Imaging System at Millimeter-wave Frequencies

by

Benjamín López García

A Dissertation
Submitted to the Program in Electronics Science,
Electronics Science Department
in partial fulfillment of the requirements for the degree of

MASTER OF SCIENCES
WITH THE SPECIALTY IN ELECTRONICS

at the

National Institute for Astrophysics, Optics and Electronics
November 2008
Tonantzintla, Puebla

Advisor:

Dr. Alonso Corona Chávez,
Electronics Department, INAOE

Dr. Ignacio E. Zaldívar Huerta,
Electronics Department, INAOE

Abstract

The need for a concealed weapons and explosive detection has increased in recent years. Millimeter-wave (MMW) imaging is a possible solution to this problem since millimeter-waves can penetrate thin clothing layers. This is a method of forming images through the detection of millimeter-wave radiation power from a scene. This power is a combination of what the scene object is directly emitting and what it is reflecting from its environment. The MMW has the ability to see under low visibility conditions (such as fog, clouds, smoke, sandstorms, etc.) that would ordinarily blind visible or infrared sensors.

Several millimeter-wave imaging systems for target identification have been reported in the current state of the art but the novelty of this thesis work is the incorporation of the Substrate Integrated Waveguide (SIW) technology in the receiver antenna and a Nipkow disc to reconstruct the image under surveillance. SIW technology has the advantages of low cost, lower losses than coplanar and microstrip lines, and it is highly integrable with microwave and millimeter wave integrated circuits. The Nipkow disc is a mechanical operating image scanning device. The device consists of a mechanically spinning disk with a series of equally distanced circular holes of equal diameter drilled in it that scan the image when rotating. This disc has the advantages of simple realization high speed scanning.

Resumen

La necesidad de detección de armas y explosivos ocultos ha aumentado en los últimos años. Los sistemas de imagenología a través ondas milimétricas es una posible solución a este problema a partir de que las ondas milimétricas pueden penetrar capas delgadas de ropa. Este es un método de formación de imágenes a través de la detección de la potencia de radiación de ondas milimétricas de una escena. Esta potencia es una combinación de lo que el objeto de la escena esta directamente emitiendo y de lo que esta reflejando de su entorno. Las ondas milimétricas tiene la capacidad de ver bajo condiciones de baja visibilidad (tales como niebla, nubes, humo, arena, etc.) que normalmente cegaría a los sensores visibles o infrarrojos.

Varios sistemas de imagenología a través ondas milimétricas para la identificación de objetos han sido reportados en el estado actual del arte, pero la novedad de este trabajo de tesis es la incorporación de la tecnología de guía de onda integrada en el mismo substrato en la antena receptora (SIW, por sus siglas en inglés) y un disco de Nipkow para reconstruir la imagen bajo observación. SIW se sintetiza por la colocación de dos filas de agujeros metálicos en un substrato. Las ventajas de la tecnología SIW son bajo costo de manufactura, menores pérdidas que las líneas coplanares y de microcinta, y su alta integrabilidad en circuitos integrados de microondas y milimétricos. El disco de Nipkow es un dispositivo mecánico de escaneo de imagen. El dispositivo consta de un disco girando mecánicamente con una serie de agujeros circulares de igual diámetro e igualmente distanciados perforados en él, que al girar escanean la imagen. Las ventajas de éste disco son su sencilla implementación y su alta velocidad de escaneo.

Acknowledgment

I would like to thank:

CONACyT for the award of the scholarship with registration number: 210,722 during the two-year of Masters.

INAOE and GTM for providing their facilities and laboratories as well as material and necessary equipment for the realization of this thesis work.

Dr. José Soto Manríquez from Institute of Physics, BUAP and Andrés Mendoza Bonilla from the Faculty of Electronics, BUAP for their help in the implementation of the nipkow disk.

Dr. Murthy for his teachings and advice, not only has he helped me tremendously in the realization of this thesis work but also in an emotional and personal level. Thanks Dr. Murthy for his valuable friendship!

My advisors and examiners for their time and dedication during the realization of this thesis work. In particular to Dr. Alonso Corona, for his wisdom, patience, and teachings, and above all for his faith in me. See you in PhD!

I would also like to thank my lovely families from Mexico and Belgium for their unconditional support and enormous sacrifice, for their teachings, values and advice they have given me. And for raising me to be the man I am now. Thank you for everything my dear family!

My friends and cousins for their great friendship, for their advice during the good and bad moments, because they have helped me to get this far. Many thanks with all my heart!

Dedicatory

To my lovely parents from Mexico and Belgium:

Humberto A. López and Silvia I. García

Michelin Van de Putte and Geer Decaluwé

To my brothers and sisters from Mexico and Belgium:

Humberto López, Hein Decaluwé, Daan Decaluwé,

Cristina López and Lien Decaluwé

To my sister and brother in law from Mexico and Belgium:

Dalia Oliva, Ángel Morales

Sigrid and Jacob

To my little nieces and nephew from Mexico and Belgium:

Lizbeth, Valeria,

Jutta and Tibe

To all my dear friends and cousins

To GOD

"Cuando el hombre se rige por amor, no hay nada ni nadie que pueda detenerlo, es libre de alcanzar sus sueños"

"Wanner de man wordt beheerst door de liefde, is er niets dat hem kan stoppen, hij vrij is om zijn dromen te bereiken"

"When the man is governed by love, there is nothing that can stop him, he is free to achieve their dreams"

Benjamín López García

Index

Chapter I

Introduction

Imaging has been performed for decades, new sensor technology in the millimeter-wave regime has enabled the generation of MMW imaging and has renewed interest in this area. This attention is, in part, driven by the ability to form images during the day or night; in clear weather or in low-visibility conditions, such as haze, fog, clouds, smoke, or sandstorms; and even through clothing.

Millimeter-wave (MMW) imaging is a method of forming images through the detection of millimeter-wave radiation from a scene. This detection can be active or passive. The election between these two approaches depends of the particular application. Nowadays different applications exist for imaging through millimeter-waves such as medical devices, security systems and surveillance cameras among others.

In this thesis work a MMW imaging system for concealed object detection is proposed. We added to the system a millimeter-wave lens to form an image of the target to the antenna and a Nipkow disc to sample the image under observation. We also incorporated the Substrate Integrated Waveguide (SIW) technology in the receiver antenna.

In Chapter II, the current state of the art of the millimeter-wave imaging and the justification of the thesis work are presented.

Chapter III deals with the radiometer theory where topics such as blackbody radiation and the Planck's radiation law are discussed. The different types of MMW imaging systems are also explained.

The details of the MMW imaging system as well as its electronics are exhibited in Chapter IV. An in depth explanation on the integrator design, the operation of the millimeter-wave lens and the absorber material are also given. At the end of this chapter, the operation of the whole system is explained.

In Chapter V the SIW antenna design is presented. This Chapter begins with an explanation of the Substrate Integrated Circuit (SIC) technology. Then it proceeds to explain the proposed wide bandwidth SIW flare antenna. Full simulations and optimization of this antenna are shown together with a comparison with the current state of the art.

Chapter VI begins by giving a theoretical introduction of the Nipkow disc device, and then it proceeds to treat the Nipkow disc system designed at optical frequencies. Finally the Nipkow disc system implementation at millimeter frequencies is discussed.

The experimental results of the remote sensing system are treated in Chapter VII. Both, active and passive experimental results obtained from the MWW imaging systems are exhibited.

Finally, all the conclusions obtained from this thesis work as well as the future work for the MMW imaging system are presented in Chapter VIII.

In Appendix A the datasheets of the materials and components used to perform the MMW imaging system are shown. The participation in conferences of this thesis work is presented in Appendix B. References used in this thesis work can be found at the end of each chapter in the References Section.

Chapter II

State of the art and justification

This Chapter is divided in two sections. The current state of the art of the millimeter-wave imaging is discussed in Section 2.1, while In Section 2.2, the justification of the thesis work is presented.

2.1 State of the art of the millimeter-wave imaging

The exploitation of the millimeter-wave regime (defined to lie between 0.3 and 300 GHz, with corresponding wavelengths between 1 m and 1 mm) for imaging has increased in recent years. The great advantage of millimeter-wave radiation is that it can be used not only in day and night conditions, but also in fog, clouds, smoke, dust and other poor visibility conditions that normally limit the “seeing” ability of both visible and infrared (IR) sensors.

The current state-of-the-art in millimeter-wave imaging systems includes two fundamentally different techniques. The first technique uses a focal-plane array (FPA) of millimeter-wave detectors placed behind a large lens. This technique can detect either passive energy emitted by the target or can use active millimeter-wave illuminators. As an example of this technique is the system proposed by Richter et. al. [2.1], where they performed a Multi-channel FPA radiometer at the frequency of 94 GHz with array modules of rectangular tapered dielectric rod antennas to scan at different viewing angles. The dielectric lens that they designed is a bifocal wide angle lens

made from high density polyethylene. This system presents a slow image acquisition time (12 min). Another example of FPA imaging system is the proposed by Watabe et. al. [2.2], who designed a 60 GHz active imaging system, which uses a Yagi–Uda antenna array. This system incorporates multilayered feed-forward neural network signal processing to recognize objects and reconstruct images distorted under coherent illumination with an image reconstruction time from 1 to 2 min. To focus the millimeter-waves scattered by the object they used two dielectric lenses to construct the images (an objective lens and a hemispherical substrate lens). These two systems present good quality in the image reconstruction but they have the disadvantages of high cost and big size due to the antenna arrays used in the receiver. A novel contribution to solve the size problem was made by Mizuno et. al. [2.3], who developed a 35 GHz passive millimeter-wave imaging apparatus with a dielectric lens and an imaging element array. Each imaging element has a single-substrate structure on which a wideband antenna, a line-transition structure, low noise amplifiers, and a detector circuit. All components have been integrated in the same substrate, reducing significantly the size of the whole system in comparison with other millimeter-wave FPA imaging systems. Another contribution was made by Luukanen et. al. [2.4] where they use an array of microbolometers as the detectors and a low cost pulsed-noise source as an illuminator. The focal plane array is fabricated on a high resistivity silicon wafer incorporating 120 microbolometers coupled to slot-ring antennas reducing significantly not only the size of the system but also its cost.

One of the main drawbacks of conventional FPAs is their small lens aperture as a consequence of limited size due to manufacturing constraints, which leads to relative low resolution and limited field of view. To overcome these, several authors have proposed image enhancement techniques. Luo et. al. [2.5], presented an improved imaging system based on the singular-value

decomposition (SVD) theorem to reconstruct the image. With this new approach a thin lens can be used as the focusing element with image quality improvements. Ocket et. al. [2.6] also performed a simplified 2D calculation method based on Huygens' principle for active millimeter wave imaging systems to avoid aberrations such as speckle and glint in the image reconstruction.

A second technique which eliminates the use of lenses is based on holographic linear arrays (phased arrays) of sequentially switched transmitter receivers scanned quickly over a large aperture to actively illuminate the target. This system operates at a single frequency, and is coherent, which means the phase of the returned signal is recorded, as well as the amplitude. The coherent data can be mathematically reconstructed in a computer to form a focused image of the target without the need for a lens. Millimeter-wave holographic imaging for concealed weapon detection was originally proposed by Farhat and Guard [2.7]. Their imaging technique utilized a stationary source and a scanned receiver system that employed optical (film-based) reconstruction. This technique was dramatically improved by Collins et. al. [2.8] by utilizing a scanned transmitter receiver and digital reconstruction. Scanning the source produces high-quality imagery because the target is illuminated over a broad range of angles, both vertically and horizontally, which greatly reduces shadowing due to specular reflection. The original techniques developed by Collins et. al. [2.8] produced high-quality imagery. However, the depth of field was very short due to the large aperture and close-range operation. This limitation has been eliminated by using the wide band holographic imaging proposed by Sheen et. al. [2.9], which consists of forming 3-D images of targets from wide-band data gathered over a 2-D aperture. There, different techniques for improving image reconstruction have been performed, as the frequency-encoding technique proposed by Derham et. al. [2.10], where a transmitter illuminates objects in the scene with a

pseudo-noise signal, and a frequency-scanning receiver antenna captures the reflected signals to be processed in an algorithm computer program. This prototype system works at the frequency of 60 GHz and the images are obtained by a combination of frequency-encoding and mechanical scanning (one motor scans the complete antenna system in azimuth and a second motor rotates the antenna to one of the fixed positions in elevation). Due to the mechanical scanning in both azimuth and elevation, the system becomes expensive but the programming time to reconstruct the image is shorter in comparison with other imaging systems (40 sec.). Dallinger et. al. [2.11] have also performed a system concept based on the circular SAR principle. They proposed a circular synthetic aperture to scan a person's body entirely and an algorithm to enhance the image quality based in the method of stationary phase to obtain the image's Fourier transform. By using this circular aperture only the necessary amount of hardware components is at minimum, because only a single monostatic sensor needs to be designed. With this system concealed weapon detection can be successfully performed with a good quality in the image reconstruction. On the other hand, Zhang et. al. [2.12] designed multispectral image fusion techniques which can significantly improve the spatial content of mm-wave images. Three different pixel-level fusion methods, including band ratioing fusion, wavelet transform fusion, and principle component fusion, have been applied to mm-wave images of two test objects, captured in W-band. The experimental results show that band ratioing fusion performs the best in revealing detailed features of the object, wavelet transform fusion performs well in distinguishing the object from the background, and principle component fusion has the potential to reduce speckle resulting in better image quality. Therefore, these fusion methods are believed to be helpful for object recognition tasks in active millimeter wave imaging applications. Another interest approach of phased array systems is the W-band phased array imager performed by Lovberg et. al. [2.13]. It consists of a broadband phased array receiver from 76 to 94 GHz, and a

single planar slot-array antenna. The object radiation is detected by the antenna, followed by phase sorting into azimuth bins and then frequency sorting into elevation bins, to create a two-dimensional image. This system has the advantage of a reduced volume requirement in compare with FPA imaging systems, since no dedicated focal area is required. The disadvantage of this design is that the fidelity, sharpness and contrast of imagery are affected by the quality of the array phasing.

These two techniques (FPA and holographic) explained above have a lot of potential applications in security scanning [2.14], in plasma diagnostics [2.15], atmospheric and planetary remote sensing [2.16], automotive collision-avoidance radar [2.17], safe aircraft landing [2.18], and as diagnostic tools in areas such as agriculture, forestry, and food industry [2.3]. More recent applications of terahertz spectroscopy for character recognition in medieval manuscripts [2.19] and art conservation [2.20] have been reported.

In the field of security, scanning the detection of concealed weapons underneath a person's clothing is an important obstacle to the improvement of the security of the general public as well as the safety of public assets like airports and buildings. Due to this, several researchers have devoted much effort to the development of a variety of techniques for concealed weapon detection. As an example McMakin *et al.* [2.14], developed a novel wideband millimeter-wave imaging system which allows rapid inspection of personnel for concealed explosives, handguns, or other threats. To form an image rapidly, a linear array of 128 antennas is used to electronically scan over a horizontal aperture, while the linear array is mechanically swept over a vertical aperture. At each point over this 2-D aperture, coherent wideband data reflected from the target is gathered using wide beamwidth antennas. The data is recorded coherently, and reconstructed using an efficient image reconstruction algorithm. This algorithm works in the near-field of both the

target and the scanned aperture and preserves the diffraction limited resolution of less than one wavelength. The wide frequency bandwidth is used to provide depth resolution, which allows the image to be fully focused over a wide range of depths, resulting in a full 3-D image. This system has been extensively tested using concealed metal and plastic weapons, and has recently been tested using real plastic explosives (C-4 and RDX) and simulated concealed liquid explosives

In plasma diagnostics, significant advances in millimeter wave and THz receiver and array technology have led to new approaches for the visualization of density and temperature fluctuations inside the core of high temperature plasmas, as the work made by Domier et. al. [2.15]. Their system collects millimeter wave electron cyclotron emission from the plasma and images it onto a planar mixer array to form 2-D images of electron temperature fluctuations. Collective scattering approaches at THz frequencies can resolve density fluctuations deep into the plasma core that are not accessible via reflectometry.

For atmospheric and planetary remote sensing millimeter-wave radiometers have found extensive use in several geoscientific fields including meteorology, oceanography, and hydrology, as will discussed in Chapter 3. Most of these applications are those involving observations of oceanographic parameters or atmospheric parameters over the ocean, such as sea surface temperature, wind speed, atmospheric water-vapor content, liquid-water content, temperature profiles, rainfall rates, etc.

Recently, IR diagnostics are now widely used to check maturity of fruit such as apple, peach, etc. This diagnostics utilizes a spectroscopic way to determine degree of sweetness. However, this method can not apply for fruit with thick skin such as citron, watermelon, etc. Because of this, Mizuno et. al.

[2.3], have been designed an imaging system (described in the previous paragraphs) to measure fruit using millimeter-wave technology to check maturity by passive millimeter-wave diagnostic. The results obtained with this system suggest we can recognize whether fruit would be mature or not using millimeter-wave passive imaging. Mizuno et. al. [2.3] performed another imaging apparatus which uses the Fresnel distance principle. The imaging element is mechanically scanned in front of an object of a distance within 10 wavelengths (Fresnel distance). This system can be used for nondestructive inspection of timber, for example, damage suffered from white ants, search on existence of knots, and so on, or for measuring the temperature of an object inside a cardboard box.

2.2 Justification

As discussed in the above Section, most of the current millimeter-wave imaging systems present the disadvantages of high cost, slow image acquisition time, complex computer algorithms to reconstruct or enhance the image quality, and difficult implementation due to the focal plane and phase arrays used as receivers. Because of this, a new millimeter-wave imaging system has been proposed for this thesis work where the cost and image reconstruction are improved significantly by introducing the relative new substrate integrated waveguide (SIW) technology in the receiver antenna, and a Nipkow disc to reconstruct the image under observation. As will be explained in Chapter 5, SIW technology is synthesized by placing two rows of metallic via-holes in a substrate where the field distribution is similar to that of a conventional rectangular waveguide with the advantage of being low cost. Moreover, SIW presents lower losses when compared to other planar technologies such as coplanar or microstrip. The Nipkow disc is a mechanical

operating image scanning device which consists of a mechanically spinning disk with a series of circular holes drilled in it. These holes are positioned to form a single-turn spiral so that each hole takes a horizontal "row" through the image which is sampled as a pattern of *light* or *dark* by a sensor. This information can then be easily displayed on a computer screen, as will be shown in Chapter 6.

References

[2.1] J. Richter, D. Notel, F. Kloppel, J. Huck, H. Essen, and L.-P. Schmidt, "A Multi-Channel Radiometer with Focal Plane Array Antenna for W-Band Passive Millimeterwave Imaging," *IEEE MTT-S International Microwave Symposium Digest, 2006*, pp. 1592-159, June 2006.

[2.2] K. Watabe, K. Shimizu, M. Yoneyama, and K. Mizuno, "Millimeter-Wave Active Imaging Using Neural Networks for Signal Processing," *IEEE Transactions on Microwave Theory and Techniques*, vol. 51, no. 5, pp. 1512-1516, May 2003.

[2.3] K. Mizuno, H. Matono, Y. Wagatsuma, H. Warashina, H. Sato, S. Miyanaga, and Y. Yamanaka, “New Applications of Millimeter-Wave Incoherent Imaging,” *IEEE MTT-S International Microwave Symposium Digest, 2005,* pp. 629-632, June 2005.

[2.4] A. Luukanen, A. J. Miller, and E. N. Grossman, "Active millimeter-wave video rate imaging with a staring 120-element microbolometer array," from http://www.emergencymgt.net/sitebuildercontent/sitebuilderfiles/ActiveMillimeterWave.pdf

[2.5] Z. Luo, J. Xiong, and J. Yang, "An Image Regulation Technique for Passive Millimeter Wave Focal Plane Array Imaging Radar System," *International Conference on Radar, 2006*, pp. 1-4, Oct. 2006.

[2.6] I. Ocket, B. Nauwelaers, G. Koers, and J. Stiens, “Fast Modeling and Optimization of Active Millimeter Wave Imaging Systems,” *36th European Microwave Conference, 2006*, pp. 1559-1562, Sept. 2006.

[2.7] N. H. Farhat and W. R. Guard, “Millimeter wave holographic imaging of concealed weapons,” *Proceedings of the IEEE*, vol. 59, pp. 1383-1384, Sept. 1971.

[2.8] H. D. Collins, D. L. McMakin, T. E. Hall, and R. P. Gribble, “Real-time holographic surveillance system,” U.S. Patent 5 455 590, Oct. 3, 1995.

[2.9] D. M. Sheen, H. D. Collins, T. E. Hall, D. L. McMakin, R. P. Gribble, R. H. Severtsen, J. M. Prince, and L. D. Reid, “Real-time wideband holographic surveillance system,” U.S. Patent 5 557 283, Sept. 17, 1996.

[2.10] T. Derham, H. Kamoda, T. Iwasaki, and T. Kuki, "Active MMW Imaging System using the Frequency-Encoding Technique," *Microwave Conference, 2007. KJMW 2007. Korea-Japan*, pp. 181-184, Nov. 2007.

[2.11] A. Dallinger, S. Schelkshorn, and J. Detlefsen, “Efficient omega-k-Algorithm for Circular SAR and Cylindrical Reconstruction Areas,” in *Kleinheubacher Tagung, ser. Advances in Radio Science*, Germany 2005.

[2.12] L. Zhang, J. Stiens, and H. Sahli, "Multispectral Image Fusion for Active Millimeter Wave Imaging Application," *Global Symposium on Millimeter Waves, 2008. GSMM 2008*, pp. 131-134, April 2008.

[2.13] J. A. Lovberg, C. Martin, and V. Kolinko, "Video-Rate Passive Millimeter-Wave Imaging Using Phased Arrays," *IEEE/MTT-S International Microwave Symposium, 2007*, pp. 1689-1692, June 2007.

[2.14] D. L. McMakin, D. M. Sheen, and H. D. Collins, "Remote concealed weapons and explosive detection on people using millimeter-wave holography," *Security Technology, 1996. 30th Annual 1996 International Carnahan Conference*, pp. 19-25, Oct. 1996.

[2.15] C. W. Domier, N. C. Luhmann, H. K. Park, Z. Xia, and P. Zhang, "Advances in millimeter wave/THZ plasma diagnostics instrumentation", *Infrared and Millimeter Waves, 2007 and the 2007 15th International Conference on Terahertz Electronics. Joint 32nd International Conference on IRMMW-THz*, pp. 8-11, Sept. 2007.

[2.16] F.T. Ulaby, R. K. Moore, and A. K. Fung, “Microwave Remote Sensing: Active and Passive, Volume I, Microwave Remote Sensing Fundamentals and Radiometry,” Artech House, 1981.

[2.17] M. Behet, “Low Cost MMICS for Automotive Radar and Passive Radiometric Imaging Applications,” *MM-Wave Products and Technologies, 2006. Seminar on the Institution of Engineering and Technology*, pp. 58-62, Nov. 2006.

[2.18] M. Shoucri, R. Davidheiser, B. Hauss, P. Lee, M. Mussetto, S. Young, and L. Yujiri, "A passive millimeter wave camera for aircraft landing in low visibility conditions,"

IEEE Aerospace and Electronic Systems Magazine, vol. 10, no. 5, pp. 37-42, May 1995.

[2.19] K. Fukunaga, Y. Ogawa, S. Hayashi, and I. Hosako, “Application of terahertz spectroscopy for character recognition in a medieval manuscript ,” IEICE Electronics Express, vol. 5, no. 7, pp. 223-228, April, 2008.

[2.20] K. Fukunaga, Y. Ogawa, S. Hayashi, and I. Hosako, “Terahertz Spectroscopy for art conservation,” *IEICE Electron. Express*, vol. 4, pp. 258-263, 2007.

Chapter III

Radiometer and Millimeter-Wave Imaging Theory

In this chapter some elements of the radiometer theory will be explained and after that millimeter-wave imaging systems will be treated. Among the important discussed topics we find blackbody radiation and the Planck's radiation law.

3.1 Radiometer Theory

3.1.1 Introduction

All matter radiates electromagnetic energy. The radiation is a consequence of the interaction between the atoms and molecules in the material. A material also may absorb and/or reflect energy incident upon it. When in thermodynamic equilibrium with its environment, a material absorbs and radiates energy at the same rate [3.1]. A *blackbody* is defined as an ideal material that absorbs all the incident radiation, reflecting none, as will be explained in depth in Section 3.1.2. Since the absorbed energy by a material would increase its temperature if no energy were emitted, a perfect absorber also is a perfect emitter. The blackbody radiation spectrum is given by Planck's radiation law (see Section 3.1.2), which was formulated by Max Planck in 1901 by introducing the concept of the quantum of energy. This

spectrum is used as a reference against which the radiation spectra of real bodies at the same physical temperature are compared. The spectral, polarization, and angular variations of the radiation emitted, absorbed, and scattered by a medium are governed by the geometrical configuration of the surface and interior of the medium, and by the spatial distributions of its dielectric properties and its temperature.

Radiometry is the measurement of electromagnetic radiation [3.2], [3.3]. A millimeter-wave radiometer is a highly sensitive receiver capable of measuring low levels of millimeter-wave radiation. When a scene, such as terrain, is observed by a millimeter-wave radiometer (through its antenna beam), the radiation received by the antenna is partly due to self-emission by the scene and partly due to reflected radiation originating from the surroundings. Through proper choice of the radiometer parameters (wavelength, polarization, and viewing angle), it is sometimes possible to establish useful relations between the magnitude of the energy received by the radiometer and specific parameters of interest.

3.1.2 Planck's Blackbody Radiation Law

The concept of a blackbody is of fundamental importance to an understanding of the thermal emission of real materials because its emission spectrum represents a reference, relative to which the radiant emittance of a material can be expressed. In general, of the radiation incident upon the surface of a solid (or liquid) substance, a certain fraction is absorbed and the remainder is reflected. *A **blackbody** is defined as an idealized, perfectly opaque material that absorbs all the incident radiation at all frequencies, reflecting none* [3.1]-[3.3]. In addition to being a perfect absorber, *a blackbody is also a perfect*

emitter, since energy absorbed by a material would increase its temperature if no energy were emitted.

In practice, a good approximation to a blackbody is a hollow body with a small opening. Any radiation entering the container through the opening is absorbed or undergoes many reflections on the inside surfaces, so that all the original energy is effectively absorbed before it can be reflected back out through the opening. If the container is maintained at some fixed temperature T, its inner surfaces will emit and absorb photons at the same rate, and therefore the energy leaking out through the opening resembles radiation by a blackbody in thermodynamic equilibrium. At millimeter-wave frequencies, good approximations to ideal blackbodies are the highly absorbing materials used in the construction of anechoic chambers.

According to Planck's radiation law, a blackbody radiates uniformly in all directions with a spectral brightness B_f given by

$$B_f = \frac{2hf^3}{c^2}\left(\frac{1}{e^{\frac{hf}{kT}} - 1}\right) \qquad (3.1)$$

where B_f = Blackbody spectral brightness, W m^{-2} sr^{-1} Hz^{-1}

h = Planck's constant = 6.63×10^{-34} joules

f = frequency, Hz

k = Boltzmann's constant = 1.38×10^{-23} joule K^{-1}

T = absolute temperature, K

c = velocity of light = 3×10^8 ms^{-1}.

The only two variables in (3.1) are f and T. A family of curves of B_f as a function of frequency are shown in Figure 3.1 (with T as parameter). Logarithmic scales are used on both axes so that a wide range of values can

be accommodated. These curves exhibit two interesting features: (1) as the temperature *T* is increased, the overall level of the spectral brightness curve increases, and (2) the frequency at which B_f, is maximum increases with *T*.

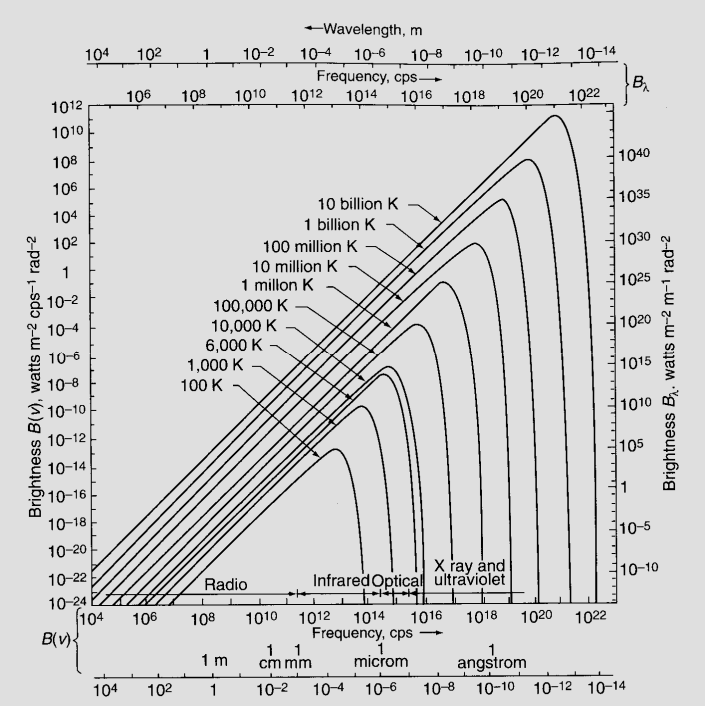

Figure 3.1. Planck radiation-law curves (from [3.3]).

Over a narrow frequency interval *df* centered at *f,* the brightness is given by

$$dB = B_f \, df \tag{3.2}$$

It is sometimes of interest to express the spectral brightness in terms of B_λ, rather than B_f where B_λ is the power per unit area per unit solid angle per unit wavelength. Over a wavelength interval $d\lambda$ corresponding to the frequency interval *df* above, the area under the curve contains the same brightness *dB*. Thus,

$$dB = B_\lambda \, d\lambda \tag{3.3}$$

From equations (3.2) and (3.3) and noting that

$$df = -\frac{c}{\lambda^2} d\lambda \tag{3.4}$$

the following expression for B_λ is obtained:

$$B_\lambda = \frac{2hc^3}{\lambda^5}\left(\frac{1}{e^{\frac{hc}{\lambda kT}} - 1}\right) \tag{3.5}$$

The negative sign in (3.4) has been ignored because it merely reflects the fact that *f* and *λ* increase in opposite directions and it has no bearing on the magnitudes of *dλ* and *df.* The curves shown in Figure 3.1 are also plots of B_λ, with the right-hand ordinate scale expressing B_λ, and the corresponding frequency and wavelength scale given as abscissa along the top of the chart.

3.1.3 Application of millimeter-wave radiometry

Millimeter-wave radiometry has a lot of applications as discussed in Chapter 2. All these applications can be classified into three general topics: astronomical studies, military and security applications, end environmental monitoring. A fourth relative new topic can be included: food applications. Radiometers have been used to measure the radio emission from numerous objects in our galaxy as well as from objects in other galaxies [3.4].

The military and security use of radiometers is primarily for detecting or locating hidden weapons [3.5]-[3.9]. The term used for characterizing the emission by the scene observed by the radiometer (through its antenna

beam) is the brightness temperature T_B, which may vary from zero K (for a non emitting medium) to a maximum value equal to the physical temperature T_o, of the scene (for a perfect emitter known as a blackbody). Equivalently, the emissivity $e(=T_B/T_o)$ varies between zero and unity. Theoretically, a perfectly conducting material, such as a metal object, has zero emissivity, thereby making it easy to differentiate from the earth's background (the emissivity for land surfaces is rarely <0.3 and is often >0.7). Although metal objects do not self-emit, their radiometric temperatures are not identically zero because they reflect downward-emitted sky radiation. The radiometric contrast between a *field of view* (FOV) with and without a target contained in it is a function by the antenna beamwidth, being in turn determined by the size of the antenna and the millimeter-wave frequency. Operationally, millimeter-wave radiometers are used in conjunction with other superior-spatial-resolution sensors such as radars and infrared scanners, which serve as the prime sensors for detecting the presence of military targets.

Aside from their use in radio astronomy and for military applications, millimeter-wave radiometers have found extensive use in several geoscientific fields including meteorology, oceanography, and hydrology [3.3]. Most of these applications are those involving observations of oceanographic parameters or atmospheric parameters over the ocean, such as sea surface temperature, wind speed, atmospheric water-vapor content, liquid-water content, temperature profiles, rainfall rates, etc. Over land, monitoring snow accumulation and depletion may be feasible. Another land application that may be served by millimeter-wave radiometry is soil-moisture determination [3.10]. Extensive research has been conducted using ground-based and airborne millimeter-wave radiometers to determine the radiometric sensitivity to soil moisture content, soil surface roughness, soil type, and (to a lesser extent) vegetation cover.

3.1.4 Operation of radiometers

The signal received by a radar receiving antenna consists of energy scattered back by the target after it has been illuminated by the radar transmitting antenna. For the radiometer, the "transmission source" is the target itself, and the radiometer is merely a passive receiver. The energy received by a radiometer is due to radiation self-emitted and/or reflected by the scene and collected by the antenna. The power *P* emitted by an object in thermodynamic equilibrium is a function of its physical temperature *T*, and in the millimeter-wave region *P* is directly proportional to *T*, [3.3]. For a given value of *T*, the maximum amount of power that an object can emit is equal to P_{bb}, the power emitted by an ideal blackbody. If a millimeter-wave antenna is placed inside a chamber whose walls are made of a perfectly absorbing (and therefore, perfectly emitting) material, the power received by the antenna is

$$P_{bb} = kTB \tag{3.6}$$

where *k* is Boltzmann's constant and *B* is the radiometer bandwidth. The above correspondence between power and temperature has led to the definition of *radiometric* temperatures to characterize the power emitted by or received from a real scene. Specifically, the term radiometric *brightness temperature* T_B is used to characterize the emission by a material through the expression

$$T_B = \frac{P}{kB} \tag{3.7}$$

where *P* is the power emitted by the material over the bandwidth *B.*

Similarly, corresponding to the power P_A received by a radiometer antenna, a radiometric *antenna* temperature T_A is defined by

$$T_A = \frac{P_A}{kB} \tag{3.8}$$

If the scene observed by the antenna beam is characterized by a uniform brightness temperature T_B (representing radiation in the direction of the antenna), then T_A=T_B. In the general case, however, T_A represents all incident radiation upon the antenna, integrated over all possible directions and weighted according to the antenna directional pattern. Additionally, in the real situation, other factors also are involved. These include the effects of the atmosphere and self-emission by the antenna structure.

It was stated earlier that a radiometer is merely a passive receiver. A radiometer, however, is different from traditional radar or communications receivers in two respects. First, whereas the input signal that is processed by a traditional receiver may be phase-coherent and nearly monochromatic, the natural radiation emitted by material media is phase-incoherent and extends over the entire electromagnetic spectrum. That is, it is "noiselike'" in character and similar to the noise power generated by the receiver components.

The second difference relates to the signal-to-noise ratio, S_n, at the receiver output. In traditional receivers, faithful extraction of the information contained in the received signal necessitates that S_n >>1 to differentiate the signal from the fluctuating component of the noise. This condition usually is achieved through a combination of amplitude and waveform design of the transmitted signal and the application of signal-processing modes in the receiver section, although some scatterometers use methods similar to those used in radiometers.

Unlike the situation in traditional receivers, the radiometric signal to be measured, P_A, usually is much smaller than the receiver noise power. Radiometers are highly sensitive receivers that are configured to measure very small input signal levels with a high degree of precision. Several different configurations have been developed, [3.11]. For the purposes of this thesis work, we shall discuss the operation of the configuration used for the MWW imaging system (Section 4.1), known as the *total-power radiometer*.

The block diagram of a typical total power radiometer is show in Figure 3.2. The front end of the receiver is a standard superheterodyne circuit consisting of a radio frequency (RF) amplifier, a mixer/local oscillator, and an intermediated frequency (IF) stage, followed by a detector and an integrator. The power delivered by the antenna usually is broadband noise extending over a wider bandwidth than the receiver bandwidth B. The function of the RF amplifier is to filter the input signal by amplifying the frequency components contained in the bandwidth B centered at the RF frequency of interest, f_{RF}. The mixer and IF amplifier translate the RF band of signals of bandwidth B to the same bandwidth at the IF and provide further amplification. In practice, the RF amplifier usually has a wider bandwidth than that of the IF amplifier, and therefore the predetection bandwidth B is effectively determined by the IF amplifier bandpass characteristics. The detector is generally a square-law device, so that its output voltage is proportional to the input power, [3.12]. The integrator is essentially a low-pass filter with a cutoff frequency of $1/\tau$, and serves to smooth out short-term variations in the noise power.

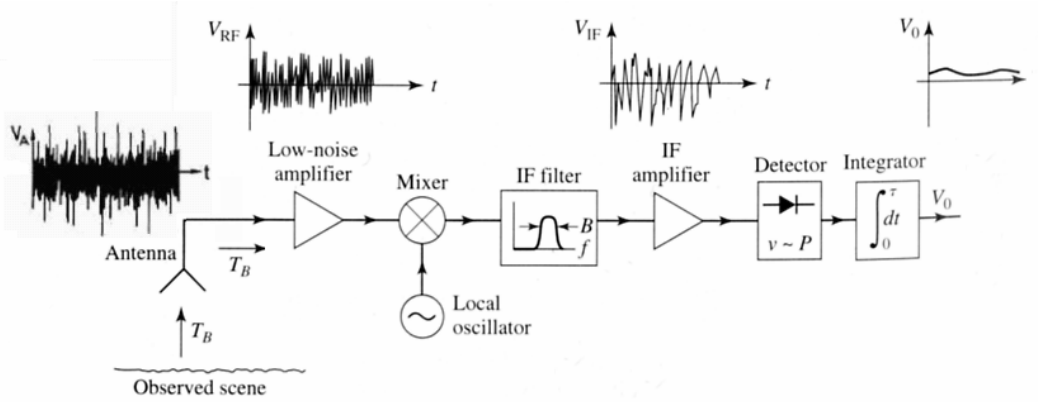

Figure 3.2. Total power radiometer block diagram.

If the antenna is pointed at a background scene with a brightness temperature T_B, the antenna power will be $P_A=kT_BB$. The receiver contributes noise which can be characterized as a power $P_R=kT_RB$ at the receiver input, where T_R is the overall noise temperature of the receiver. Thus the output voltage of the radiometer is

$$Vo = G(T_B + T_R)kB \tag{3.9}$$

where G is the overall gain constant of the radiometer. Conceptually, the system is calibrated by replacing the antenna input with two calibrated noise sources, from which the system constants GkB and GT_RkB can be determined. (This is similar to the Y-factor method for measuring noise temperature). Then the desired brightness temperature, T_B, can be measured with the system.

Two types of errors occur with this radiometer. First is an error, ΔT_N, in the measured brightness temperature due to noise fluctuations. Since noise is a random process, the measured noise power may vary from one integration

period to the next. The integrator acts to smooth out ripples in V_0 with frequencies components greater than $1/\tau$. Then the remaining error is

$$\Delta T_N = \frac{T_B + T_R}{\sqrt{B\tau}} \tag{3.10}$$

This result shows that if a longer measurement time, τ, can be tolerated, the error due to noise fluctuation can be reduced to a negligible value.

A more serious error is due to random variations in the system gain, G. Such variations generally occur in the RF amplifier, mixer, LO or IF amplifier, over a period of one second or longer. So if the system is calibrated with a certain value of G, which changes by the time a measurement is made, an error will occur, as given as

$$\Delta T_G = \left(T_B + T_R\right)\frac{\Delta G}{G} \tag{3.11}$$

where ΔG is the rms change in the system gain, G.

It will be useful to consider some typical numbers at this time. For example, a 10 GHz total power radiometer may have a bandwidth of 100 MHz, a receiver temperature of T_R=500 K, an integrator time constant of τ=0.01 s, and a system gain variation $\Delta G/G$=0.01. If the antenna temperature is T_B=300 K, (3.10) gives the error due to noise fluctuations as, ΔT_N =0.8 K, while (3.11) gives the error due to gain variations as ΔT_G=8K. These results, which are based on reasonably realistic data, show that gain variation is the most detrimental factor affecting the accuracy of the total power radiometer.

3.2 Millimeter-wave imaging

3.2.1 What is Millimeter-wave Imaging?

Millimeter-wave imaging is a method of forming images through the detection of millimeter-wave radiation from a scene [3.1]. This power is a combination of what the scene object is directly emitting and what it is reflecting from its environment. The amount of power can be assigned a level within a gray scale to generate the image. The amount is thus fundamental to the generation of the image, and an understanding of what contributes to this power is needed.

The millimeter-wave radiation has the ability to see under conditions of low visibility (fog, clouds, smoke, sandstorms, etc.) that would ordinarily blind visible or infrared (IR) systems. The amount of radiation emitted in the millimeter wave range is 10^8 times smaller than the amount emitted in the infrared range. Millimeter-wave imaging also provide transmission through optically opaque layers and passes through many materials such as clothing.

3.2.2 Types of millimeter-wave imaging

In general, there are two different modes which can be distinguished for the development of millimeter-wave imaging systems: the passive mode and the active mode,

3.2.2.1 Passive millimeter-wave imaging

Passive millimeter-wave mode may be defined as picture-taking with millimeter-waves, where each target is an energy source that generates and radiates or reflects energy in the millimeter-wave region as shown in Figure 3.3. In this mode the spectral distribution of natural radiation which is emitted or reflected from the target at environmental temperatures is properly captured and displayed (radiometry concept), the targets are not "illuminated" by reflected or scattered sources. Because the sources themselves are active, the system -without its own illuminator- is termed *passive*. On this mode the radiation of MMW is non ionizing and hence radiation does not represent a health hazard to people under observation.

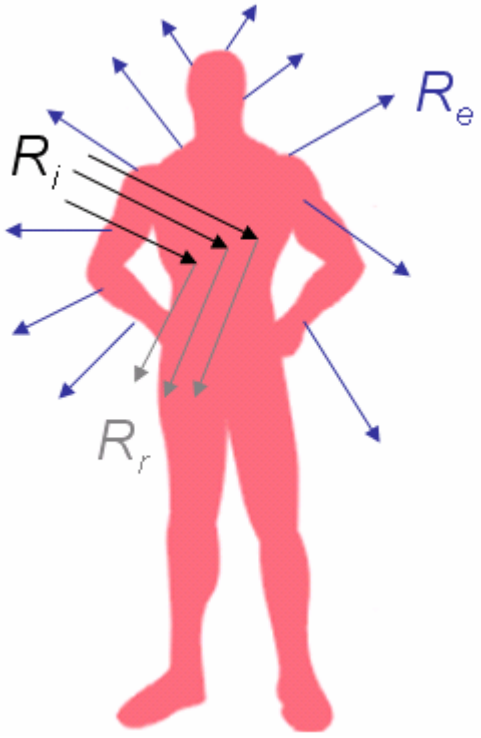

Figure 3.3. Passive millimeter-wave mode. R_i = incident radiation, R_r = reflected radiation, and R_e = emitted radiation.

3.2.2.1 Active millimeter-wave imaging

In *Active millimeter-wave mode* a millimeter-wave source is required to illuminate the scene. The source produces much higher powers than those thermally emitted from targets within the scene as illustrated in Figure 3.4. In active imaging, thermal millimeter waves generated by objects within the scene are of less significance due to the much higher power produced by the source which allows us to have a better contrast than in passive mode. On this mode we have to verify that the millimeter-wave radiation does not present a health hazard to people by complying with the safety standards for RF/microwave exposures, as will be explained in Section 4.5.2.

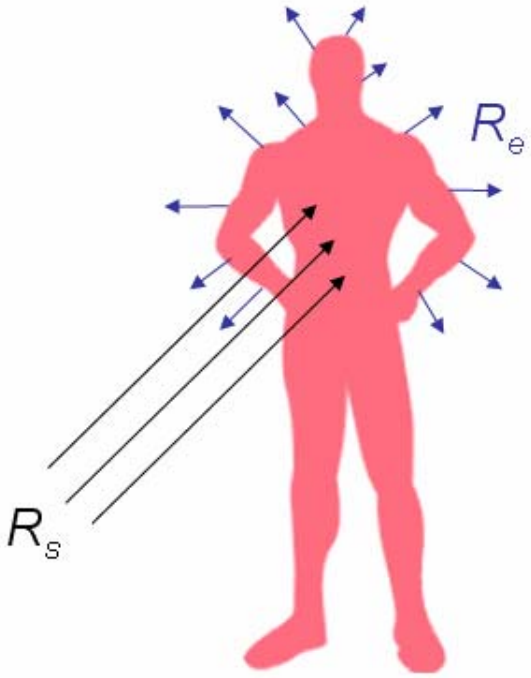

Figure 3.4. Active millimeter-wave mode. R_s = radiation emitted by the source to illuminate the target, and R_e = emitted radiation. *Re* << *Rs*.

In this thesis work, both passive and active modes have been performed as will be shown in the next Chapter.

References

[3.1] L. Yujiri, “Passive Millimeter Wave Imaging,” *Microwave Symposium Digest, 2006. IEEE MTT-S International*, pp. 98-101, June 2006.

[3.2] D. M. Pozar, “Microwave Engineering,” 3rd ed., Ed. Wiley, 2005.

[3.3] F.T. Ulaby, R. K. Moore, and A. K. Fung, “Microwave Remote Sensing: Active and Passive, Volume I, Microwave Remote Sensing Fundamentals and Radiometry,” Artech House, 1981.

[3.4] R. D. Wolstencroft, and W. B. Burton, “Millimetre and Submillimetre Astronomy,” 1st ed., Ed. Kluwer Academic Publishers, 1988.

[3.5] L. Yujiri, M. Shoucri, and P. Moffa, “Passive millimeter wave imaging,” *IEEE Microwave Magazine*, vol. 4, no. 3, pp. 39-50, Sep. 2003.

[3.6] G.N. Sinclair, R.N. Anderton, and R. Appleby, “Outdoor passive millimetre wave security screening,” *Security Technology, 2001 IEEE 35th International Carnahan Conference*, 16-19 Oct. 2001, pp. 172-179.

[3.7] D.O. Korneev, L. Y. Bogdanov, and A.V. Nalivkin, **“**Passive Millimeter Wave Imaging System with White Noise Illumination for Concealed Weapons Detection,**”** *Infrared and Millimeter Waves, 2004 and 12th International Conference on Terahertz Electronics, 2004. Conference Digest of the 2004 Joint 29th International Conference*, 27 Sept.-1 Oct. 2004, pp. 741-742.

[3.8] D.L. McMakin, D.M. Sheen, and T.E. Hall, “Three-Dimensional Millimeter-wave Imaging for Concealed Weapon Detection,” *Microwave Theory and Techniques, IEEE Transactions*, vol. 49, no. 9, pp. 1581-1592, Sep. 2001.

[3.9] D.L. McMakin, D.M. Sheen, and H.D. Collins, “Remote Concealed Weapons and Explosive Detection on People Using Millimeter-wave Holography,” *Security Technology, 1996. 30th Annual 1996 International Carnahan Conference*, 2-4 Oct. 1996, pp. 19-25.

[3.10] A. Monerris, M. Cardona, M. Vall-llossera, A. Camps, R. Sabia, R. Villarino, E. Álvarez, and S. Sosa, "Soil Moisture Retrieval Errors Using L-band Radiometry Induced by the Soil Type Variability," from: http://www.tsc.upc.edu/prs/pdfs/monerris_soilmoisturer_200 5.pdf

[3.11] M. E. Tiuri “Radio Astronomy Receivers,” *Antennas and Propagation, IEEE Transactions*, vol. 12, no. 7, pp. 930-938, Dec 1964.

[3.12] G. Leinweber, “Square Law Diode Detectors in 50 ohm Systems,” from: http://engphys.mcmaster.ca/~elmer101/sqlaw/sqlaw.html

Chapter IV

Experimental Arrangement

This chapter explains the details of the millimeter-wave (MMW) imaging system as well as the assembled radiometer (Section 4.1). In Section 4.2 an in depth explanation on the integrator design is given. In the Sections 4.3 and 4.4 the operation of the millimeter-wave lens and the absorber material are exhibited, respectively. Finally, in Section 4.5, the operation of the whole system in both active and passive approach will be explained.

4.1 Block diagram of the MMW imaging system

The block diagram of the proposed MMW imaging system is shown in Figure 4.1. The goal of the system consists of a millimeter-wave absorbing background foam, a millimeter-wave lens, a receiving antenna, and a radiometer. The foam is used only in active approach as mentioned in Section 4.4. The different objects are sensed by placing them in front of the antenna and focused by the millimeter-wave lens. This lens is made of *teflon* and has a diameter of 16.2 cm. Its focal length was obtained in both theoretically and experimentally as discussed in Section 4.3. For the receiving antenna, three different types of antennas were used in the development of the system as explained in Section 4.5. As a novelty in MMW imaging a fourth substrate integrated waveguide antenna was designed to be used in the MMW imaging system, which will be explained in detail in next Chapter.

As we see in Figure 4.1, we added to the system a nipkow disc to sampled the image formed by the lens and finally displayed it on the computer. It consists of a metal disc which has a spiral of circular holes drilled in it. Each hole provides one of the curved scan lines to reconstruct the image being observed as explained in detail in Chapter 6.

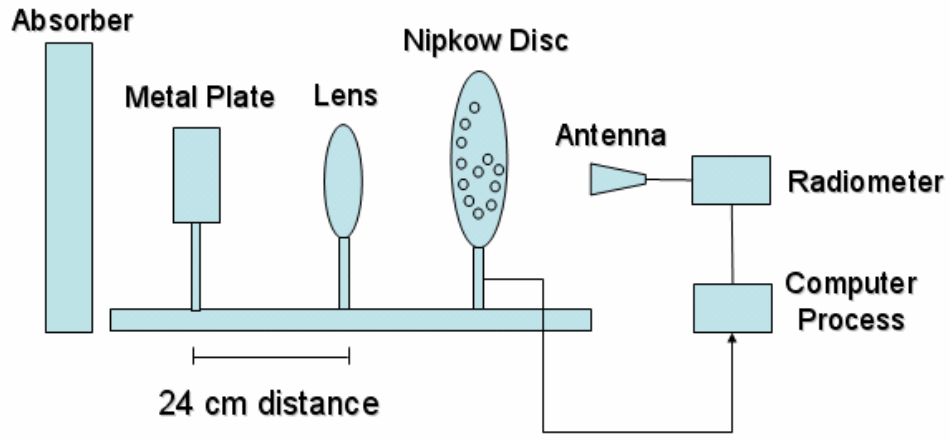

Figure 4.1. Block diagram of the MMW imaging system.

The radiometer constructed for the MWW imaging system is shown in Figure 4.2. The total power configuration was utilized (see Section 3.1.4). All the components were placed into a metal box to avoid electromagnetic interference from the surroundings.

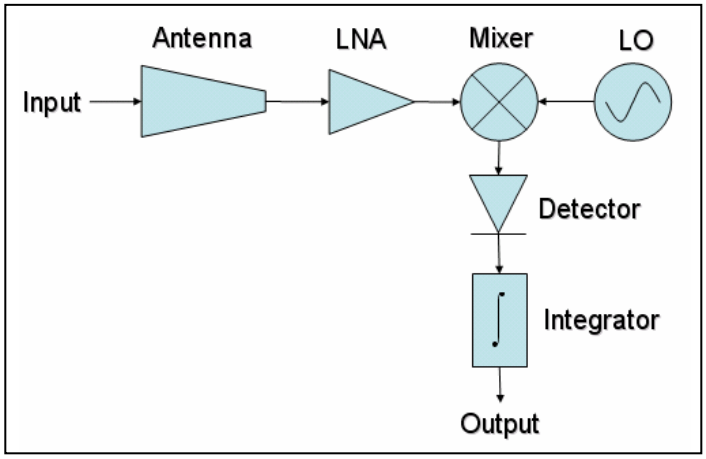

Figure 4.2. Electronics of the MMW imaging system.

The specifications of the components used in the constructed radiometer are shown in Table 4.1. The LNA is used to amplify the small radiation emitted by the target. It has a bandwidth from 15 to 26 GHz, 2.8 dB (1.90 W) of noise figure (NF) and a gain (G) of 55 dB (316.23 W).

The mixer is a triple balanced mixer with Noise Figure of NF=9.5 dB (8.91 W). It works in down-conversion mode.

The local oscillator achieves an output power (OP) from 13 to 16 dBm (19.95 to 38.91 mW) with phase noise (PN) of ~135 dBc/Hz, and a tuning range from 20.641 to 21.7 GHz.

The detector is a square law detector, with a bandwidth from 0.01 to 40 GHz and a standing wave ratio (SWR) of 1.90 at 40 GHz. To interconnect all the components we used microwave flexible cables (model 85CF-0030-20X20, from *Microstock, Inc.*) of 5.5 cm length each with *K type connectors* on both sides. The bandwidth of the whole system is determined, in our case, by the LNA and the rectangular horn antenna, thus providing a system bandwidth from 18 to 26 GHz.

Table 4.1. Component characteristics of the total power radiometer.

Component	Company	Characteristics	Frequency (GHz)	Model Number
LNA	QuinStar Technology, Inc.	55 dB, G 2.8 dB, NF	15 – 26	QLW-15262855-JO
Mixer	M/A-Com Inc.	9.5 dB, NF	LO: 2 – 24 RF: 2– 24 IF: 0.1 – 5	MY52C
LO	Lucix Corporation	13-16 dB, OP 135 dBc/Hz, PN	20.641 – 21.7	LO-211-FC-207378
Detector	Anritsu Corporation	1.90, SWR	0.01 – 40	75VA50

4.2 Integrator design

The purpose of the integrator is to enhance the sensitivity of the system as we have seen in Section 3.1.4. We designed an integrator using an operational amplifier (TL081CP from *Texas Instruments*) on a protoboard. The electronic integrator [4.1], is a device that produces an output waveform whose value at any instant of time equals the total area under the input waveform up to that point of time (mathematical integration). When the input to a practical integrator is a dc level, the output will rise linearly with time, and will eventually reach the maximum possible output voltage of the amplifier (saturation). To eliminate this problem in practical integrators, a resistor R_f is connected in parallel with the feedback capacitor C, as shown in Figure 4.3. Since the capacitor is an open circuit as far as dc is concerned, the integrator responds to dc inputs just as if it were a normal inverting amplifier. At high frequencies, the impedance of the capacitor is much smaller than R_f, so the parallel combination of C and R_f is essentially the same as C alone, and signals are integrated as usual.

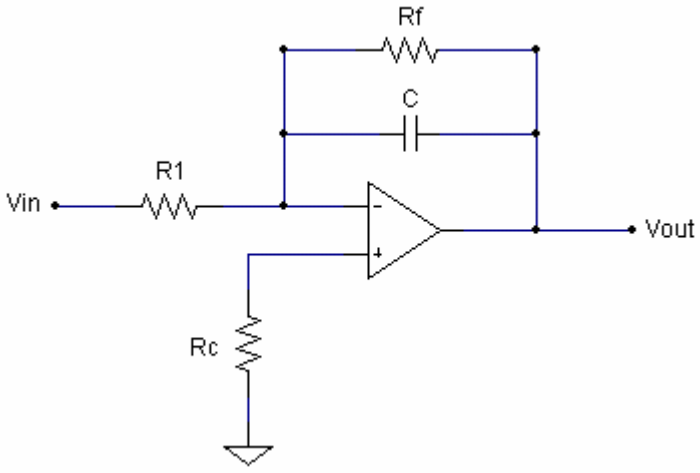

Figure 4.3. Diagram circuit of a practical integrator.

Because the integrator's output amplitude decreases with frequency, it is a low-pass filter. It is sometimes called *smoothing circuit*, because the amplitudes of high-frequency components in a complex waveform are reduced, thus smoothing the jagged appearance of the waveform. This feature is useful for reducing high-frequency noise in a signal.

While the feedback resistor prevents integration of dc inputs, it also degrades the integration of low-frequency signals. At frequencies where the capacitive reactance of C is comparable in value to R_f, the net feedback impedance is not predominantly capacitive and true integration does not occur. As a rule of thumb, we can say that satisfactory integration will occur at frequencies much greater than the frequency at which $X_C = R_f$ [4.1]. That is, for integrator action we want

$$X_C << R_f$$

$$\frac{1}{2\pi fC} << R_f$$

or

$$f >> \frac{1}{2\pi R_f C} \tag{4.1}$$

The frequency f_C where X_C equals R_f,

$$f_C = \frac{1}{2\pi R_f C} \tag{4.2}$$

defines a *break frequency* in the Bode plot of the practical integrator. As shown in Figure 4.4, at frequencies well above f_C, the gain falls off at the rate of -20 dB/decade, like that of an ideal integrator, and at frequencies below f_C, the gain approaches its dc value of R_f / R_1.

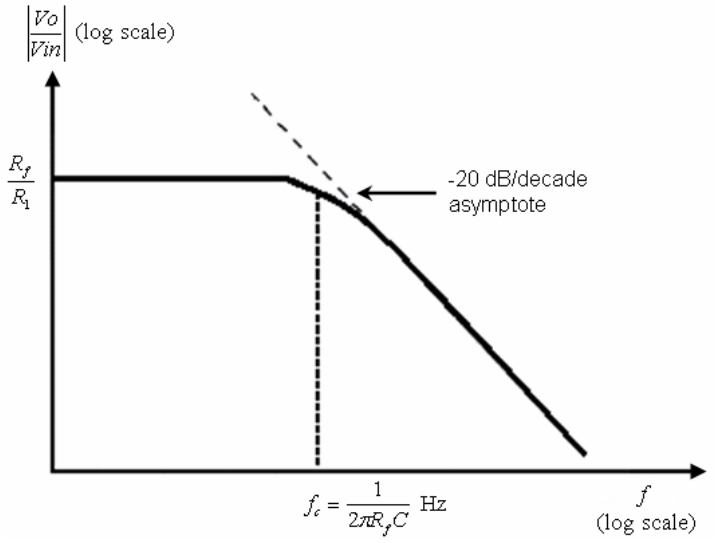

Figure 4.4. Bode plot for the practical integrator, showing that integration occurs at frequencies above $1/(2\pi R_f C)$ Hz.

Thus, to integrate signals with low frequencies such as down to 100 Hz, we require f_C << 100 Hz. Let us choose f_C one decade below 100 Hz. Then, from equation (4.2),

$$f_C = 10 = \frac{1}{2\pi R_f C}$$

If we choose C=10 nF. Then

$$10 = \frac{1}{2\pi R_f (10^{-8})}$$

$$R_f = \frac{1}{2\pi(10)(10^{-8})} = 1.59 \ M\Omega$$

The value of R_C is chosen depending on the maximum peak of the output voltage that is desired. In our case, the chosen R_C value was of 145 KΩ.

Once having the values of R_f and R_C, we need to find the input resistor value (*R1*), which will provide us the integration time value (τ) of the final integrator design.

To obtain this integration time value we performed several tests. These tests consisted in measuring the output voltage of the system without placing any object in front of the antenna (initial voltage), and then placing a metal plate (final voltage), to finally obtain the voltage difference produced with the different integration times. Table 4.2 shows test results obtained by keeping constant *C* (10 nF), and varying R_1. The best value for R_1 with a parabolic horn antenna (see Section 4.5.1), was of 10 KΩ giving us a τ of 0.1 milliseconds. Similar tests were made by using a rectangular horn antenna providing a τ of 3 milliseconds with a R_1 value of 300 KΩ. Table 4.3 shows the component values of the final integrator circuit.

Table 4.2. Test results to obtain the integration time value for the integrator design by using a parabolic (a) and a rectangular horn antenna (b). The best *R1* value in (a) was of 10 KΩ giving a τ of 0.1 ms, and the best *R1* value in (b) was of 300 KΩ providing a τ of 3 ms. The value of the feedback capacitor in both tests was kept constant to 10 nF.

R1 (KΩ)	Initial Voltage (V)	Final Voltage (V)	Difference (mV)
1	3.1822	3.1855	3.3
5	2.8046	2.8116	7.0
10	1.0570	1.0672	10.2
20	0.5880	0.5890	1.0
50	0.2650	0.2684	3.4
100	0.1398	0.1413	1.5
150	0.0921	0.0929	0.8
200	0.0707	0.0713	0.6
300	0.0465	0.0468	0.3
500	0.0224	0.0226	0.2

(a)

R1 (KΩ)	Initial Voltage (mV)	Final Voltage (mV)	Difference (mV)
82	269	280	11
160	126	142	16
300	81	117	36

(b)

Table 4.3. Component values of the final integrator circuit.

Component	Value
R1	300 KΩ
Rf	1.59 MΩ
C	10 nF
Rc	145 KΩ

4.3 Millimeter-wave lens

Millimeter-wave lenses are used in radiating systems to focus the radiation from primary sources into desired directions [4.2]. The basic function of the millimeter-wave lens is to form an image of the object being observed and then this image can be sampled by the Nipkow disc. In millimeter-wave lens, reflections from the dielectric can cause feed mismatch and power loss. As shown in Figure 4.5, reflections from the convex surface of the lens do not return to the source except for points at or near the axis. However, reflections from the plane surface are refocused at the lens and cause significant mismatch in the feed system, depending on the dielectric constant of the lens material. For normal incidence, the reflection coefficient is given by

$$|\Gamma| = \left|\frac{Z_L - Z_0}{Z_L + Z_0}\right| = \frac{\sqrt{\varepsilon_r} - 1}{\sqrt{\varepsilon_r} + 1} \tag{4.3}$$

Where $Z_0 = \eta_0 = \sqrt{\mu_0 / \varepsilon_0}$ and $Z_L = \eta = \sqrt{\mu_0 / \varepsilon_0 \varepsilon_r}$. For polystyrene: ε_r=2.6, Γ=0.2344; for alumina: ε_r=9.8, Γ=0.5158. Thus, for a small reflection coefficient, a low dielectric constant material is desirable.

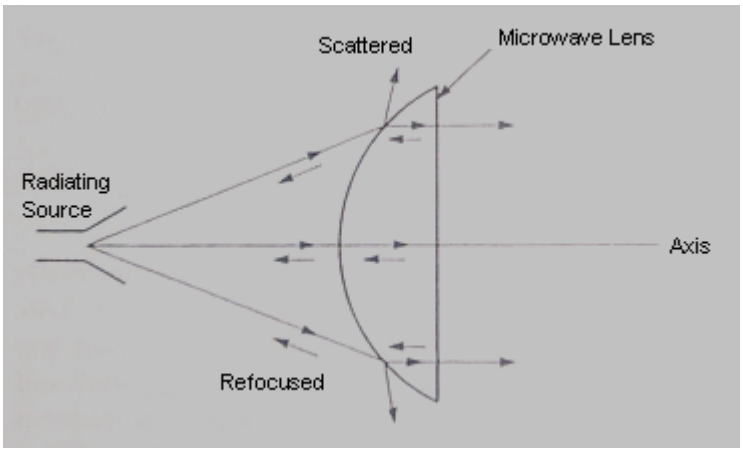

Figure 4.5. Reflected waves entering primary source. Reflections from the convex surface of the lens do not return to the source except for points at or near the axis. However, reflections from the plane surface are refocused at the lens and cause significant mismatch in the feed system, depending on the dielectric constant of the lens material.

To focus the radiation emitted by the object to the antenna, we used a millimeter-wave lens in our MMW imaging system. This lens is of plano-convex type and is made of *teflon* material, it has a diameter D = 16.2 cm and a curvature radius CR = 12.38 cm. We chose a plano-convex configuration because this kind of millimeter-wave lens configuration has different advantages in terms of fabrication simplicity such as reduced thickness (and consequently the overall weight of the lens). The *teflon* material has a permittivity ε_r = 2.1 and a refractive index n = 1.45 at millimeter-wave frequencies, covering the low permittivity characteristic explained in the preceding paragraph. The lens is covered with a metal ring of 2 cm of width to reduce the border reflections. Photographs of the millimeter-wave lens used are shown in Figure 4.6. This lens was provided by Dr. Soto from Instituto de Física of BUAP.

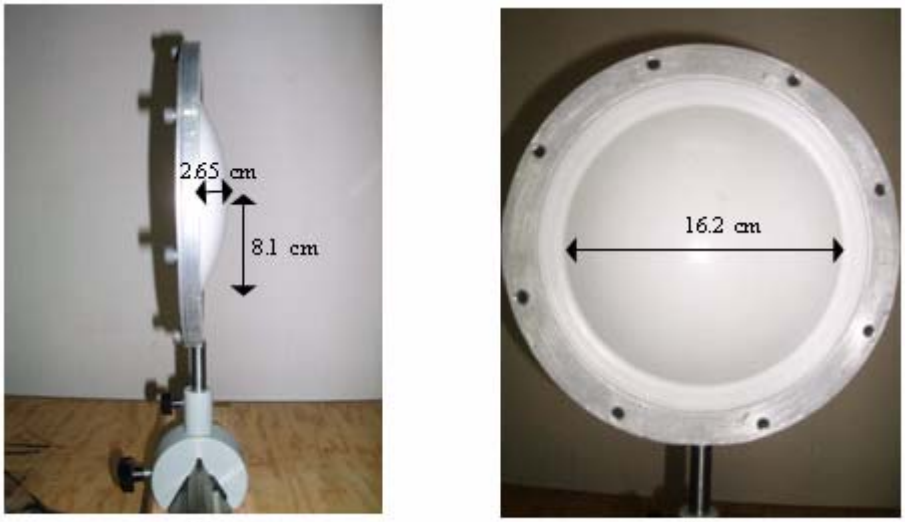

Figure 4.6. Lateral (a) and frontal (b) view of the millimeter-wave lens used in the MMW imaging system. The target's radiation is focused to the antenna by the lens. It is of plano-convex type and is made of *teflon* material (ε_r = 2.1, n = 1.45). Its dimensions are: D = 16.2 cm, CR = 12.38 cm.

To obtain the focal length the equation of the circle was used, as follows:

$$x^2 + (y - R)^2 = R^2$$

or, for $y << R$

$$R \approx \frac{x^2}{2y} \qquad (4.4)$$

The thin lens equation is given by:

$$\frac{1}{f} = (n-1)\left(\frac{1}{R_1} - \frac{1}{R_2}\right) \qquad (4.5)$$

From (4.4), the radius of the lens is:

$$R = \frac{(8.1)^2}{2(2.65)} = 12.38$$

By applying the previous result in (4.5), and knowing that R_1=∞ for plano convex lenses, the focal length is:

$$\frac{1}{f} = (1.45-1)\left(\frac{1}{\infty} - \frac{1}{-12.38\ \ cm}\right) = 0.03635\ \ cm^{-1}$$

or

$$f = 27.51\ \ cm$$

Experimentally this focal length was not used due to the maximum object detection was obtained by placing the objects at 24 cm away from the millimeter-wave lens.

4.4 Millimeter-wave absorber materials

As the name implies, millimeter-wave absorbing materials are coatings whose electrical and magnetic properties have been altered to allow absorption of millimeter-wave energy at discrete or broadband frequencies [4.3], [4.4].

Altering the dielectric and magnetic properties of existing materials will produce millimeter-wave absorbers. For the purpose of analysis, the dielectric properties of a material are categorized as its permittivity and permeability. Both are complex numbers with real and imaginary parts. Common dielectric materials used as absorbers have no magnetic properties (giving them the permeability of magnetic materials, such as ferrites, iron and cobalt-nickel alloys), which means they can be used to alter the permeability of the base

material. High dielectric materials, such as carbon, graphite and metal flakes, are used to modify the dielectric properties.

To optimize the use of absorbers in a design, there are two sets of parameters that should be critically analyzed: electrical and physical. Thus the goal of the absorber manufacturer is the compromise of the electrical performance, thickness, weight, and mechanical attributes of these materials with the final cost of the absorber.

Millimeter-wave absorbers are increasingly used to enhance shielding performance at higher frequencies. Products including elastomers, foams, thermoplastics and other custom solutions can aid with a wide variety of problems such as internal cavity resonances, antenna pattern shaping and high-frequency interference.

The millimeter-wave absorber used in our MMW imaging system was the *eccosorb AN-79* from *Emerson and Cuming Microwave Products Ltd* (see appendix A). It is made from polyurethane foam that is treated with carbon with the characteristics of lightweight, flexible, and broad bandwidth (from 0.6 to 40 GHz). It reflects less than -20 dB (<1%) of normal incident energy above specified bandwidth.

This absorber, which dimensions are 100 x 61 x 5 cm, has two behaviors depending on the mode used. In active approach the absorber helps to eliminate undesired reflections from the emitting sources as the LO and the millimeter-wave source, as explained in Chapter 7. In passive approach, the absorber introduces more undesired radiation rather than eliminate it. Thus, only in active approach the absorber is placed one meter away from the antenna and it is used as background to get more accurate measurements.

4.5 Principle of the MMW detector system

As discussed in Section 4.1, we sense objects of different materials, as shown in Figure 4.7.

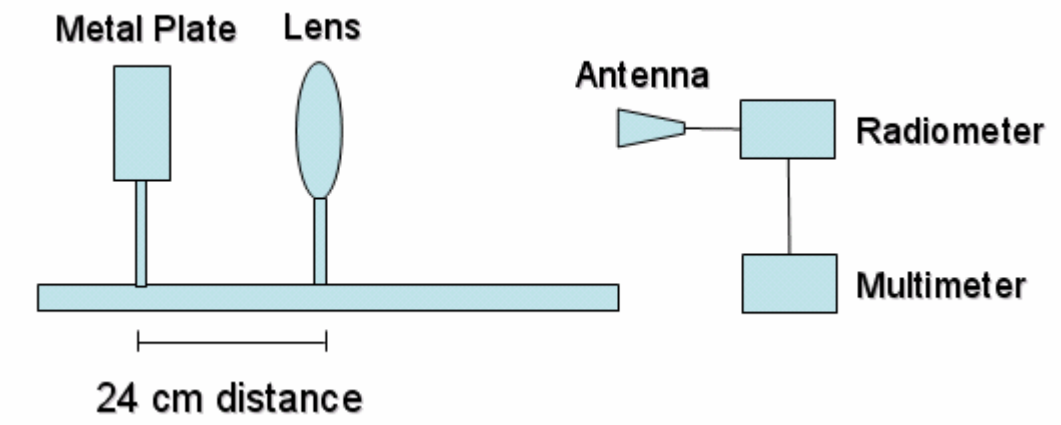

Figure 4.7. Setup for measuring the radiation of the objects.

The antenna detects the natural radiation which is emitted or reflected from the object at room temperature. Then the LNA receives this signal and provides a gain of 55 dB after which a mixer downconverts the frequency range from 4.3 to 5.359 GHz (this range is limited by the antenna and LNA bandwidths). By down converting the signal more sensitivity is obtained when compared to directly placing the detector after the LNA. Once the detector receives the signal, it converts it into a dc voltage which is directly proportional to the receiver input noise power, as mentioned in Section 2.1.4. Then this dc voltage is smoothed by the integrator and finally displayed in a HP 34401A digital multimeter.

As exhibited in Chapter 3, passive and active approaches were performed, whose configurations will be explained below.

4.5.1 Passive millimeter-wave (PMMW) approach

To measure the objects in PMMW approach three different types of antennas were used. For initial tests, we used a parabolic horn antenna. A photograph of this antenna is shown in Figure 4.8. The specifications of this antenna are not available. Experimental results are shown in the Chapter 7.

Figure 4.8. Photograph of the parabolic horn antenna used in the PMWW imaging system.

The second antenna employed was an antipodal Vivaldi antenna constructed by Colin et. al., [4.5]. The substrate used on this antenna was RT/duroid 5880® with relative permittivity (ε_r) of 2.2. The return loss of the antenna is under -7.5 dB in a bandwidth of 122% (from 10 to 37 GHz) with a microstrip transition of 50Ω. A photograph of the antenna is shown in Figure 4.9. The usage of this antenna allowed improvement of the measured results as we will also see in Chapter 7.

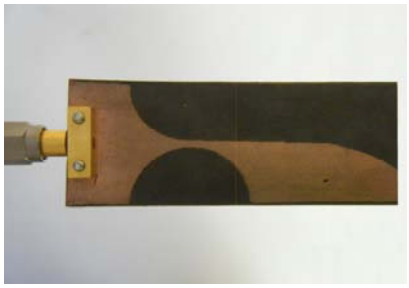

Figure 4.9. Photograph of the antipodal Vivaldi antenna used in the PMWW imaging system.

Finally a rectangular horn antenna was tested in the passive approach. This is a commercial available antenna from *Advanced Technical Materials, Inc*. It has a bandwidth of 18 to 40 GHz. The dimensions of the rectangle are 1.60 x 1.18 inches (4.06 x 3.00 cm) as illustrated in Figure 4.10. Photographs of the antenna are shown in Figure 4.11. With this antenna we obtained the best performance of our MMW detector system, as will discussed later in Chapter 7. Photographs of the final MMW imaging system are shown in Figure 4.12 and 4.13.

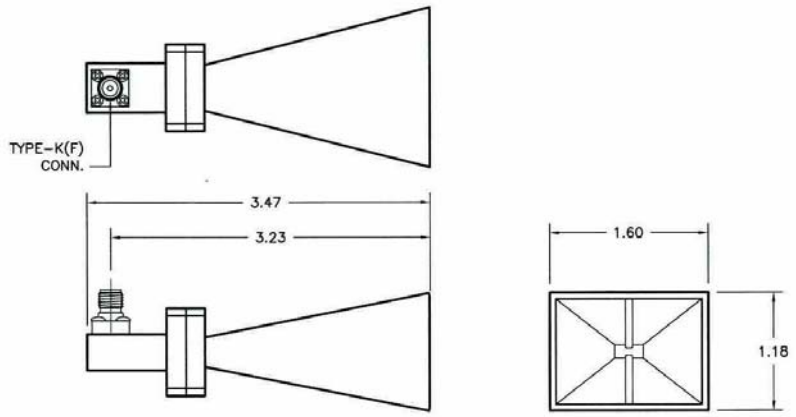

Figure 4.10. Dimensions in inches of the rectangular horn antenna used in the PMWW imaging system.

Figure 4.11. Photographs of the rectangular horn antenna used in the PMWW imaging system.

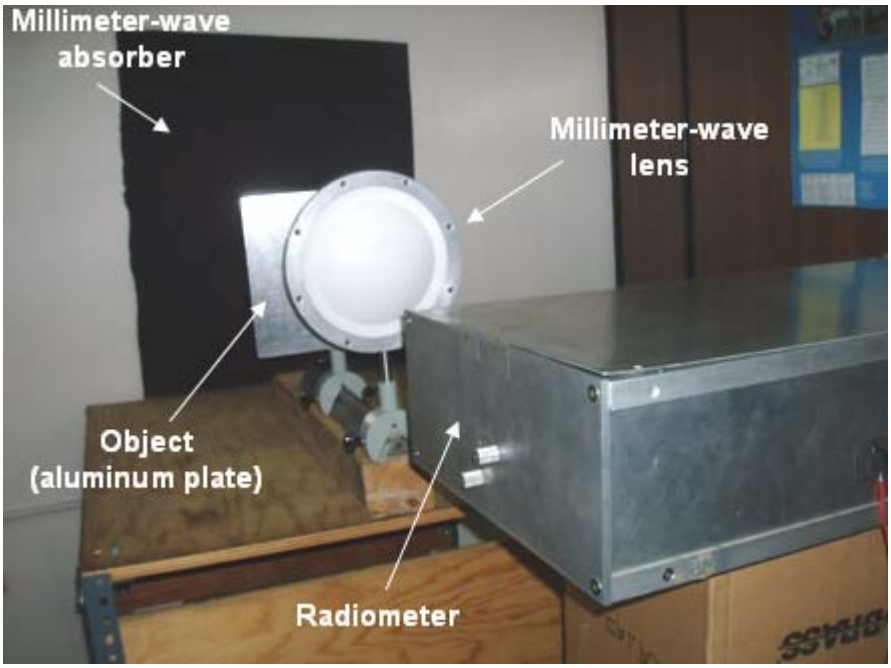

Figure 4.12. Photograph of the MWW detector system. The components are placed into a metal box for avoid noise distortions from the surroundings.

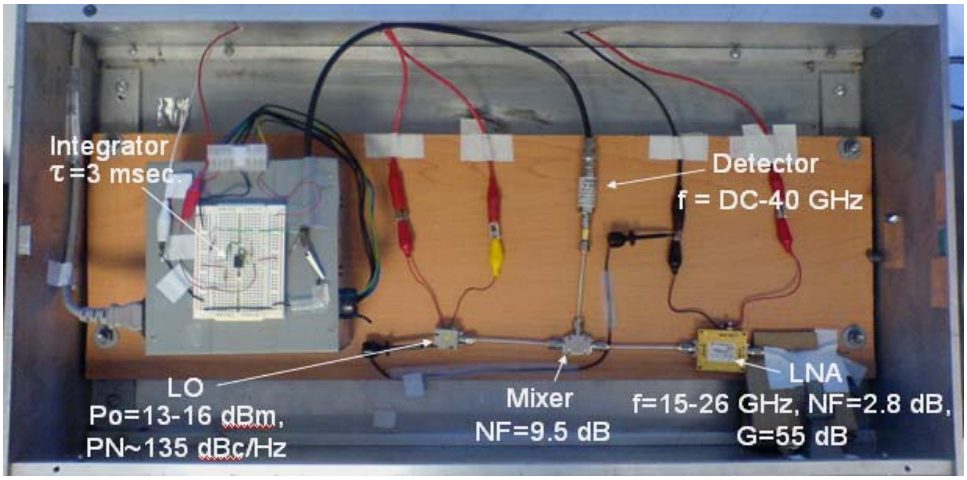

Figure 4.13. Photograph of the top view of the assembled radiometer.

4.5.2 Active millimeter-wave (AMMW) approach

As shown in Section 3.2.1.2, in AMMW imaging a source is needed to illuminate the scene under observation. For that purpose we used the same setting as the passive mode (using the rectangular horn antenna) but adding a millimeter-wave generator (HP8350B, from *Hewlett-Packard*) to radiate the object being measured. This generator has a variable frequency range from 0.01 to 26 GHz, and variable output power from -2 to 23 dBm (0.63 to 199.53 mW), with resolution power of 0.1 dBm (1.02 mW). The generator produces much higher powers than those emitted from the object being scanned, which means we can get greater contrast between the object and its surroundings. The diagram of the system in active mode is shown in Figure 4.14. We used the Vivaldi antenna (see Section 3.5) for transmitting power from the millimeter-wave generator. As the side lobes of the Vivaldi antenna produce distortion in the readings we had to cover it with metal paper to eliminate these lobes. Full experimental results are shown in Chapter 7.

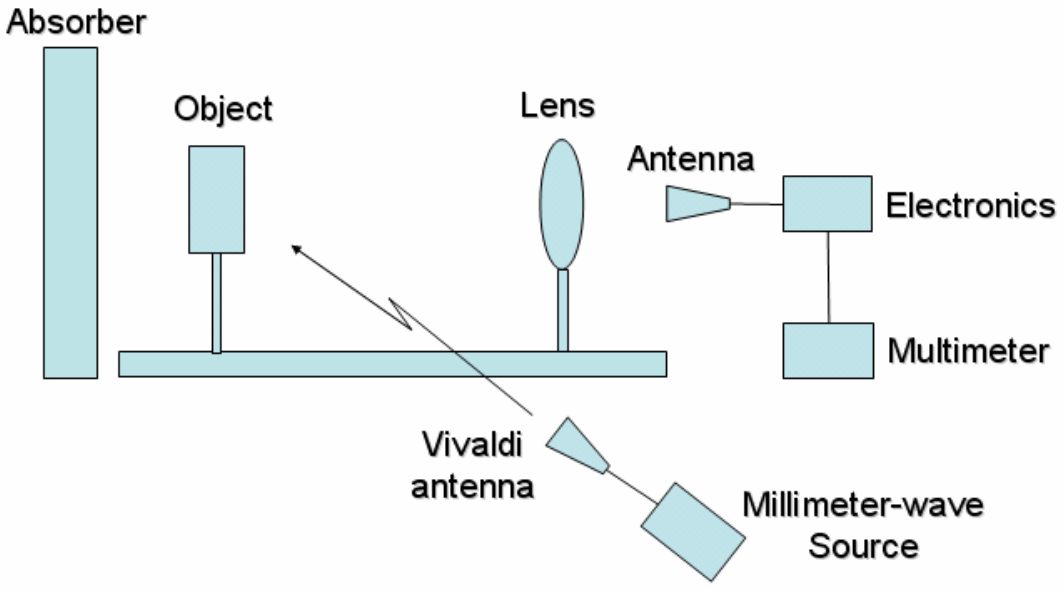

Figure 4.14. Diagram of the MMW imaging system in active mode.

4.5.2.1. EM radiation effects on biological tissues

The main concern of radiation in active approach is related to health and safety of biological tissues. Due to this, a special analysis has to be made according to the international safety standards, when active approach is performed.

The IEEE has released safety standards to regulate the emissions of microwave radiation.

The IEEE C95.1-2005 is one of the safety standards for RF/microwave human exposures [4.6]. The complete name is Standard for Safety Levels with Respect to Human Exposure to Radio Frequency Electromagnetic Fields, 3 kHz to 300 GHz. This standard contains exposure limits for electric fields and magnetic fields that are whole-body and time averaged. This standard specifies that, for a frequency range of 3 kHz to 300 GHz, the radiated power density must not exceed 10 mW/cm² as shown in Figure 4.15. As it can be also seen from Figure 4.15, the radiation allowance for humans is much lower at longer wavelengths.

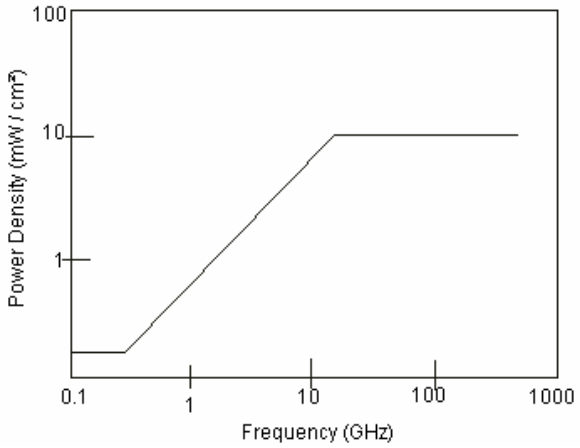

Figure 4.15. Graph of radiated power density vs. frequency. The radiated power density must not exceed 10mW/cm².

The evaluation of the field can be done in the far field area using the far field computation rules. For this analysis, the human subjects are located in the far field of the antenna. At this distance from the system, the electrical and magnetic fields can be regarded as being established and a spherical wave as being diffused.

The EIRP (Equivalent Isotropic Radiated Power) of the millimeter-wave source (HP8350B) used in the AMMW imaging system can be obtained as follows:

$$EIRP = P_T + G_a \tag{4.4}$$

$$EIRP = 23\ \ dBm + 5\ \ dBi = -7\ \ dBW + 5\ \ dBi = -2\ \ dBW = 630.96\ \ mW$$

Where P_T is the maximum Transmit power of the source and G_a is the gain of the used antenna. In this case, the horn antenna (mode 180-442-KF, from *Advanced Technical Materials, Inc*) has G_a=5dBi at the center frequency (26GHz). At the axis of the antenna where the field is at its maximum and is located for example to 10 cm away from the antenna, the maximum measurable power density is therefore obtained by the following formula [4.7]:

$$D = \frac{EIRP}{4\ \pi\ d^2} = \frac{630.96\ \ mW}{4\pi(10\ \ cm)^2} = 0.50\ \ {mW}/{cm^2} \tag{4.5}$$

From this result, it can be stated that in the worst-case scenario (Maximum

transmit power at 10cm distance) the power density generated by the system will never exceed 1/20 of the maximum permissible limit (see figure 4.14). These findings show that the AMMW imaging system therefore has potentially no health hazard on persons using it. However if any changes were made to the setup newer calculations should be computed.

References

[4.1] T. F. Bogart, “Electronic Devices and Circuits,” 4th ed., Ed. Prentice-Hall, Inc., 1997.

[4.2] P. Bhartia & I. J. Bahl, “Millimeter Wave Engineering and Applications,” Ed. John Wiley & Sons, Inc.,

[4.3] http://www.epn-online.com/page/32228/microwave-absorber-does-exactly-what-it-says-on-the-tin.html

[4.4] A. V. Vorst, A. Rosen, and Y. Kotsuka, “RF/Microwave Interaction with Biological Tissues,” 1st. ed., Ed. John Wiley & Sons, Inc., 2006

[4.5] Edgar Colin-Beltran, Alonso Corona-Chavez, Reydezel Torres-Torres, Ignacio Llamas-Garro, “A wideband antenna array with novel 3dB branch-line power dividers as feeding network”, International Workshop on Antenna Technology (Small Antennas and Novel Metamaterials), IWAT 2008, March 4-6, 2008, Chiba, Japan, pp. 267-270.

[4.6] IEEE Std C95.1-2005 “IEEE Standard for Safety Levels with Respect to Human Exposure to Radio Frequency Electromagnetic Fields, 3 kHz to 300 GHz," *IEEE*, pp. 1-238, 2006

[4.7] F.T. Ulaby, R. K. Moore, and A. K. Fung, “Microwave Remote Sensing: Active and Passive, Volume I, Microwave Remote Sensing Fundamentals and Radiometry,” Artech House, 1981.

Chapter V

Substrate Integrated Waveguide Exponential Flare Horn Antenna

In this chapter the Substrate Integrated Waveguide (SIW) Exponential Flare Horn Antenna design will be explained. It begins with an explanation of the Substrate Integrated Circuit (SIC) technology. Then proceeds to explain the narrow bandwidth SIW flare horn antenna already proposed in the literature, and our new proposed wide bandwidth design. Full simulation and optimization of this latter antenna are shown along with a comparison with the current state of the art of antennas.

5.1 SIC's Technology

At millimeter-wave frequencies, the classical waveguide technology has two fundamental problems, namely, radiation loss due to discontinuity, and difficult modal transition to planar circuits. Subsequently the concept of a new generation of high frequency integrated circuits called "substrate integrated circuits - SIC's" has been developed. This new concept has unified the hybrid and monolithic integrations of various planar and non-planar circuits that are made in single substrate and/or multilayer platforms.

SIC's architecture can serve as the design base for a broad range of hybrid planar/non-planar circuits for millimeter-wave applications. As a matter of fact,

the SIC technology can greatly facilitate interconnects and integrations between planar and non-planar circuits, which can be made in a single fabrication process. At the same time, this scheme can be used to design low cost high performance (high Q) passive circuits such as resonators [5.1], filters [5.2], couplers [5.3], power dividers [5.4], circulators [5.5], and antennas [5.6].

The SIC concept can be used to synthesize almost all kinds of waveguide by simply using air holes (or other material filled holes) and metallized holes. Furthermore, most of these synthesized waveguides are interconnected to planar circuits with simple transitions that are also fabricated on the same dielectric substrate. Since this technology is compatible with many fabrication processes we can expect strong and growing interests in it for many high frequency applications.

5.1.1 SIC's Concept

The fundamental of the SIC's concept is to synthesize non-planar structure with a dielectric substrate and make it in planar form, which is completely compatible with other planar structures [5.7]. This can usually be achieved by creating artificial waveguiding channels. In this case, alternated dielectric constant profiles of substrate using air holes or composite dielectric media and/or synthesized metallic walls using metallized vias are generally fabricated. The resulting structure on the substrate will be a planar waveguide, which has much better loss characteristics than planar counterparts, allowing for the design of millimeter wave high Q circuits using a low cost fabrication technique. Furthermore, the synthesis of a non-planar waveguide in a substrate permits the realization of efficient wideband transitions between the synthesized non-planar waveguide and planar circuits

such as microstrip and coplanar waveguide (CPW) integrated circuits. With these transitions, the complexity and cost of interconnection between non-planar high Q circuits and planar circuits is reduced to a minimum.

Another potential advantage of the SIC technology is that the planar circuits could easily be combined with many types of SIC's on the same dielectric substrate so to achieve high efficiency and high density millimeter wave integrated circuits in which antenna, circulator, filters, attenuators, amplifiers and mixer and many other circuits are all integrated.

Finally, the SIC concept is compatible with many existing fabrication processes including the microwave integrated circuit (MIC) fabrication technique, the thin film ceramic process, the HTCC and LTCC technologies and the microwave monolithic integrated circuit process (MMIC). Generally, the critical aspect of fabricating SIC circuits is the positioning of the holes or vias along the substrate that should be controlled adequately, as exhibited below.

5.1.2 Substrate Integrated Waveguide (SIW)

It is known that the proposed integration schemes of the conventional rectangular waveguide with planar structures are bulky and usually require a precision machining process, which is difficult to achieve at millimeter-wave frequencies for mass production. A straightforward solution is to integrate the rectangular waveguide into microstrip circuit substrate as we have mentioned in the above section. This will surely reduce the Q factor of waveguide compared with the hollow rectangular waveguide because of the dielectric filling and volume reduction [5.8]. The whole circuit including planar circuitry, transitions and waveguides can be, however, constructed using standard

PCB or other planar processing techniques. In addition, the transmission loss of the substrate transitions may be much lower than that of the transitions or coupling sections made between the conventional waveguide and planar circuits.

5.1.2.1 SIW design rule

The rectangular waveguide is synthesized by placing two rows of metallized holes in the substrate, as illustrated in Figure 5.1. The diameter *D* of the holes, the spacing *p* between the holes, and the spacing W between the two rows are the physical parameters necessary for the design of the guide. The pitch *p* must be kept small to reduce the leakage loss between adjacent posts. However, the post diameter *D* is also subject to the loss problem. Due to the synthesis, the SIW can no longer be regarded as a normal waveguide, and it is in fact an artificial waveguide. Therefore, the post diameter may significantly affect the return loss of the waveguide section in view of its input port. Two design rules related to the post diameter and pitch are used to neglect the radiation loss [5.7]. These rules have been deducted from simulation results of different SIW geometries.

$$D < \lambda_g / 5 \tag{5.1}$$

where λ_g is the guided wavelength, and

$$p \leq 2D \tag{5.2}$$

These two rules ensure that the radiation loss be kept at a negligible level. In this case, the SIW can be modeled by a conventional rectangular waveguide (RW). When following the two above rules, the mapping from the SIW to the RW is nearly perfect in all the single mode bandwidth. All the existing design

procedures and theoretical frameworks developed for the rectangular waveguide are directly applicable to its synthesized counterpart. Nevertheless, dielectric filling effects and geometrical particularity of the synthesized waveguide should be accounted for coupler and antenna designs. Finally, a nonessential but desirable condition for the manufacturing process is to minimize the number of holes. These holes are usually mechanically drilled and chemically electroplated, and the production time is proportional to their number.

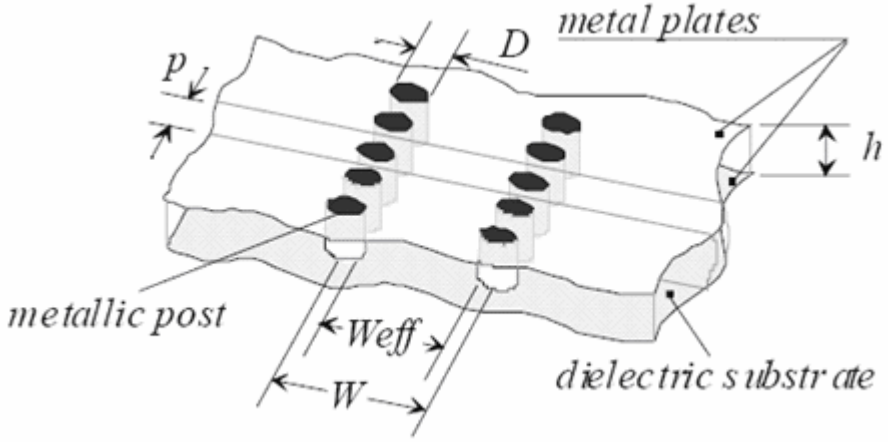

Figure 5.1. Topology of an SIW guide realized on a dielectric substrate with its physical dimensions (from [5.7]).

5.1.2.2 SIW transitions

SIW guide can easily be integrated with active devices because the design of transition between the SIW guide and the planar technology is straightforward. The first transition presented has involved a microstrip line [5.9]. The microstrip transition is a wideband structure, covering the entire useful bandwidth of the SIW guide. This transition structure makes use of a tapered microstrip line to excite the waveguide mode as illustrated in Figure 5.2a. With low thickness substrate, the conductor loss in the waveguide

section cannot be neglected and to reduce it, the thickness must he increased. The coplanar waveguide (CPW) to SIW transition [5.10], is shown in Figure 5.2b. It consists of a coplanar waveguide section with 90° bend on each slot. A stub is added on the CPW line to match the transition and the rectangular waveguide is designed with via holes. However, this transition exhibits a narrower bandwidth compared to the microstrip counterpart. Thus, for our antenna design we have used the microstrip transition to obtain the desired wide bandwidth, as mentioned in section 5.3.

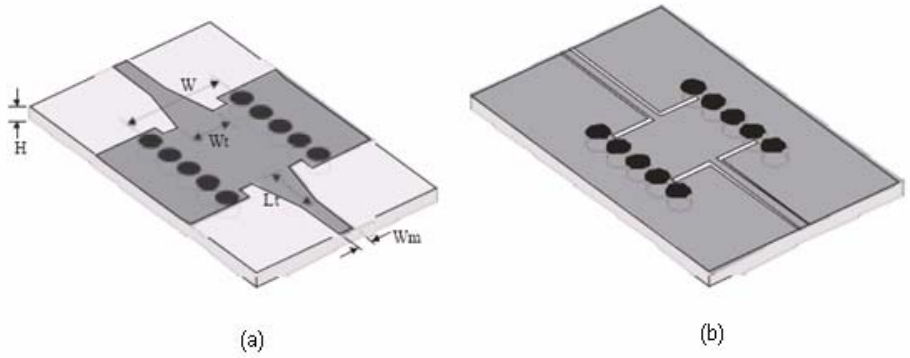

Figure 5.2. Integrated transitions from planar circuits to SIW guide. (a) Microstrip transition and (b) Coplanar waveguide transition (from [5.7]).

5.2 SIW flare horn antenna

Taking into account the concepts showed in Section 5.1, we can use SIC technology to integrate an antenna with its transition on the same substrate. One example of this is the SIW flare horn antenna fabricated by Che et. al., [5.6]. These authors proposed a SIW flare horn antenna with dielectric lens which has a bandwidth from 25.5 to 28.5 GHz and central frequency at 27 GHz. This lens shares the same substrate with the horn antenna. The simulated model of the antenna is illustrated in Figure 5.3.

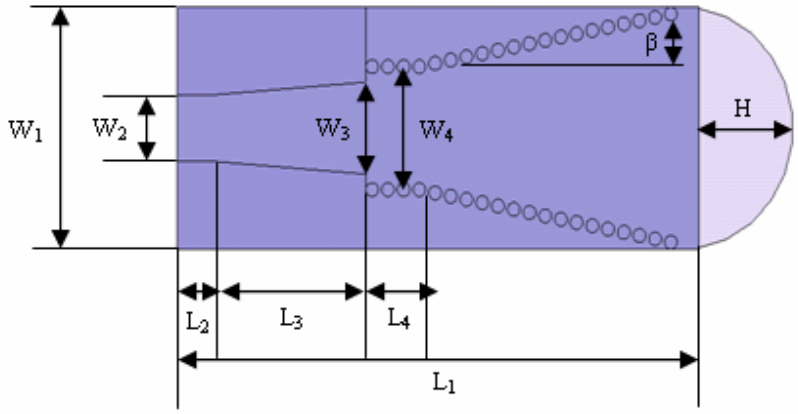

Figure 5.3. Geometry of the SIW flare horn antenna proposed by Che et. al. [5.6]. W_2 =3.8mm, L_2 =2mm, W_3 =5.32mm, L_3 =10mm, W_4 =7.112mm, L_4 =3.4mm, H =6mm, β =10°, L_1 =14mm, W_1 =33.175mm, h =2 mm^3.

The substrate integrated rectangular waveguide (SIRW) was made following the design rules explained in ref. [5.7] and [5.9]. The dimensions of the SIRW are: width W_4=7.112 mm, length L_4=3.4mm, cylinder radius r=0.4mm, cylinder separation p=1mm, width of the horn W_1=14mm, substrate thickness h=2mm, and dielectric constant ε_r=10.2. The tapered-transition from 50 Ω microstrip feed line was designed to provide a low loss transition to the SIRW on the same substrate. The width of the microstrip is W_2=3.8mm, and length L_2=2mm. The taper transition length is L_3=10mm, and the larger width W_3=5.32 mm. The overall dimensions of the horn antenna including the arc lens are 39.175 x 14 x 2 mm^3. Following the procedure for a conventional horn antenna [5.11], the flare angle of the horn chosen by the authors was β=10°. Based on the operation principle of the optical focus [5.12], the arc lens is placed before the radiation plane to improve the directivity of the horn antenna.

In [5.6] a numerical investigation is presented to find the relation between the H-plane beamwidth and the arc height with a commercial finite element method package [5.13] as shown in Table 5.1. As we can see, the beamwidth of the radiation pattern is dependent on the arc height of the dielectric lens, i.e., stronger arc height results in narrower beam. We may note that, the arc height cannot exceed half of the horn width, beyond which the dielectric lens is not a normal arc and would result in the deterioration of the radiation pattern.

Table 5.1. The relation between the height *H* of the dielectric arc lens and the H-Plane Beamwidth (HPBW).

H (mm)	HPBW (°)
0	160
1	150
2	140
3	135
4	90
5	80
6	75
7	68

The experimental antenna prototype was compared with simulated results. The H-plane and E-plane radiation patterns at 27 GHz are shown in Figure 5.4. The measured gain is about 9 dB, close to the simulation result, and the front-to-back ratio is about -15 dB. The beamwidths, H and E planes for both simulated and measured, are quite similar, at about 60°. The antenna prototype also has a bandwidth of 12%, obtaining better measured return loss S_{11} than the simulated (Figure 5.5). However, at around 27.5 GHz the response worsens. This is probably due to fabrication inaccuracies of the dielectric arc and the SIRW horn antenna in the substrate.

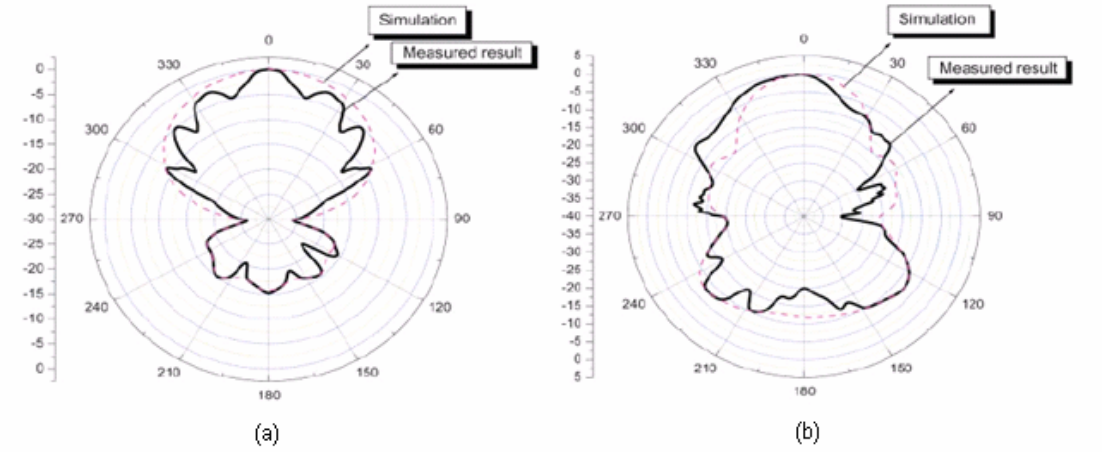

Figure 5.4. The measured and simulated radiation patterns of the SIW flare horn antenna at 27 GHz. (a) E-plane, (b) H-plane (from [5.6]).

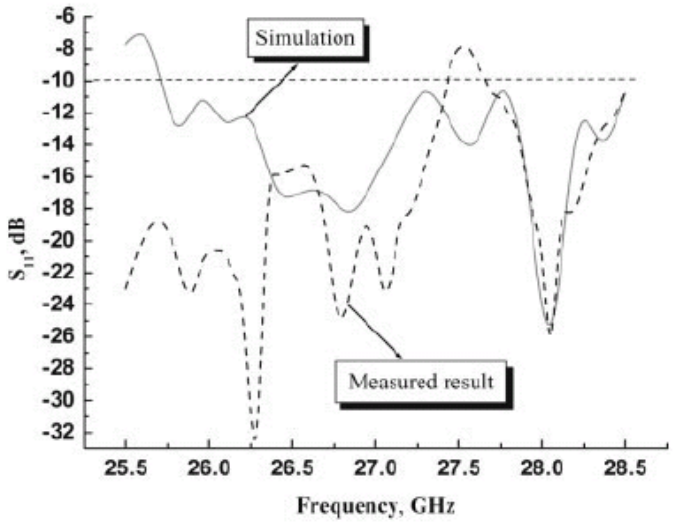

Figure 5.5. The measured and simulated return loss S_{11} of the SIW flare horn antenna (from [5.6]).

This prototype allows the very compact design of a completely integrated planar platform of horn antenna and its feeding structure on the same substrate without any mechanical assembly or tuning. The only disadvantage of this model is the narrow bandwidth (25.5-28.5 GHz), which is not useful for our application.

5.3 SIW exponential flare horn antenna: proposed design

5.3.1 Design of the SIW exponential flare horn antenna

One of the requirements which has become a very critical design issue in the passive MMW imaging systems is the wide bandwidth. A broadband MMW imaging system allows us to have a greater detection range of objects made with different materials as the emissivity of each material is different. Moreover, greater bandwidth detection translates into more receiving power to be integrated and hence greater system sensitivity. Finally, wide bandwidth systems are more immune to noise due to their spectral characteristics.

For these reasons, we propose a design of a wide bandwidth SIW horn antenna for our MWW imaging system. We have used the design of the antenna performed by Che et. al., [5.6], however, we modified it by introducing exponential flares to have a wide bandwidth.

We took the Vivaldi antenna concept to obtain the exponential flare of our antenna design. The Vivaldi antenna is a special type of tapered slot antenna with exponential flare profile [5.14].

The slot flare is tapered exponentially with the opening rate *R*, of which the shape is determined by

$$y = c_1 e^{Rx} + c_2 \tag{5.3}$$

where, c_1 and c_2 are determined by the coordinates of the first and last point of the exponential curve.

We also changed from the original design the dimensions of the SIRW, the total length (L_1) and width of the antenna (W_1), and the arc height of the lens (H).

The simulation of the proposed antenna was also made in a commercial finite element method package [5.13]. Figure 5.6 represents the simulated model of the antenna. The new SIRW dimensions are W_4=6.312mm, L_4=3.4mm, cylinder radius r=0.5mm, and cylinder separation p=1.2mm, substrate thickness h=2mm, and dielectric constant ε_r=10.2. The new width of the antenna is W_1=19.4mm, and the arc height of the lens is H=8.6 mm. The overall dimensions of the horn antenna including the arc lens are 41.775 x 19.4 x 2 mm^3. Changing these values and by using the exponential flares, we obtained the desired broad bandwidth antenna.

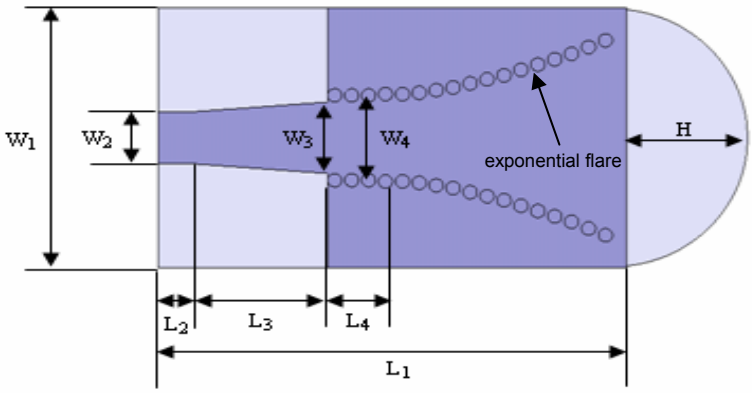

Figure 5.6. Geometry of the SIW exponential flare horn antenna. W_2 =3.8mm, L_2 =2mm, W_3 =5.32mm, L_3 =10mm, W_4 =7.112mm, L_4 =3.4mm, H =6mm, L_1 =41.775, W_1 =19.4, h =2 mm^3.

These parameters of design were chosen by taking into account the physical materials for constructing the antenna that are commercially available. For that purpose we have found a substrate (RT/duroid 6010LM, from *Rogers Corporation*) which has a ε_r=10.2, and susbtrate thickness h=1.905 mm. We also found the values for D and p that are commercially available and follow

the SIW design rules discussed in Section 5.1.2.1. From ec. (5.1) and knowing that λ_g = 11.54 mm [5.15], we obtain:

$$D < \frac{\lambda_g}{5} = \frac{11.54\ \ mm}{5} = 2.308\ \ mm$$

Thus, a cylinder diameter less than 2.3 mm has to be chosen. The minimum commercial diameter of copper wire available is of 1 mm, thus a cylinder diameter of 1 mm can be selected. Once we chose the cylinder diameter, we have to verify if that value follows the second design rule. From ec. (5.2), the separation *p* between the cylinders is:

$$p \leq 2D = 2\left(1\ \ mm\right) = 2\ \ mm$$

Thus, a *p* value of 1.2 mm can be chosen.

5.3.2 Simulation of the SIW exponential flare horn antenna

As said in the preceding Section, the simulation of the antenna was made in a commercial finite element method package [5.13]. The most difficult part for optimizing was the opening rate *R* of the exponential flares (see Section 5.3). To do so, several simulations with different *R* values were performed to obtain the desired wide bandwidth. The best *R* value was of 0.8 cm^{-1} and by using this value and the antenna design shown in below Section was obtained the best response of the return loss S_{11} in a broad frequency band. The return loss S_{11} response and the antenna radiation pattern are illustrated in Figures 5.7 and 5.8, respectively. As shown in Figure 5.7, this antenna has a wide

bandwidth from 18 to 40 GHz, having a good response of the return loss S_{11} (under -10 dB approximately). The arc lens placed in the substrate improves the directivity of the SIW antenna as shown in Figure 5.8.

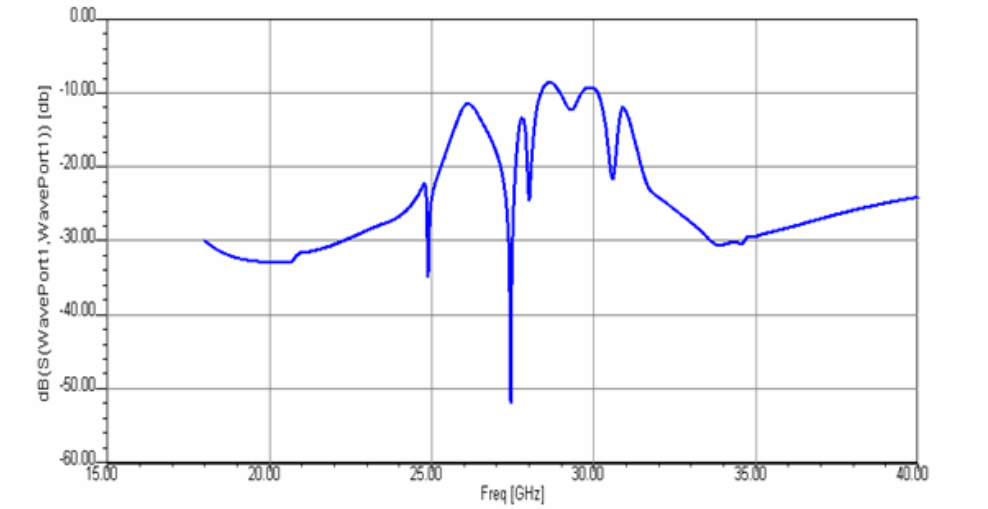

Figure 5.7. Return Loss S_{11} of the proposed ISW exponential flare horn antenna.

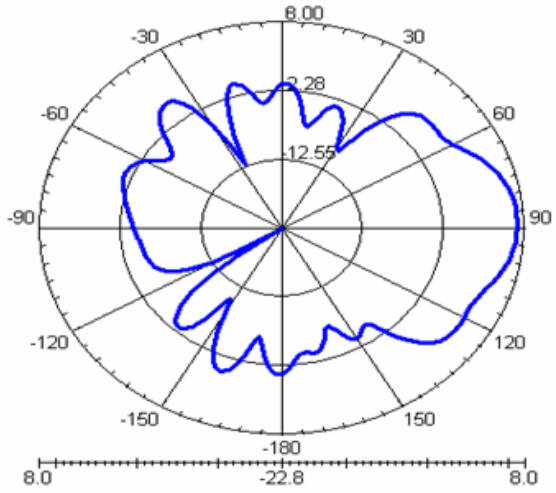

Figure 5.8. Radiation pattern of the proposed ISW exponential flare horn antenna.

It also was simulated an antenna with another commercial substrate (RT/duroid 5880 from *Rogers Corporation*) which has a dielectric constant ε_r=2.2 and substrate thickness h=0.381mm but could not be obtained good response in the return loss S_{11}. Here, the best result obtained was a return loss of -2.6 dB in the desired bandwidth as shown in Figure 5.9.

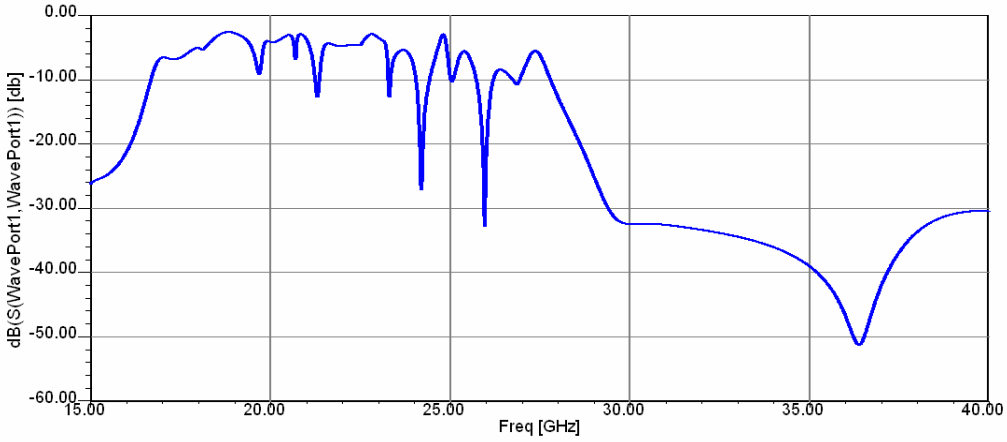

Figure 5.9. Return Loss S_{11} of the proposed ISW exponential flare horn antenna with dielectric constant ε_r=2.2 and substrate thickness h=0.381mm.

References

[5.1] Y. Cassivi, L. Perregrini, K. Wu, and G. Conciauro, "Low-Cost and High-Q Millimeter-Wave Resonator Using Substrate Integrated Waveguide Technique," *IEEE 32nd European Microwave Conference*, pp. 1-4, Oct. 2002.

[5.2] X. Zhang, J. Xu, Z. Yu, and Y. Dong, "Microstrip Wide Band-pass Filter Based on Substrate Integrated Waveguide (SIW)," *IEEE International Symposium on Microwave, Antenna, Propagation, and EMC Technologies For Wireless Communications*, pp. 209-211, August 2007.

[5.3] X. Xu, R. G. Bosisio, and K. Wu, "A New Six-Port Junction Based on Substrate Integrated Waveguide Technology," *IEEE Transactions on Microwave Theory and Techniques*, vol. 53, no. 7, pp. 2267-2273. July 2005.

[5.4] Z.Hao, W. Hong, H. Li, H. Zhang, and K. Wu, "Multiway broadband substrate integrated waveguide (SIW) power divider," *IEEE 2005 Antennas and Propagation Society International Symposium*, vol. 1A, pp. 639 – 642, July 2005.

[5.5] W. D'Orazio, K. Wu, and J. Helszajn, "A Substrate Integrated Waveguide Degree-2 Circulator," *IEEE Microwave and Wireless Components Letters*, vol. 14, no. 5, pp. 207-209, May 2004.

[5.6] W. Che, B. Yao, and Y. L. Chow, "Substrate Integrated Waveguide Horn Antenna with Dielectric Lens," *Microwave and Optical Technology Letters*, vol. 49, no. 1, pp. 168-170, Jan. 2007.

[5.7] K. Wu; D. Deslandes, and Y. Cassivi, "The Substrate Integrated Circuits - A New Concept for High-Frequency Electronics and Optoelectronics," *Telecommunications in Modern Satellite, Cable and Broadcasting Service, 2003. TELSIKS 2003. 6th International Conference*, vol. 1, pp. III-X, Oct. 2003.

[5.8] W. Che, K. Deng, E. K. N. Yung, and K. Wu, "H-Plane 3-dB Hybrid Ring of High Isolation in Substrate-Integrated Rectangular Waveguide (SIRW)," *Microwave and Optical Technology Letters*, vol. 48, no. 3, pp. 502-505, March 2006.

[5.9] D. Deslandes, and K. Wu, "Integrated Microstrip and Rectangular Waveguide in Planar Form," *IEEE Microwave and Wireless Components Letters*, vol. 11 no. 2, pp. 68-70, Feb. 2001.

[5.10] D. Deslandes and K. Wu, "Integrated Transition of Coplanar to Rectangular Waveguides", *IEEE 2001 International Microwave Symposium Digest*, vol. 2, pp. 619-622, May 2001.

[5.11] K. Nagasawa, and I. Matsuzuka, "Radiation Field Consideration of Biconical Horn Antenna with Different Flare Angles," *IEEE Transactions on Antennas and Propagation*, vol. 36, no. 9, pp. 1306-1310, Sep. 1988.

[5.12] M. Born, and E. Wolf, "Principles of Optics," 6th ed., Ed. Pergamon, 1980.

[5.13] "*Ansoft HFSS*, version 9," Ansoft Corporation 2003.

[5.14] S. G. Kim, and K. Chang, "Ultra wideband 8 to 40 GHz beam scanning phased array using antipodal exponentially-tapared slot antennas," IEEE Microwave Symposium Digest, vol. 3, pp. 1757-1760, June 2004.

[5.15] S. Y. Liao, "Microwave Devices and Circuits," 3rd. ed. Ed. Prentice Hall, pp. 106-110, 2004.

Chapter VI

Nipkow Disc

This chapter begins by giving a brief description of the Nipkow disc device, and then proceeds to treat the Nipkow disc system designed for the MMW imaging system. Finally it will be discussed the Nipkow disc system implementation at millimeter frequencies.

6.1 Theoretical Introduction

Nowadays, there are several methods for image acquisition in MMW imaging. Early systems used single detectors at the focal plane, the detector being mechanically scanned across the scene of interest. Due principally to the slow mechanical scan motion, these systems usually took minutes to take single-frame images. The present goal in millimeter-wave imaging research is to drastically reduce the image acquisition time in order to approach TV frame rates. One of the important approaches being investigated to reach this goal is the use of focal plane solid-state arrays with individualized amplification and detection. The other important approach is the combination of raster motion and a single receiver channel. The raster motion is either of the image in front of a fixed receiver by means of a flapping reflector [6.1], [6.2] or of the receiver in front of a fixed image [6.3], [6.4].

Although millimeter-wave imaging is mostly dominated by focal plane arrays, there are, however, several problems associated with them, like high cost,

large size, complexities associated with interchannel gain stability, and others [1, 3], so that, as present, the field remains dominated by scanned systems; however, their success awaits the discovery of a compact and efficient scanner capable of achieving video rates.

The Nipkow disc is a possible solution to achieving these video rates. The Nipkow disc was a device which its inventor, Paul Nipkow, thought could be used to transmit pictures by wire (1884), [6.5]-[6.7]. The device consists of a mechanically spinning disc of any suitable material (metal, plastic, cardboard, etc.), with a series of equally distanced circular holes of equal diameter drilled in it as illustrated in Figure 6.1. These holes are positioned to form a single-turn spiral starting from an external radial point of the disc and proceeding to the center of the disc, much like a gramophone record. When the disc rotates the holes trace circular ring surfaces. Each hole in the spiral takes a horizontal "slice" through the image which is picked up as a pattern of light and dark by a sensor. By spinning the disc rapidly enough, the object seems complete, in a way similar to cinematography, and capturing of motion becomes possible. The resolution of the image depends only on the number of holes of the Nipkow disc.

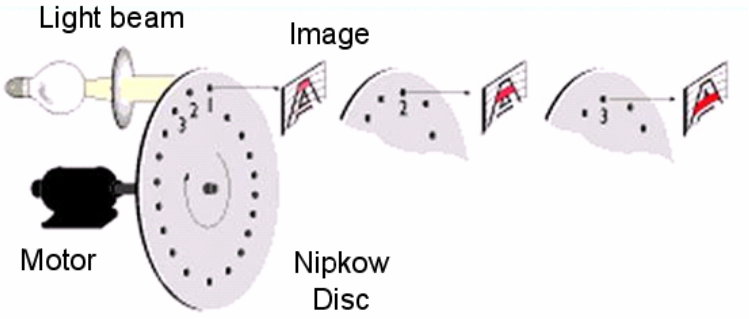

Figure 6.1. Nipkow disc diagram. The image (letter A), is scanned in slices by each hole in the spiral to reconstruct the w hole image.

6.2 Design and implementation of the Nipkow Disc

A Nipkow disc system at the optical region was first designed by Soto et. al. and proposed to be used at mm waves [6.8]. As convenience the explanation of the Soto's work is closely reproduced here. The authors propose a scheme for raster-scanned image acquisition in which neither the image nor single channel receiver has to be scanned, and whose maximum frame rate will be determined ultimately by the speed and sensitivity of the single channel receiver, and not by mechanical motion limitations. The original system has two principal components to distinguish: the Nipkow disc and an integrating sphere.

The Nipkow disc, as discussed in Section 6.1, is provided with a number of spirally distributed sampling holes, and it is utilized for scanning the object under observation. It has N sampling holes having a uniform angular distribution around the disc. Their radial positions vary successively from r_{min} to r_{max}, with uniform increments of magnitude given by $\Delta r = (r_{min} - r_{max})/(N - 1)$. Thus, for the ith hole, its radial position is $r_i = r_{min} + (i - 1)\Delta r$, where $i = 1, 2, \ldots, N$. This is represented graphically in Figure 6.2. An opaque mask is to be placed at the back of the rotating disc. This mask contains a window, designated by *abcd* in the Figure 6.2, which represents the scanning area of interest. Its shape, a truncated circular slice, has an angular dimension such that only one of the sampling holes appears in it a time, and when it disappears from view, the following one immediately appears on the opposite side of the window in the next row. The number of curved rows in the scanning is directly determined by, and is equal to, the number N of the sampling holes, as said in Section 6.1, while the number M of columns is determined by the number of measurements taken within the angular displacement equal to $2\pi/N$ of the disc, and can be programmed at

convenience. Thus, the maximum integration time per sample allowed for the single-channel receiver is $2\pi/\omega NM$, where ω is the angular speed of the disc.

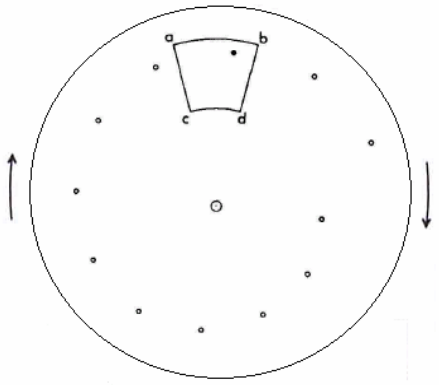

Figure 6.2. Representation of the rotating disk with 12 sampling holes (from [6.8]). Only the hole within the window *abcd* is active; the rest of them are assumed to be covered by an opaque mask.

The other important component is the integrating sphere. It consists of a empty sphere whose interior is covered with a layer designed to have a high diffuse reflectance. When light from a source enters into the integrating sphere, it loses all memory of the point and direction of entrance at the entrance port of the sphere, as well as of its original polarization. At the exit port, the light intensity becomes highly uniform and diffuse.

In Figure 6.3, a diagram of the system is shown. For this system, the sampling disc was made by covering a 21 cm diameter *plexiglas* disc with a circular photolithographic mask containing 24 transparent sampling spots, as well as 720 radial marks on its periphery. These marks are optically sensed in order to read the photodetector signal into the computer every 0.5º. Another single mark on the periphery was used for knowing when the first reading of the outermost sampling spot takes place. Once the 720 values are read into the computer, they are assigned 30 per row in 24 rows. The diameter of the sampling spots is nearly 1mm, and the *abcd* window is 15º wide and is

radially placed between 7.4 and 9.5 cm. The integrating sphere as illustrated in Figure 6.4, was obtained by removing the active parts of an 8 cm diameter spherical lightbulb, and painting it both internally and externally with diffuse white-matte vinyl paint. The paint was removed in a 2 mm diameter spot, and the light escaping through is detected with a highly sensitive *New-Focus* model 2151 photodetector. This photodetector transforms the intensity of light into an electric signal which is processed by a conventional electronic circuit. Depending on the intensity of light will be the amplitude of the electrical signal obtained, which can provide us a grayscale in the final computer image.

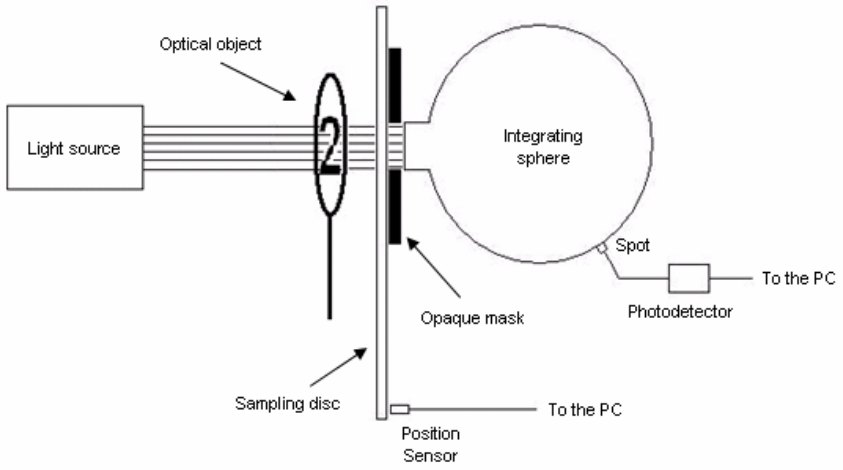

Figure 6.3. Schematic if the Nipkow disc system implemented by Soto et. al., [6.8]. Here the focusing element is represented as a lens.

Figure 6.4. Photograph of the integrating sphere constructed by Soto et. al., [6.8].

To scan the optical object it has to be placed between the rotating disc and a red beam laser which is expanded by a lens to illuminate the whole object, as illustrated in Figure 6.5.

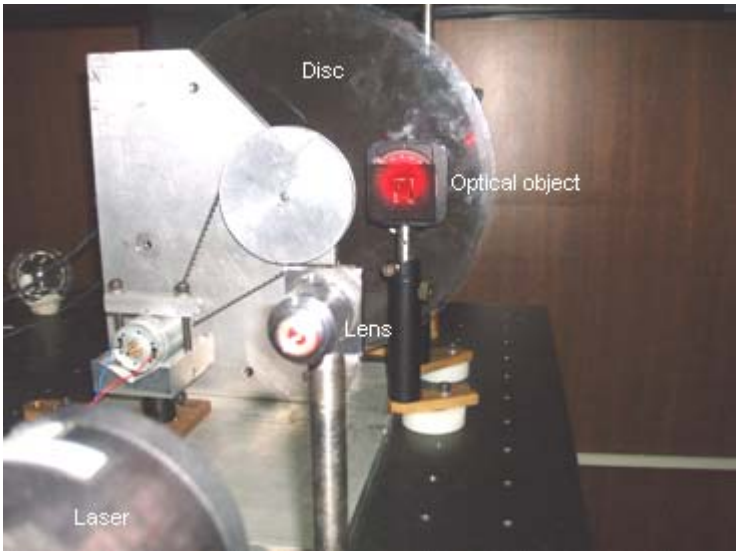

Figure 6.5. Photograph of the optical Nipkow disc system. The laser beam is expanded by a lens to illuminate perfectly the optical object.

6.3 Nipkow disc system implementation at millimeter frequencies

In order to prepare the approach at millimeter frequencies, some modifications have been made to the original design performed by Soto et. al, [6.8] in a collaborative effort with Dr. Soto and Andrés Mendoza. Essentially the modified design employs two discs of different diameter, one of 21 cm, from the original design, and another of 9 cm. The significance of using a combination of two discs is to enable us to implement this new design at millimeter frequencies, as will be explained below.

To use the Nipkow disc approach at millimeter-wave frequencies, it is important to determine the minimum diameter of the spiral holes of the disc. In order to find the minimum diameter of the spiral holes, we performed several tests using metal plates with a central hole diameter of different sizes (0.5, 1.0, …, 4.0 cm). The results are shown in Table 6.1. A metal plate is placed between a power meter (HP437B, from *Hewlett-Packard*) and a millimeter-wave source (HP8350B from *Hewlett-Packard*), as shown in Figure 6.6. The source power used was of 5 dBm (3.16 mW). The initial power of the system was of -76.12 dBm (2.44E-08 mW), and as can be noticed in Figure 6.7, a hole diameter of 1.5 cm is the minimum diameter which the object radiation can be detected by the MMW imaging system, i.e. spiral holes of at least 1.5 cm are needed to apply the Nipkow disc at millimeter frequencies. If a resolution by a large number of lines is required, say 24 lines (as the original design), the Nipkow disc for the MMW imaging system would have a spiral with 24 holes of 1.5 cm each and the size of the whole disc would be enormous, a few feet in diameter. Such an instrument would not be practical and it would be completely out of the question for equipment which has to be portable and light.

Table 6.1. Test results to obtain the minimum size in diameter of the Nipkow disc holes for the implementation at millimeter frequencies. The diameter of 1.5 cm is good enough to detect the radiation object with the MMW imaging system.

Diameter (cm)	Output Power (dBm / mW)	
0.5	-68.84	1.3062E-07
1.0	-50.56	8.7902E-06
1.5	**-40.75**	**8.4140E-05**
2.0	-38.28	1.4859E-04
2.5	-36.45	2.2646E-04
3.0	-32.2	6.0256E-04
3.5	-30.75	8.4140E-04
4.0	-30.2	9.5499E-04

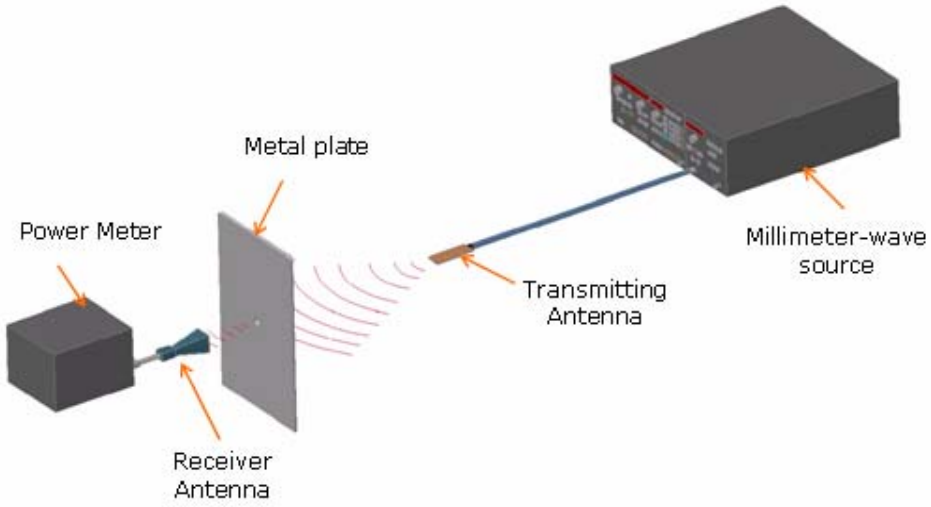

Figure 6.6. Diagram of experimental arrangement to find the minimum diameter of the spiral holes of the Nipkow disc.

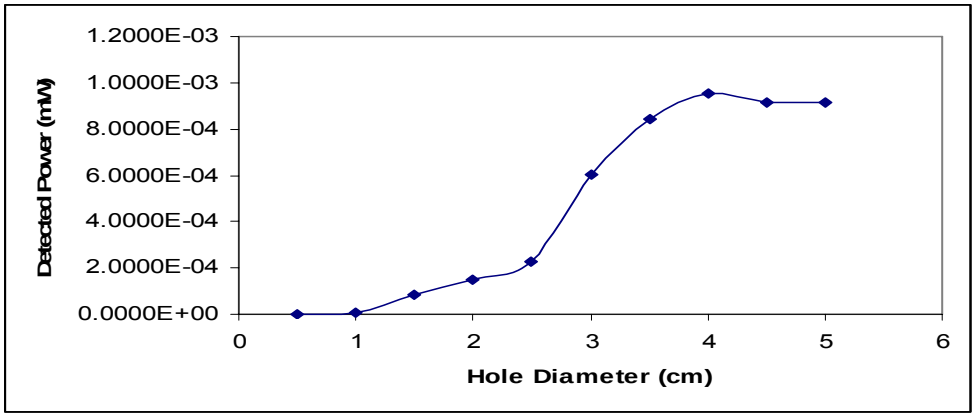

Figure 6.7. Graph of the hole diameter vs detected power. As can be noticed in the figure, the system begins to detect the object radiation with a hole diameter of 1.5 cm.

A second disc was implemented to separate the monitoring of the angular positions from the image sampling operation of the large disc. This disc is made of acetate paper and has 6 groups of 5 radial marks each, and a single mark on the periphery. The radial marks are separated 15º one of each other as shown in Figure 6.8. These groups are positioned so that only readings of

the holes 1, 4, 7, 10, 13 and 16 of the first disc are taken into account, giving a final resolution of $R = NxM = 6x5 = 30$ pixels. For that purpose, two horseshoe detectors are placed in the second disc (Figure 6.9), one of them to sense the beginning and end of the readings (through the mark on the periphery), and the other indicates when we have to take the reading from the photodetector and when not (using the radial marks). Once the 30 values are read into the computer, they are assigned 6 per row in 5 rows to display the final image. A photograph of the Nipkow disc system constructed is shown in Figure 6.10. The original disc is driven by a dc motor having a gear arrangement and a shaft. The disc is connected to the shaft and turns at motor speed (600 rpm). The second disc is provided with a central hole through which the shaft extends and is mounted behind the fist disc as shown in Figure 6.11. Thus, both discs rotate at the same speed and direction.

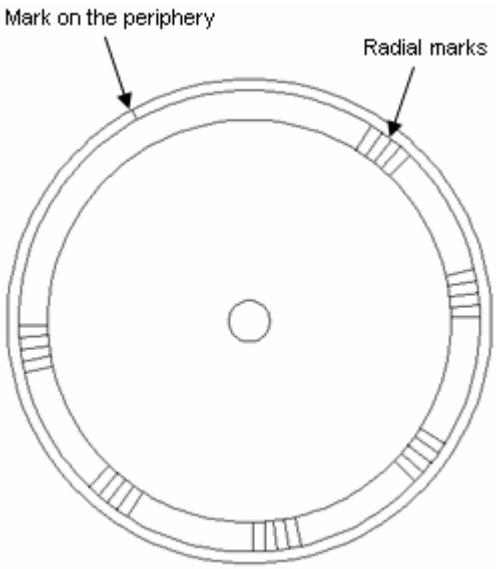

Figure 6.8. Mark configuration of the second disc implemented to reduce the resolution of the original Nipkow disc. The radial marks are separated 15º one of each other and the groups are positioned so that to only the readings of the holes 1, 4, 7, 10 and 16 are taken into account.

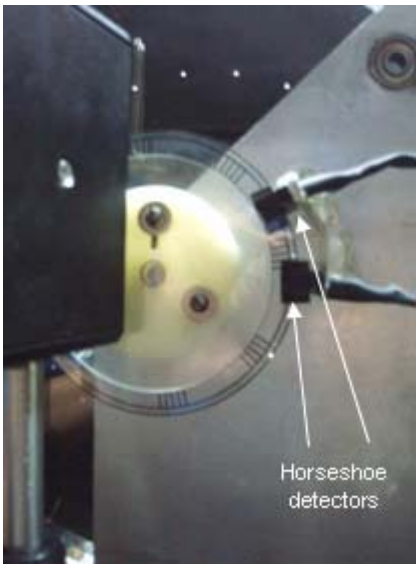

Figure 6.9. Photograph of the second disc constructed. Two horseshoe detectors are place in the disc, one of them to inform us the beginning and end of the readings, and the other to indicate us when we have to take the reading from the photodetector and when not.

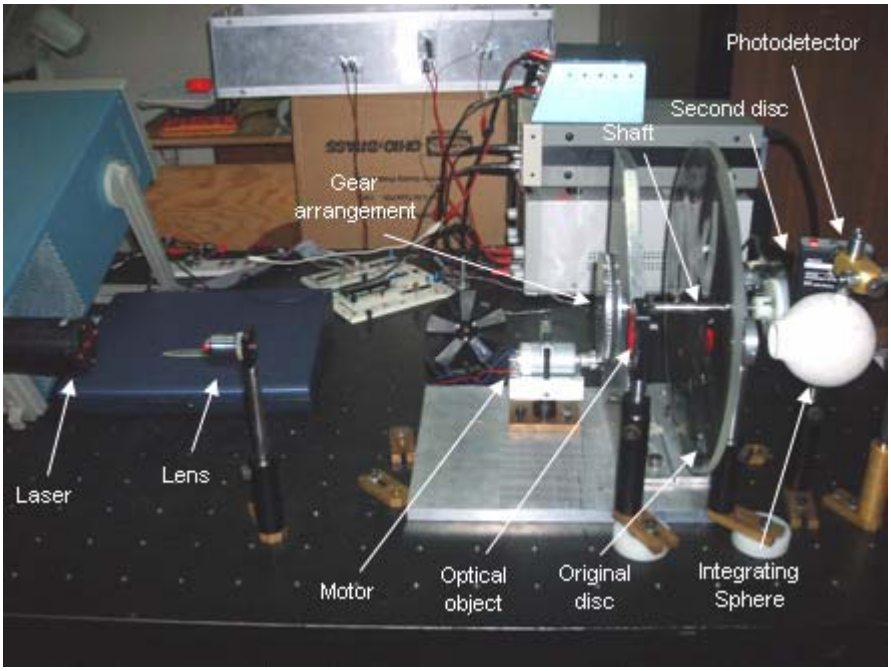

Figure 6.10. Lateral view of the constructed optical image acquisition system. The original Nipkow disc (big disc in the photo), is driven by the dc motor having a gear arrangement and a shaft.

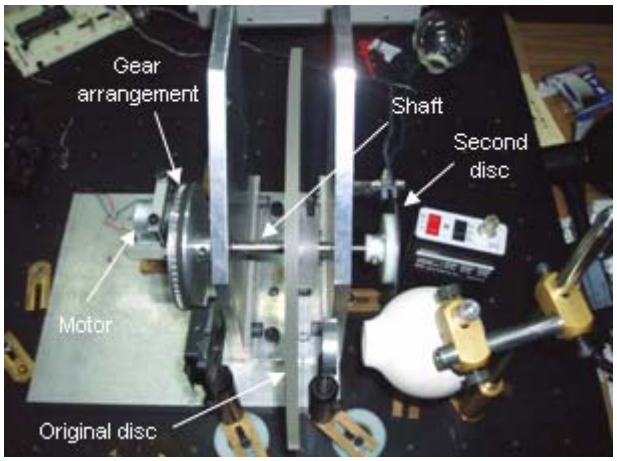

Figure 6.11. Top view of the constructed optical image acquisition system. The two discs are mounted on the same shaft allowing them to rotate at the same speed and direction.

As mentioned above, the Nipkow disc system has a resolution of R=30 pixels per image. These pixels are assigned in 6 columns per 5 rows to construct the final image. To display the scanned image on the computer a program in *Visual Basic* language was made. This program receives the information from the horseshoe detectors and photodetector through the parallel port of the computer by using a conventional electronic circuit. One of the horseshoe detectors informs to the program the beginning and end of the readings and the other indicates it when it has to take the reading from the photodetector and when not. We avoid with this any shape distortion in the image reconstructed. The electronic circuit also converts the data received from the photodetector in a binary format. Depending of the intensity of light, it will be assigned a particular binary number to provide us a grayscale in the reconstructed image.

Several tests by using different optical objects were made. The objects were mostly alphanumeric symbols such as C, E, 2, etc. Some image results are

shown in Figures 6.12 to 6.14. As we can observe in the pictures, we obtained good quality reconstruction of the scanned image at low resolution, which is needed for millimeter-wave frequencies approach.

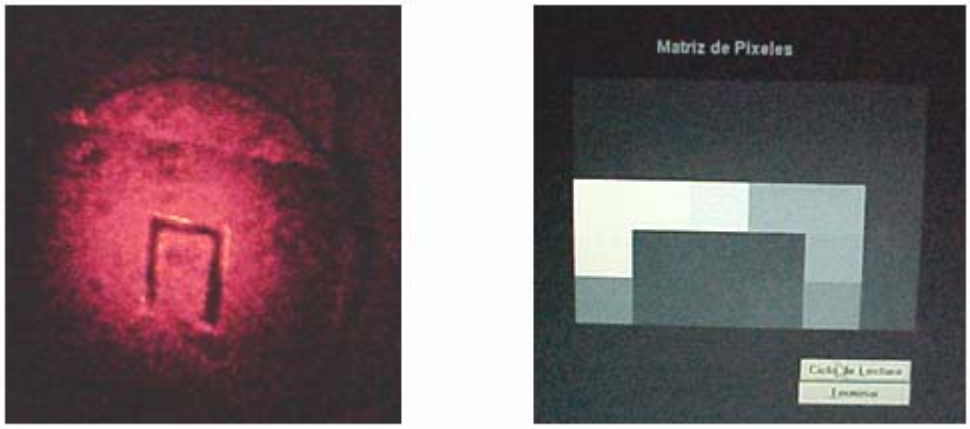

(a) (b)

Figure 6.12. (a) Photograph of a letter C illuminated by the laser beam, and (b) computer image result. The letter C is rotated 90º to the right.

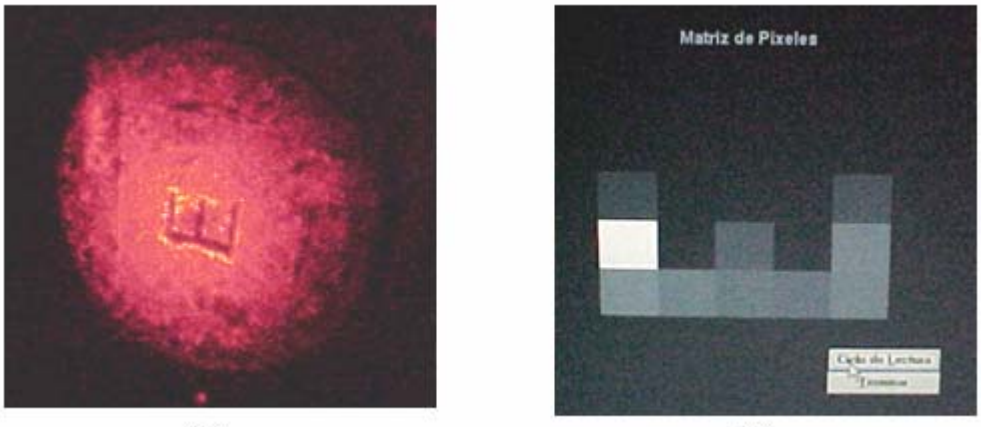

(a) (b)

Figure 6.13. (a) Photograph of a letter E illuminated by the laser beam, and (b) computer image result. The letter E is rotated 90º to the left.

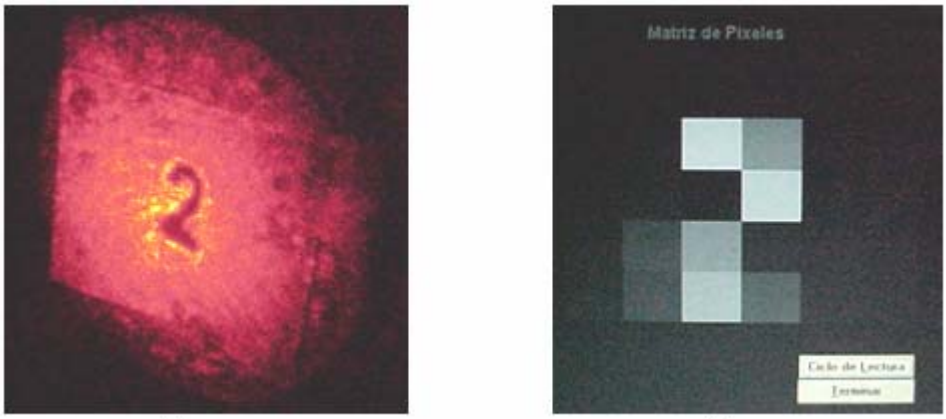

Figure 6.14. (a) Photograph of a number 2 illuminated by the laser beam, and (b) computer image result.

Thus, we can conclude that a Nipkow disc method for image reconstruction at video rates is a viable solution for the MMW imaging system.

References

[6.1] R. M. Smith, B. M. Sundstrom, B. W. Belcher, and D. Ewen, "ROSCAM: A 95-GHz radiometric one-second camera," Passive millimeter-wave imaging technology II, R. M. Smith (editor), Proc SPIE, 1998, vol. 3378, p.p. 2-13.

[6.2] A. Luukanen and V. P. Viitanen, "Terahertz imaging system based on antenna-coupled microbolometers," Passive millimeter-wave imaging technology II, R. M. Smith (editor), Proc SPIE, 1998, vol. 3378, p.p. 34-44.

[6.3] R. N. Anderton, R. Appleby, J. R. Borril, D. G. Gleed, S. Price, N. A. Salmon, G. N. Sinclair, P. Papakosta, and A. H. Lettington, "Real time passive mm-wave imaging,"

Passive millimeter-wave imaging technology II, R. M. Smith (editor), Proc SPIE, 1998, vol. 3378, p.p. 77-83.

[6.4] B. Blume, J. Wood, and F. Downs, “Naval special warfare MMHW data collection results,” Passive millimeter-wave imaging technology II, R. M. Smith (editor), Proc SPIE, 1998, vol. 3378, p.p. 86-94.

[6.5] D. F. McLean, "Restoring Baird’s image," *IEE Review*, Vol. 46, no. 5, Sept. 2000, pp. 9-14.

[6.6] www.inventors.about.com: http://inventors.about.com/od/germaninventors/a/Nipkow.htm

[6.7] www.wikipedia.org: http://en.wikipedia.org/wiki/Nipkow_disk

[6.8] J. Soto, and J. A. Dávila, “A Technique for the Fast Raster-Scanned Motion of a Small Window for Millimeter- Wave Image Acquisition,” in *Microwave and Optical Technology Letters*, vol 32, no. 6, pp. 440-442, March 2002.

[6.9] J. A. Lovberg, C. Martin, and V. Kolinko, “Video-Rate Passive Millimeter-Wave Imaging Using Phased Arrays,” *IEEE/MTT-S International Microwave Symposium, 2007*, pp. 1689-1692, June 2007.

[6.10] L. Schulwitz, and A. Mortazawi, ”A Compact Dual-Polarized Multibeam Phased-Array Architecture for Milimeter-Wave Radar,” *IEEE Transactions on Microwave Theory and Techniques*, vol. 53, no. 11, pp. 3588-3594. Nov. 2005.

[6.11] H. Park, M. K. Singh, S. Kim, H. Lee, and Y. Kim, “Blind Image Restoration for MMW Radiometer Based on Wavelet Techniques,” *IEEE International Geoscience and Remote Sensing Symposium, 2005*, vol. 6, pp. 4279-4282, July 2005.

Chapter VII

System Results

In this chapter the experimental results of the remote sensing system shall be treated. The performance and experimental results obtained from the MWW detector system in active mode will be exhibited.

7.1 Performance of the MMW detector system

As mentioned in Chapter IV, three different kinds of antennas (Parabolic, Vivaldi and Horn) were used to obtain the best performance of the PMMW detector system. This performance was made in passive mode (see Section 4.5.1).

a) Using a Parabolic Horn Antenna

For initial experiments we used a parabolic horn antenna available in the institute's microwave laboratory. Several objects of different materials such as plastic, ceramic, and aluminum were measured, as shown in Table 7.1. The experimental setup is shown in Figure 4.1 of Chapter 4.

With this antenna very small voltage differences were obtained with respect to the initial voltage (1.61 V). The maximum voltage difference obtained was around 4 mV, produced by the ceramic plate. The voltage difference is not

high enough for object detection. Therefore, it can be concluded that the use of this antenna did not provide us very useful results. One of the reasons of this could be that we did not know the specifications of the antenna such as the bandwidth (as mentioned in Section 4.5), which could be lower or higher than the system's bandwidth (18-26 GHz).

Table 7.1. Obtained results from objects of different materials by using the parabolic horn antenna. The best difference with respect to the initial voltage (1.61 V) was obtained with a ceramic plate which produced a difference around 4 mV.

Object	Output Voltage (V)	Difference (mV)
Aluminum plate	1.64	3
Plastic Plate	1.59	2
Ceramic plate	1.65	4

b) Using a Antipodal Vivaldi Antenna

The second antenna employed in the MWW detector system was the antipodal Vivaldi antenna. In this case several objects of different materials were also detected. The aluminum plate showed a voltage difference of approximately 30 mV with the initial voltage (75 mV), while the cardboard plate did not provide any change, as shown in Table 7.2. It is important to note that the initial voltage is not the same as in the previous Section since the antennas have different gains and the integration time is also different, as discussed in Chapter 4. With these results a object detection can be done with appreciable quality.

Table 7.2. Measured results from objects of different materials by using the antipodal Vivaldi antenna. The best difference with respect to the initial voltage (75 mV) was obtained with an aluminum plate providing us a difference of around 29 mV.

Object	Output Voltage (mV)	Difference (mV)
Aluminum Plate	56	29
Plastic Plate	76	1
Ceramic Plate	79	4
Cardboard Plate	75	0

c) Using a Rectangular Horn Antenna

The third antenna used in the system was a rectangular horn antenna. Here we detected once again several objects of different materials. As we can see in Table 7.3, the aluminum plate provided a difference of 45 mV with the initial voltage (85 mV), while the cardboard plate did not show again any change. In this case, the voltage differences produced by the object radiations were higher than the other two antennas, allowing detect in a better way the object radiation. It can be concluded that with this last antenna we found the best performance of our system, so the final design of the MWW imaging system is based on this antenna.

Table 7.3. Obtained results of different materials by using the rectangular horn antenna. The best voltage difference with respect to the initial voltage (85 mV) was obtained with an aluminum plate providing a difference of approximately 45 mV. This performance provided us the maximum detection of the object radiation.

Object	Output Voltage (mV)	Difference (mV)
Aluminum Plate	130	45
Plastic Plate	83	2
Ceramic Plate	70	11
Cardboard Plate	81	0

In the three antenna cases, changes in the output voltage values can be observed by varying the viewing angle of the object and its focal length. These changes in the output voltages are because of the inherent noise of the system. The main problems causing this inherent noise were leakage through the edges of all metal boxes and electromagnetic mismatched signals looping back the coaxial cables, as illustrated in Figure 7.1. The first problem was treated by tightening with precision each connector through a specialized torque spanner. By using this tool instead of hand tightening the cables most of these mismatched signals can be eliminated.

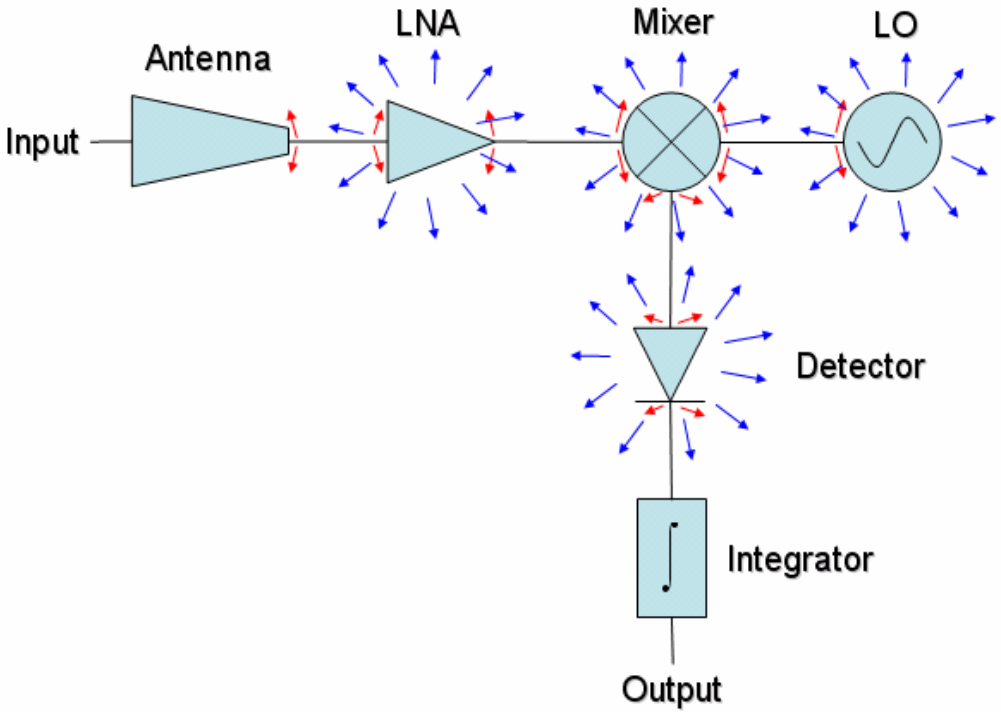

Figure 7.1. Illustration of the inherent noise problem caused by leakage (red arrows) and electromagnetic interference (blue arrows).

Then, to address the problem of electromagnetic radiation, the radiated power from each component of the system was measured with the power meter

(HP437B), as shown in Figure 7.2 and found that this noise is mainly due to the LO, which radiates its ac output signal to the whole system.

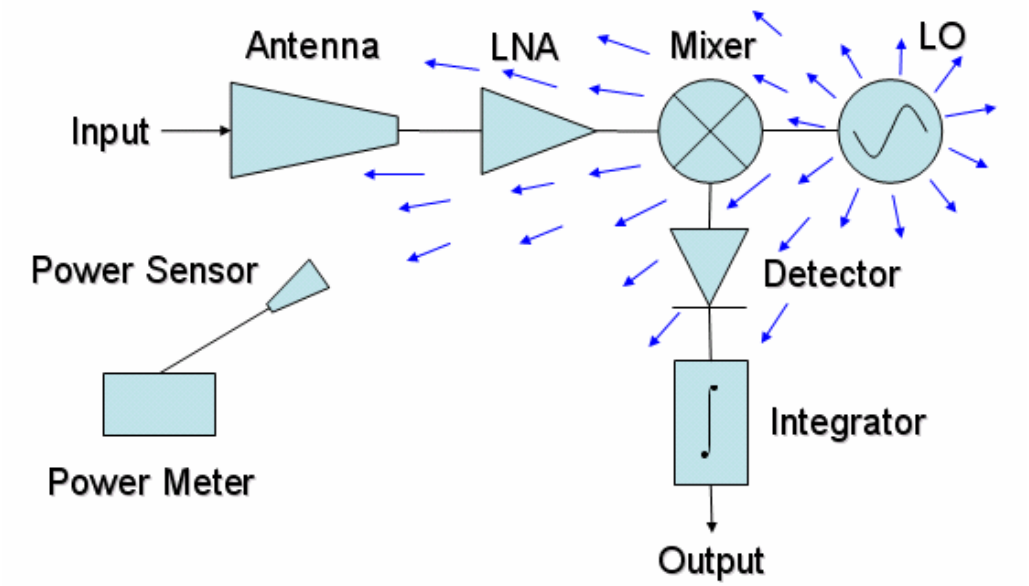

Figure 7.2. Measurement of the radiated power of each component to address the problem of electromagnetic radiation. It was found that the LO is the principal producer of the inherent noise of the system.

To solve the LO radiation problem we used a 320-3-C-RAM-AR/HP millimeter-wave absorber (see Appendix A), from *Cuming Microwave Corporation* to isolate the LO and all the components inside the metal box (see Figure 7.3) This absorber has a thickness of 0.375 in, performance of -20 dB at the frequency of 10 GHz and up. To verify if the system had become isolated from the LO radiation, several measurements were performed after and before isolating the system components. These measurements consisted of measuring the radiation produced by the aluminum plate at different angles, both the left and right taking the center as 0°, as displayed in Figure 7.4. The results are shown in Table 7.4. As we can see in Figure 7.5, the changes in the output voltage of the MMW imaging system with its

components covered with the absorber were almost null with respect to the angle, which showed that the LO was the primarily responsible of the inherent noise from the system, significantly reducing the problem of reflection caused by the angle.

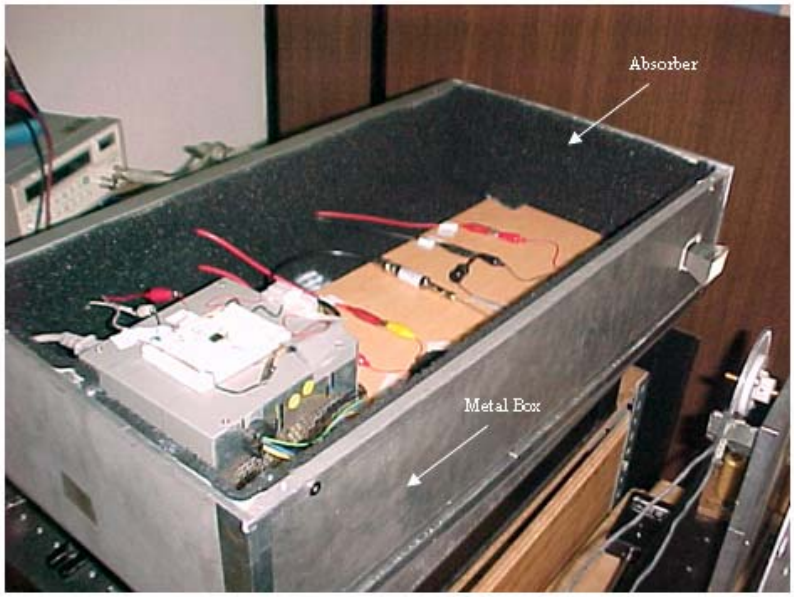

Figure 7.3. Photograph of the system covered by absorber material.

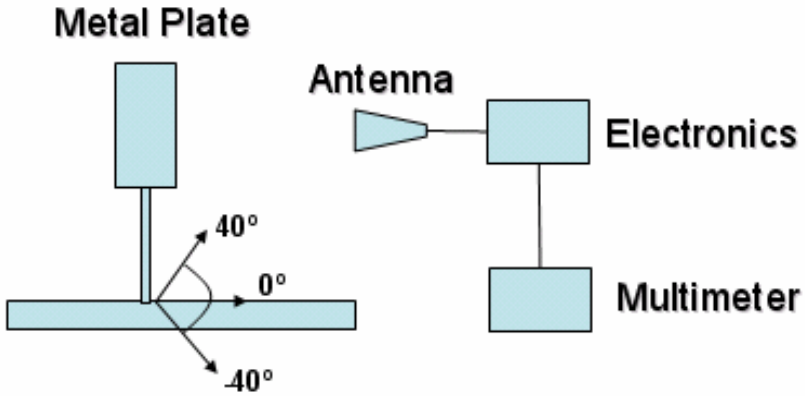

Figure 7.4. Setup to verify if the system had become isolated from the LO radiation.

Table 7.4. Measurements of the aluminum plate radiation at different viewing angles with the LO and all the components isolated with a millimeter-wave absorber.

Angle (°)	Without absorber (mV)	With absorber (mV)
0	77	80
10	65	82
20	86	82
30	88	81
40	78	82
-10	86	82
-20	91	81
-30	87	82
-40	80	82

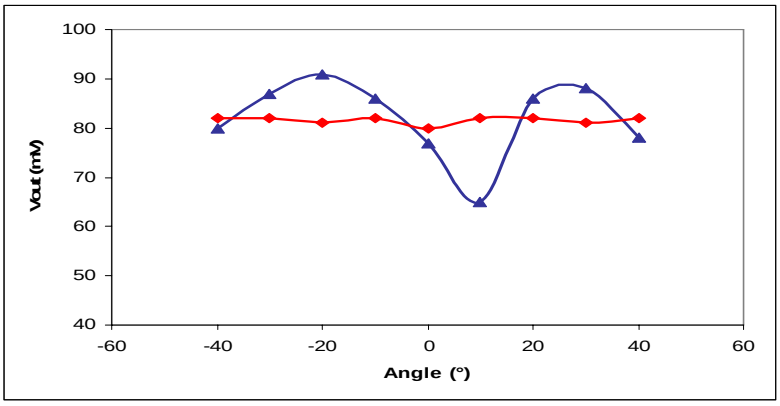

Figure 7.5. Graph of the obtained measurements to solve the LO radiation. Without absorber in blue, and with absorber in red.

7.2 System results in active approach

As mentioned in Section 4.5.2, we also performed tests with the MMW imaging system in active mode, that is, we used a millimeter-wave source (HP8350B) to irradiate the object under observation. This source produces much higher powers than those thermically emitted by the objects, which means we can get greater contrast between the object and its surroundings.

The diagram of the system in active mode is shown in Figure 7.6. We used the Vivaldi antenna as the transmitting antenna of the millimeter-wave source. To reduce side lobes radiation from the transmit antenna it was covered with aluminum foil.

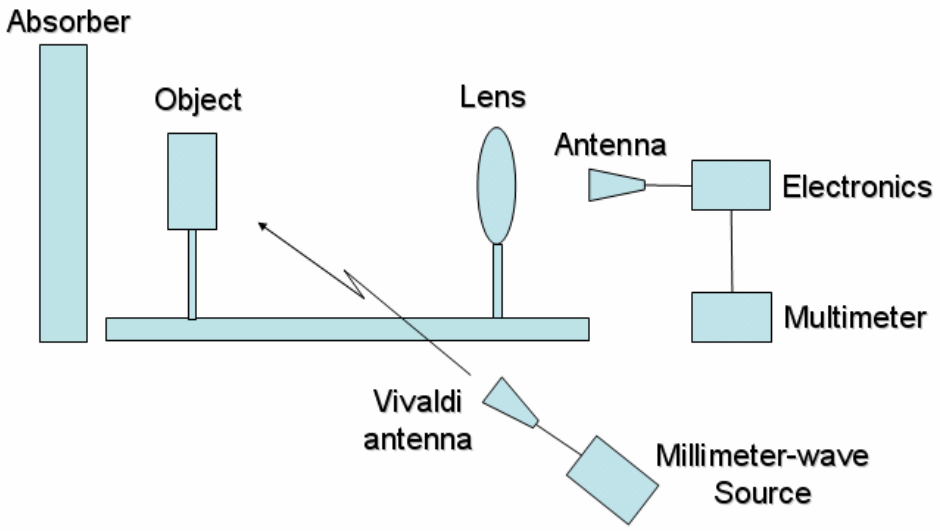

Figure 7.6. Diagram of the MMW imaging system in active mode.

First, several objects such as aluminum, ceramic, and plastic plate were measured in the same way as in passive mode. The data obtained is displayed in Table 7.5. These values were obtained by varying the source power from -2 to 18 dBm with increments of 0.5 dBm. The initial voltage of the system was of 72 mV approximately, and as we can note, the biggest change was again produced by the metal plate, while the lowest was produced by the plastic plate, as occurred in passive mode. Here we obtained a greater change in the output voltage compared to the passive mode since, as mentioned above, the source produces a greater contrast between the object and the area scene. As can be noted in Table 7.5, the minimum power source that provided us a huge voltage difference between the different objects was of 13.5 dBm, where the metal, ceramic and plastic plate produced a voltage

difference of 278, 85 and 51 mV, respectively. These findings allow the detection of the material which the object is made of with a very high percentage of veracity. Thus, it can be concluded that the active approach of the MMW imaging system is the best performance for object material detection.

Table 7.5. Object radiation detection in active mode.

Source Power (dBm)	Aluminum Plate (mV)	Ceramic Plate (mV)	Plastic Plate (mV)
-2.0	-46	-71	-73
-1.5	-44	-70	-73
-1.0	-40	-70	-73
-0.5	-36	-69	-72
0.0	-33	-69	-72
0.5	-29	-67	-71
1.0	-25	-66	-71
1.5	-19	-65	-70
2.0	-13	-63	-70
2.5	-5	-62	-70
3.0	2	-61	-69
3.5	7	-58	-69
4.0	14	-57	-68
4.5	23	-56	-66
5.0	31	-55	-66
5.5	39	-53	-63
6.0	48	-51	-63
6.5	56	-50	-62
7.0	63	-47	-61
7.5	71	-45	-55
8.0	79	-43	-54
8.5	86	-41	-51
9.0	95	-37	-51
9.5	106	-33	-50
10.0	118	-27	-48
10.5	127	-25	-45
11.0	139	-20	-45
11.5	152	-18	-38
12.0	165	-15	-28
12.5	176	-9	-26
13.0	195	-3	-24
13.5	**206**	**13**	**-21**
14.0	222	17	-17
14.5	239	20	-14

15.0	257	26	3
15.5	272	31	13
16.0	286	39	17
16.5	302	44	22
17.0	313	54	26
17.5	323	65	35
18.0	329	73	43

Then, the voltage/power relation of the MMW imaging system was obtained by using the power meter (HP437B). The setup used for this test is shown in Figure 7.7. The millimeter-wave generator was used to radiate the MMW imaging system in direct form. The transmitting antenna was placed 1 m away from the receiver antenna, and the source power was varied in a range of -2 to 23 dBm with steps of 0.5 dBm. The data obtained is shown in Table 7.6. As we can observe in Figure 7.8, the output voltage of the system increases as the source power is also increased until it reaches a maximum value where its behavior is almost constant. This behavior is expected due to the nonlinearity of the LNA, that is, as the power of the input signal is increased, it generates greater harmonics hence reducing the power of the signal of interest. If the power keeps on increasing the amplifier reaches it saturation stage [7.1]. For our setup, the amplifier has a quasi linear behaviour up to about 14dBm of the source power.

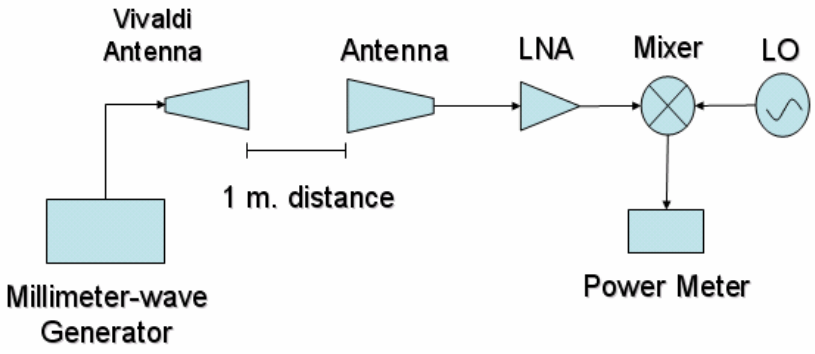

Figure 7.7. Schematic for measuring the voltage/power relation of the MMW imaging system.

Table 7.6. Voltage/power relation of the MMW imaging system.

Source Power (dBm)	Output Voltage (mV)
-2.0	58
-1.5	66
-1.0	75
-0.5	83
0.0	92
0.5	102
1.0	112
1.5	122
2.0	133
2.5	145
3.0	157
3.5	173
4.0	188
4.5	202
5.0	220
5.5	236
6.0	254
6.5	270
7.0	287
7.5	301
8.0	315
8.5	328
9.0	341
9.5	354
10.0	366
10.5	379

Source Power (dBm)	Output Voltage (mV)
11.0	390
11.5	402
12.0	412
12.5	422
13.0	430
13.5	436
14.0	442
14.5	447
15.0	450
15.5	454
16.0	455
16.5	455
17.0	455
17.5	455
18.0	456
18.5	456
19.0	456
19.5	456
20.0	457
20.5	457
21.0	457
21.5	458
22.0	458
22.5	458
23.0	458

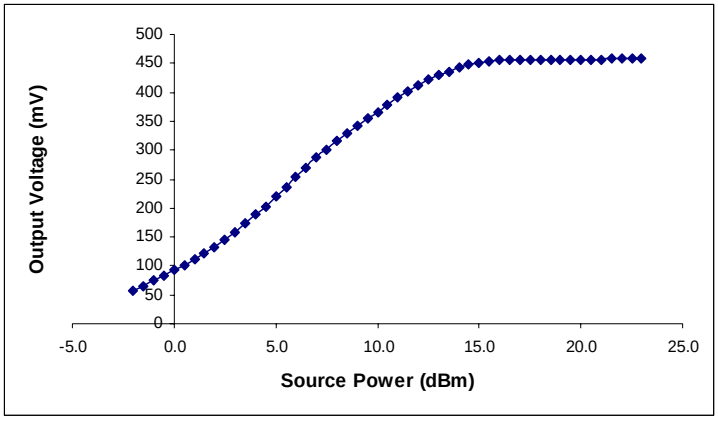

Figure 7.8. Voltage/power relation of the MMW imaging system.

Finally, a third test was performed for measuring the power at each stage of the system (antenna, antenna-LNA, antenna-LNA-Mixer-LO) by using the power meter. The power of the millimeter-wave source was varied in a range of -2 to 11.5 dBm with increments of 0.5 dBm. The schematic setups of every stage are shown in Figure 7.9. The data obtained is shown in Table 7.7. As we can observe in Figure 7.10a, as the source power is increased, the power measured by the system increases, presenting a linear behavior, but the readings taken after the LNA (settings antenna-LNA, and antenna-LNA-Mixer-LO) presented the nonlinear behavior discussed in the preceding paragraph (Figures 7.10b and 7.10c).

Table 7.7. Measurements of the power behavior at every stage of the MMW imaging system.

Source Power (dBm)	**Configuration (a) (dBm)**	**Configuration (b) (dBm)**	**Configuration (c) (dBm)**
-2.0	-49.61	2.94	-4.74
-1.5	-49.30	2.97	-4.42
-1.0	-48.80	3.31	-4.27
-0.5	-48.69	3.40	-4.11
0.0	-48.10	3.74	-3.95
0.5	-47.71	3.96	-3.64
1.0	-47.23	4.11	-3.48
1.5	-46.63	4.47	-3.2
2.0	-46.32	4.82	-2.91
2.5	-45.64	5.10	-2.64
3.0	-45.31	5.37	-2.21
3.5	-44.76	5.62	-2.1
4.0	-44.33	5.87	-1.87
4.5	-43.82	6.03	-1.69
5.0	-43.31	6.19	-1.47
5.5	-42.92	6.42	-1.37
6.0	-42.25	6.47	-1.21
6.5	-41.79	6.72	-0.98
7.0	-41.31	6.82	-0.87
7.5	-41.02	6.95	-0.79
8.0	-40.43	7.03	-0.74
8.5	-39.95	7.17	-0.62
9.0	-39.52	7.23	-0.55
9.5	-38.92	7.26	-0.49
10.0	-38.37	7.33	-0.41
10.5	-38.14	7.36	-0.39
11.0	-37.63	7.39	-0.34
11.5	-37.42	7.42	-0.31

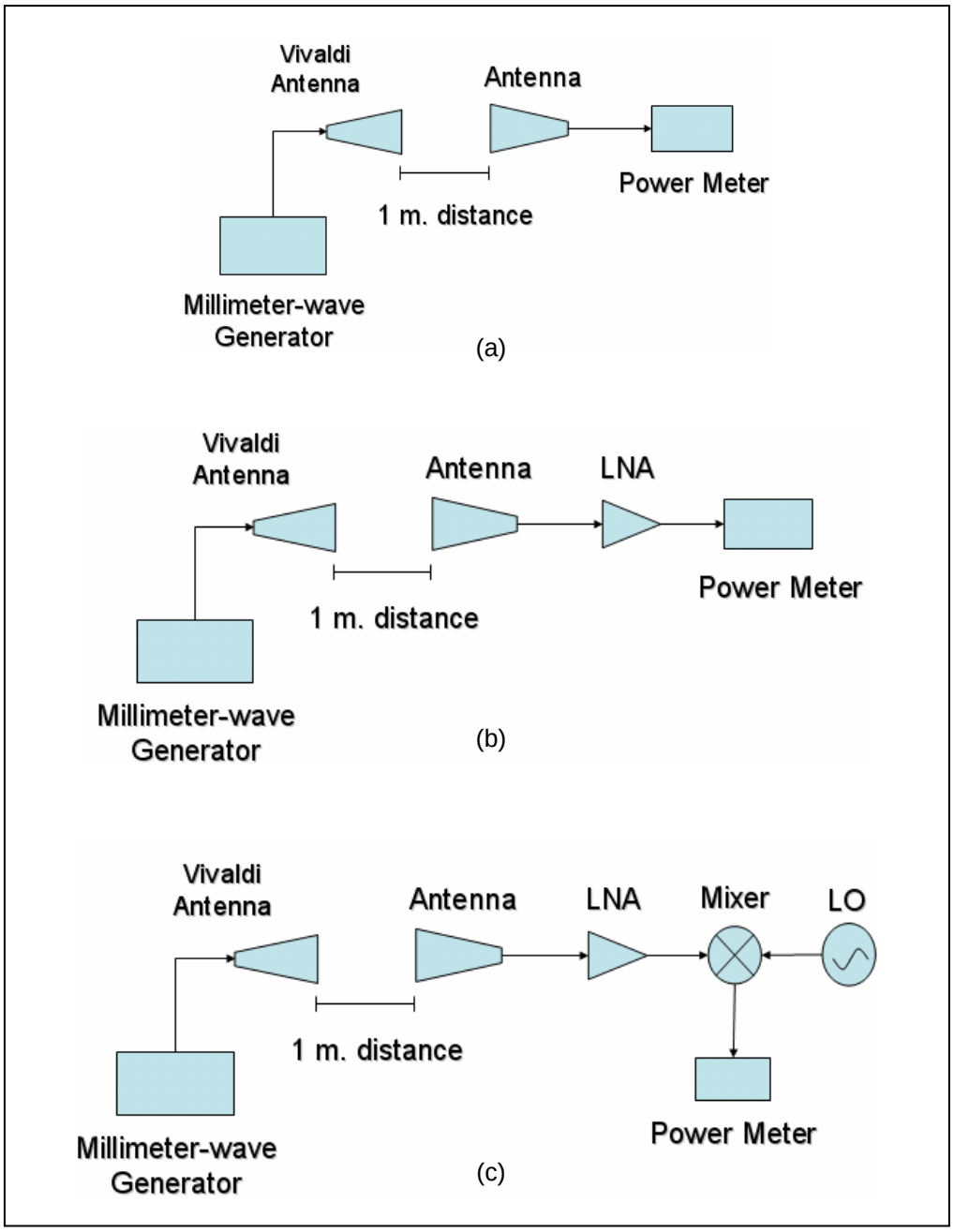

Figure 7.9. Settings for measuring the power behavior at the different stages of the MMW imaging system. (a) Antenna setting, (b) antenna-LNA setting, and (c) antenna-LNA-mixer setting.

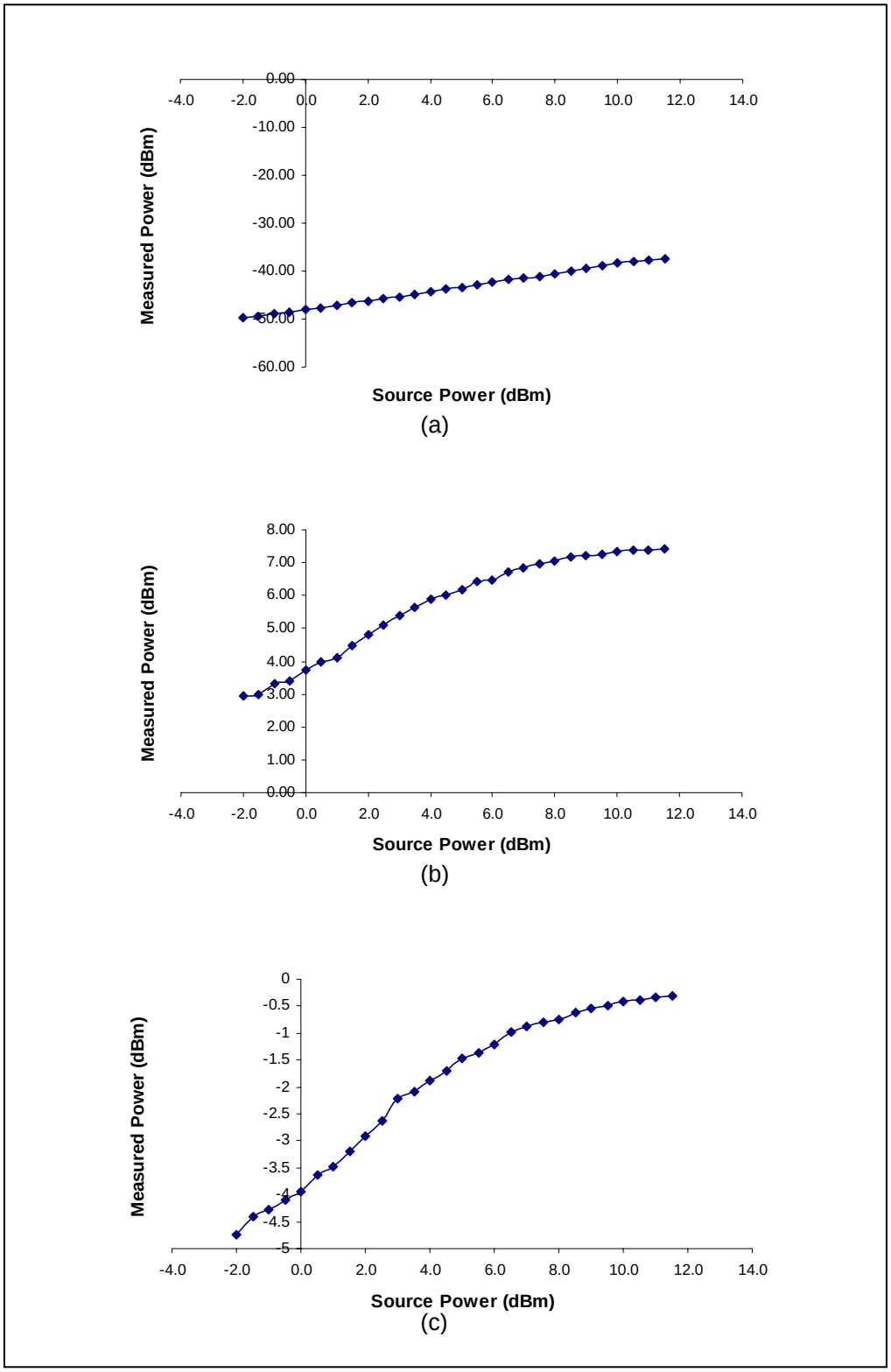

Figure 7.10. Power behavior at the different stages of the MMW imaging system. (a) Antenna setting, (b) antenna-LNA setting, and (c) antenna-LNA-mixer setting.

References

[7.1] W. H. Hayt, J. E. Kemmerly, and S. M. Durbin, “Engineering Circuit Analysis,” 6th. ed., Ed. Mc-Graw-Hill Companies, Inc, 2002.

Chapter VIII

Conclusions and Future work

8.1 Conclusions

MMW imaging is a method of forming images through the detection of millimeter-wave radiation from a scene. This power is a combination of what the scene object is directly emitting and what it is reflecting from its environment. As we have seen in Section 3.2.2, there are two different approaches which can be distinguished for the development of MMW imaging systems: Active and Passive imaging. Active millimeter-wave imaging uses a source to illuminate the scene where the object is placed, and as explained in Section 3.2.2.2, this source produces much higher power than those thermically emitted from objects within the scene, producing higher contrast. Passive means that the spectral distribution of natural radiation which is emitted or reflected from a body at room temperatures is properly captured and displayed (radiometry). In this thesis work a millimeter-wave detector system in active mode has been implemented. Different materials such as plastic, ceramic, cardboard and aluminum have been successfully detected.

To obtain the image reconstruction of the scanned object with the MMW imaging system a nipkow disc has been implemented in a collaborative effort with Dr. Soto and Andrés Mendoza. The demonstration of the nipkow disc principle is made in the optical region as preliminary step for the

implementation of the nipkow disc at millimeter-wave frequencies, as discussed in Chapter 6.

The images obtained using the nipkow disc at optical frequencies have been successfully reconstructed. Thus, the nipkow disc is a viable solution for the MMW imaging system. Moreover the nipkow disc also presents many advantages such as low cost, simple implementation and fast sampling in comparison with other image reconstruction methods, as shown in Chapter 6.

As explained in Chapter 5, the SIW technology has been developed as a solution for the two fundamental problems that the classical waveguide technology presents at millimeter-wave frequencies, namely, radiation loss due to discontinuity, difficult modal transition to planar circuits and high manufacturing costs. The SIW concept consists on synthesizing non-planar structures on a dielectric substrate in planar form. The advantage of the SIW technology is that these planar circuits could easily be integrated with MMICs. Moreover SIW has the advantages of cost reduction and miniaturization of the system. The design of the SIW exponential flare horn antenna allows a very compact design of a completely integrated planar platform with very broad bandwidth. The final simulated design of the SIW exponential flare horn antenna obtained a BW (below -10 dB) of 22GHz (18-40 GHz), wider than any other reported SIW antenna. The arc lens placed in the substrate improves the directivity of the SIW antenna as shown in Chapter 5.

As a final word, we can say that the exploitation of the millimeter wave regime is the natural next step in expanding our ability to see more of the world through artificial means. The MMW imaging system ideas proposed in this thesis work offer portable, light and inexpensive solutions for modern remote sensing systems.

8.2 Future Work

As future work the nipkow disc at millimeter-wave frequencies with the hole dimensions obtained in Section 6.3 will be implemented on a metal disc for millimeter wave testing. Other aspect to be contemplated is the total isolation of the system with absorber material to reduce RF interference. Also, the SIW antenna should be implemented and tested, and a final MMW imaging Front End system should be realized on a single substrate to have a fully integrated circuit.

Finally, the usage of higher frequencies could enhance the pixel resolution for short distance applications.

Appendix A

Data Sheets of the Materials and Components

A.1 Millimeter-wave absorber AN-79

EMERSON & CUMING MICROWAVE PRODUCTS

RoHS Compliant

ECCOSORB® AN

Flexible Foam Sheet Broadband Microwave Absorbers

Material Characteristics

- Lightweight, flexible, broadband, open-cell, polyurethane foam absorber
- Carbon loaded, laminated polyurethane sheets
- Frequency range from 600 MHz -40 GHz
- Designed to reflect less than -20 dB of normal incident energy above specified frequencies and relative to a metal plate
- Does not support fungal growth per MIL-STD-810E
- Can be readily cut on a band saw, with scissors, die, or a sharp knife

Applications

- ECCOSORB® AN is commonly used for the lining of small test chambers to reduce reflections
- ECCOSORB® AN has been used in reducing crosstalk between adjacent antennas, shrouding antennas to improve the antenna patterns and undesired backlobes, as well as selective shadowing of parts of a target for RCS measurements
- Shadowing of posts and supports in anechoic chambers, and as absorbing blankets for testing radar systems without harm to personnel
- For isolation of components or antennas by means of insertion loss, it can be used without a metal backing

Environmental Properties

- ECCOSORB® AN is *not* waterproof and will not operate correctly when wet. Since there is no washout, ECCOSORB® AN will function as expected after being allowed to dry
- A special CERSEAL coating to prevent moisture uptake in high humidity to moderately wet environments is available on special request
- For waterproof applications, see ECCOSORB® ANW or ECCOSORB® AN can be coated with CERSEAL

Availability

- Standard sheets are 24" x 24" (61 cm x 61 cm)
- Thickness depends upon the lowest desired frequency of operation required
- ECCOSORB® AN is available in other sizes and customer specified configurations, incorporating miter cuts or attachment to metal parts
- Can be manufactured, on special order, on a mandrel, to take a contoured shape.

Instructions for Use

- To obtain low reflectivity, the absorbers must be mounted on a metal surface. If a metal surface is not available, ECCOSORB® AN can be supplied metal backed with aluminum foil (ML)
- Layering of multiple pieces or slicing off part of the thickness will degrade the overall performance
- Reflectivity performance also degrades for off-normal bistatic incidence and at different rates for different polarizations
- ECCOSORB® AN can be securely bonded to itself or to other materials such as metal, wood, and common plastic composites. The recommended adhesive is ECCOSTOCK® 13-111-NF.

Typical Properties

Front Surface Color (facing oncoming EMI)	White
Max. Service Temperature, °F (°C)	248 (120)
Power Handling, W/cm^2	0.15
Thermal Conductivity, cal-cm/sec- cm^2-°C	6.8 x 10^{-4}
Fire Retardancy	UL 94 HBF

	Reflectivity range (>20 dB)	Thickness Inch (cm)	Weight lb/piece (kg/piece)	Density oz/in^3 (g/cm^3)
AN-72	>20 GHz	0.24 (0.6)	0.6 (0.25)	0.06 (0.11)
AN-73	>7.5 GHz	0.39 (1.0)	1.1 (0.50)	0.08 (0.13)
AN-74	>3.5 GHz	0.75 (1.9)	1.5 (0.70)	0.06 (0.10)
AN-75	>2.4 GHz	1.14 (2.9)	1.8 (0.80)	0.04 (0.07)
AN-77	>1.2 GHz	2.24 (5.7)	3.3 (1.50)	0.04 (0.07)
AN-79	>600 MHz	4.49 (11.4)	6.5 (2.95)	0.04 (0.07)

A.2 Millimeter-wave absorber 320-3-C-RAM-AR/HP

CUMING MICROWAVE

C-RAM AR

RoHS Compliant

TECHNICAL BULLETIN 320-3

RETCULATED FOAM BROADBAND RADAR ABSORBER

C-RAM AR is a line of reticulated foam Radar Absorbing sheet materials, comprised of urethane foam and a gradient lossy coating C-RAM AR absorbs microwave energy across a wide range of frequencies. Typically the thicker the material the lower in frequency C-RAM AR will attenuate. C-RAM AR has proven to be ideal for lining shrouds of communications antennas for the suppression of sidelobes. It can also be used to cover fences to separate adjacent antennas, and shield or isolate equipment. The open-cell structure permits airflow freely through the absorber, also when used outdoors rain will freely drain from the product. Cuming Microwave Corporation offers two types of C-RAM AR, our standard performance AR and high performance AR.

C-RAM AR SELECTION

Typically the standard performance AR is suitable for most antenna shroud applications, high performance AR is suited for applications where maximum attenuation is desired, such as RCS reduction, chamber fences, Radomes, electronic enclosures and foam through applications. If standard performance AR is suitable it will cost less than high performance AR. Reticulated foam absorbers in general are the lowest cost absorbers, including high performance AR. AR can also be supplied as an insertion loss material. On specialty applications AR has been purchased up to 3.0" thick. Consult the factory if a required thickness is not listed.

TYPICAL PROPERTIES

Porosity, pores per inch:	4-20
Tensile strength, psi:	8-12
Tear strength, lb/inch width:	2.2
Density, lb/ft^3:	3.0
Ultimate elongation (%) max:	275
Environmental Properties	
Operating temp., max:	250^{0}F
Ozone adverse affects:	No
Fungus Resistance, Evidence of fungus growth:	No

TYPICAL REFLECTIVITY

(dB down from reference)

Standard Performance (SP) Grade:

Thk.	Performance	Freq. Range
0.375in.	-12 dB	10 GHz & up
0.50in	-12 dB	8 GHz & Up
0.75in.	-12 dB	6 GHz & Up
1.0in.	-12 dB	6 GHz & Up
1.25in.	-12 dB	5 GHz & Up

High Performance (HP) Grade:

Thk.	Performance	Freq. Range
0.375in.	-20 dB	10 GHz & Up
0.50in.	-20 dB	8 GHz & Up
0.75in.	-20 dB	6 GHz & Up
1.00in.	-20 dB	6 GHz & Up
1.25in.	-20 dB	5 GHz & Up

225 Bodwell Street, Avon, MA 02322 USA • Tel 508.580.2660 • 800.432.6464 • Fax 508.584.2309
mwsales@cumingcorp.com • www.cumingmw.com

A.3 Low Noise Amplifier QWL-15262855-JO

QuinStar Tecnology, Inc.

Model Number	Frequency Range (GHz)	Noise Figure (dB Max)	Gain (dB)	Gain Flatness (±dB)	Current (mA) max., at 12V	Outline
QLW-15262855-XX	15-26	2.8	55	3.25	300	J

Outline Drawings

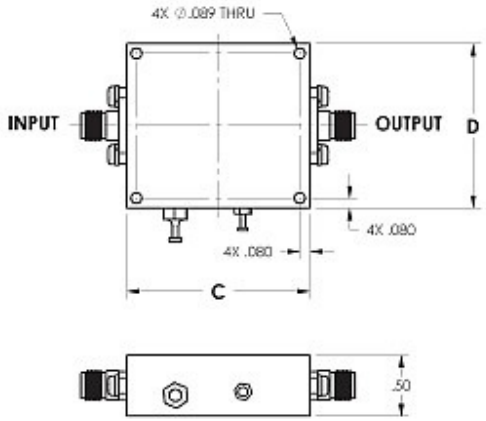

OUTLINE	C	D
J	1.50	1.35
A	2.50	1.75
B	2.50	3.00

Outline A, B, J

Ordering Information

Model Number: **QLW - ABCD EF GH - IJ**

ABCD = Frequency Range, minimum-maximum frequencies in GHz

EF = Noise figure in tenths of dB
(Example: EF = 45 for Noise Figure = 4.5 dB)

GH = Gain, in dB

IJ = Outline designation (E, G, I, J, P1, P2)

A.4 Triple Balanced Mixer MY52

MY52/MY52C

TRIPLE-BALANCED MIXER

· LO 2 TO 24 GHz
· RF 2 TO 24 GHz
· IF 0.1 TO 5 GHz
· LO DRIVE: +10 dBm (NOMINAL)
· HIGH COMPRESSION POINT
· VERY WIDE BANDWIDTH

Specifications (Rev. Date: 7/02)*

Characteristics	Typical	Guaranteed +25°C	Guaranteed -54° to +85°C
SSB Conversion Loss & SSB Noise Figure (max.)			
f_R = 8 to 18 GHz, f_L = 8 to 18 GHz, f_I = 0.1 to 4 GHz	7.5 dB	9.5 dB	10.0 dB
f_R = 2 to 8 GHz, f_L = 2 to 8 GHz, f_I = 1 to 4 GHz	8.0 dB	10.0 dB	10.5 dB
f_R = 2 to 18 GHz, f_L = 2 to 18 GHz, f_I = 0.1 to 5 GHz	8.5 dB	10.5 dB	11.0 dB
f_R = 18 to 24 GHz, f_L = 13 to 24 GHz, f_I = 0.1 to 5 GHz	9.5 dB	12.5 dB	13.0 dB
Isolation (min.)			
L to R			
f_L = 2 to 24 GHz	18 dB	15 dB	13 dB
f_L = 4 to 19 GHz	25 dB	20 dB	18 dB
L to I			
f_L = 2 to 20 GHz	30 dB	22 dB	20 dB
f_L = 20 to 24 GHz	20 dB	15 dB	13 dB
1 dB Conversion Compression			
f_L @ +10 dBm	+5 dBm		
Input IP3			
f_{R1} = 3.75 GHz @ -6 dBm, f_{R2} = 3.76 GHz @ -6 dBm, f_L = 4 GHz @ 10 dBm	+16 dBm		
f_{R1} = 13 GHz @ -6 dBm, f_{R2} = 13.01 GHz @ -6 dBm, f_L = 11 GHz @ 10 dBm	+16 dBm		
f_{R1} = 20 GHz @ -6 dBm, f_{R2} = 20.01 GHz @ -6 dBm, f_L = 24 GHz @ 10 dBm	+13 dBm		

* Typical values are measured at 25°C and are not guaranteed. Measured in a 50-ohm system with nominal LO drive and downconverter application only, unless otherwise specified. Subject to change without notice.

Absolute Maximum Ratings

Operating Temperature	-54°C to 100°C
Storage Temperature	-65°C to 100°C
Peak Input Power	26 dBm max. @ +25°, 22 dBm max. @ +100°C
Peak Input Current	mA DC

Outline Drawing(s)

Package	Figure	Model
VPAC	JB	MY52
SMA	JA	MY52C

Specifications subject to change without notice. • North America: 1-800-366-2266
Visit www.macom.com for complete contact and product information.

LucixDROs

Free Running DROs
Specification Performance

Low Phase Noise Excellent Frequency Stability Low Current High Power

June-04

C series		MODEL									
	Size	0.640" x 0.720" x 0.499"								1.608" x 0.993" x 0.612"	
Specification	Units	LO-164-FC	LO-173-FC	LO-182-FC	LO-191-FC	LO-201-FC	LO-211-FC	LO-222-FC	LO-233-FC	LO-245-FC	LO-258-FC
Frequency	GHz	16.071-16.900	16.901-17.760	17.761-18.670	18.671-19.630	19.631-20.640	20.641-21.700	21.701-22.810	22.811-23.980	23.981-25.210	25.211-26.500
RF power	dBm	9-12	9-12	8-11	8-11	8-11	8-11	7-10	7-10	7-10	7-10
frequency pushing	MHz/V	0.825	0.865	0.91	0.955	1.01	1.06	1.12	1.17	1.23	1.3
load pulling (2)	MHz	3.3	3.46	3.64	3.82	4.02	4.24	4.46	4.68	4.92	5.18
Phase noise	(1 Hz BW)										
@10 kHz	dBc/Hz	-88	-87	-87	-86	-86	-85	-85	-85	-84	-84
@100 kHz	dBc/Hz	-113	-112	-112	-111	-111	-110	-110	-110	-109	-109
@ 1 MHz	dBc/Hz	-138	-137	-137	-136	-136	-135	-135	-135	-134	-134
Frequency stability (4)	MHz	1.65	1.73	1.82	1.91	2.01	2.12	2.23	2.34	2.46	2.59
Mechanical tuning	MHz	> +/- 13.2	> +/- 13.8	> +/- 14.6	> +/- 15.2	> +/- 16.0	> +/- 17.0	> +/- 17.8	> +/- 18.8	> +/- 19.6	> +/- 20.8
Electrical tuning, min (1)	MHz	5.6	5.9	6.2	6.5	6.8	7.2	7.6	8.0	8.3	8.8
Tune voltage range (1)	V	0.6 to 7.4	0.6 to 7.4	0.6 to 7.4	0.6 to 7.4	0.6 to 7.4	0.6 to 7.4	0.6 to 7.4	0.6 to 7.4	0.6 to 7.4	0.6 to 7.4
Tune voltage center (1)	V	4	4	4	4	4	4	4	4	4	4

Other Parameters

Harmonics dBc	Spurious dBc	Supply Voltage V	Supply Current mA (7)	Temperature		Stability Over Temperature (p-p)		Aging ppm/year
				Operating ºC	Storage ºC	Frequency ppm (4)	Power dB (5) (6)	
-25	-95	5-16	55	-40 to +70	-55 to +85	100	2	+/- 1

Notes:
1. Varactor tuning is included in every unit.
2. Maximum frequency variation for 360º phase change in a 1.5:1 load.
3. Recommended input voltage. Unit equipped with on board regulator.
4. Total frequency variation over entire operating temperature range.
5. Total power variation over entire operating temperature range.
6. 3dB for LO-245-FC and LO-258-FC
7. 125 mA for LO-245-FC and LO-258-FC

Lucix Corporation

Contact us with your specific requirements: sales@lucix.com

800 Avenida Acaso • Camarillo, CA 93012 • (805)987-6645 • Fax: (808)987-6145 • www.lucix.com • sales@lucix.com

A.6 Square Law Detector 75VA50

MICROWAVE DETECTORS

70, 75 Series 100 kHz to 50 GHz

Anritsu

Specifications

Model	Frequency range	Flatness (dB)	Connectors		Impedance (Ω)	SWR (Maximum)	Low level sensitivity at –30 dBm (mV/µW)	High level sensitivity at +13 dBm (Volts, Min.)	Input maximum (mW)	Output capacitance (pF)
			In	Out						
70KA50	0.01 to 20 GHz	±0.6	K(m)	SMC(f)	50	1.33	0.6	1	100	30
70KC50	0.01 to 40 GHz	±0.5 to 20 GHz ±1.0 to 26.5 GHz ±1.5 to 40 GHz	K(m)	SMC(f)	50	1.33 to 20 GHz 1.50 to 26.5 GHz 1.90 to 40 GHz	0.4	1	100	30
75N50B	0.01 to 18 GHz	±0.3 to 12.4 GHz ±0.6 to 18 GHz	N(m)	BNC(f)	50	1.15 to 4.5 GHz 1.30 to 15 GHz 1.39 to 18 GHz	0.35	1	100	30
75KC50	0.01 to 40 GHz	±0.5 to 20 GHz ±1.0 to 26.5 GHz ±1.5 to 40 GHz	K(m)	BNC(f)	50	1.33 to 20 GHz 1.50 to 26.5 GHz 1.90 to 40 GHz	0.4	1	100	30
75VA50	0.01 to 50 GHz	±0.5 to 20 GHz ±1.0 to 26.5 GHz ±1.5 to 40 GHz ±3 to 50 GHz	V(m)	BNC(f)	50	1.33 to 20 GHz 1.50 to 26.5 GHz 1.90 to 40 GHz 2.1 to 50 GHz	0.4	1	100	30

Dimensions

Model	Dimensions L(cm) x dia(cm)
70KA50	4.6 x 1.0
70KC50	4.6 x 1.0
75N50B	6.4 x 1.8
75KC50	4.6 x 1.0
75VA50	4.6 x 1.0

Ordering information

Please specify model/order number, name, and quantity when ordering.

Model/Order No.	Name
	Microwave Detector
70KA50	10 MHz to 20 GHz, K(m) input, SMC(f) output, 50 Ω
70KC50	10 MHz to 40 GHz, K(m) input, SMC(f) output, 50 Ω
75KC50	10 MHz to 40 GHz, K(m) input, BNC(f) output, 50 Ω
75N50B	10 MHz to 18 GHz, N(m) input, BNC(f) output, 50 Ω
75VA50	10 MHz to 50 GHz, V(m) input, BNC(f) output, 50 Ω
	Options
Option 2 (75KC50)	Matching frequency response of two detectors
Option 3 (75KC50)	Matching frequency response of three detectors

* Upper frequency limit (GHz): ≤8, ≤12.4, ≤18, ≤26.5, ≤40

** Frequency response tracking (dB): ±0.2, ±0.3, ±0.6, ±0.8, ±1.2

Features

- *Broadband coverage, 10 MHz to 50 GHz with a Single Detector*
- *K Connector® compatible with SMA and 3.5 mm*
- *V Connector® compatible with 2.4 mm*
- *Lowest SWR: 1.33 to 20 GHz, 1.5 to 40 GHz*
- *Flat Response: ±0.5 dB to 20 GHz ±1.5 dB to 40 GHz*
- *Best Value for Instrumentation, system, and OEM applications*
- *Low price and availability from stock*
- *Standard output polarity is negative*
- *Positive polarity is available as a special*

Precision RF & Microwave Components Catalog No. 11410-00235, Rev. F
Printed in United States 2006-11

A.7 RT/duriod 6010LM

ROGERS CORPORATION
Advanced Circuit Materials

Advanced Circuit Materials Division
100 S. Roosevelt Avenue
Chandler, AZ 85226
Tel: 480-961-1382, Fax: 480-961-4533
www.rogerscorporation.com

Data Sheet
1.6000

RT/duroid® 6006/6010LM High Frequency Laminates

Features:

- High dielectric constant for circuit size reduction.
- Low loss. Ideal for operating at X-band or below.
- Low Z-axis expansion for RT/duroid 6010LM. Provides reliable plated through holes in multilayer boards.
- Low moisture absorption for RT/duroid 6010LM. Reduces effects of moisture on electrical loss.
- Tight ε_r and thickness control for repeatable circuit performance.

Some Typical Applications:

- Space Saving Circuitry
- Patch Antennas
- Satellite Communications Systems
- Power Amplifiers
- Aircraft Collision Avoidance Systems
- Ground Radar Warning Systems

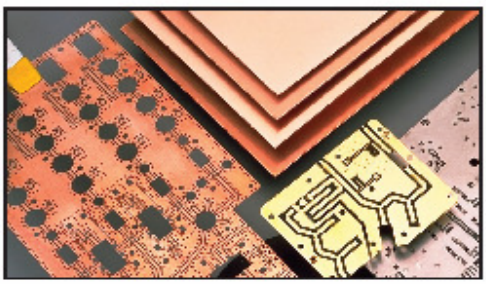

RT/duroid® 6006/6010LM microwave laminates are ceramic-PTFE composite designed for electronic and microwave circuit applications requiring a high dielectric constant. RT/duroid 6006 laminate is available with a dielectric constant value of 6.15 and RT/duroid 6010LM laminate has a dielectric constant of 10.2.

RT/duroid 6006/6010LM microwave laminates feature ease of fabrication and stability in use. They have tight dielectric constant and thickness control, nearly isotropic electrical properties, low moisture absorption, and good thermal mechanical stability.

Laminates are supplied clad both sides with ¼ to 2 oz./ft.^{2} (8 to 70 µm) electrodeposited (ED) copper foil. Cladding with rolled copper foil is also available. Thick aluminum, brass, or copper plate on one side may be specified.

Standard tolerance dielectric thicknesses of 0.010", 0.025", 0.050", 0.075", and 0.100" (0.254, 0.635, 1.270, 1.905, 2.54 mm) are available. When ordering RT/duroid 6006 and RT/duroid 6010LM laminates, it is important to specify dielectric thickness, electrodeposited or rolled, and weight of copper foil required.

PROPERTY	TYPICAL VALUE [2] 6006	TYPICAL VALUE [2] 6010LM [3]	DIRECTION	UNITS[1]	CONDITION	TEST METHOD
Dielectric Constant, ε_r	6.15 ± 0.15	10.2 ± 0.25 10.5 ± 0.25 10.8 ± 0.25	Z		10 GHz/A	IPC-TM-650 2.5.5.5
Dissipation Factor, tan δ	0.0027	0.0023	Z		10 GHz/A	IPC-TM-650 2.5.5.5
Thermal Coefficient of ε_r	-410	-425	Z		-50 to 170°C	IPC-TM-650 2.5.5.5
Surface Resistivity	7x10⁷	5X10⁸		Mohm	A	IPC 2.5.17.1
Volume Resistivity	2X10⁷	5X10⁸		Mohm cm	A	IPC 2.5.17.1
Young's Modulus under tension	627 (91) 517 (75)	931 (135) 559 (81)	X Y	MPa (kpsi)	A	ASTM D638 (0.1/min. strain rate)
ultimate stress	20 (2.8) 17 (2.5)	17 (2.4) 13 (1.9)	X Y	MPa (kpsi)	A	
ultimate strain	12 to 13 4 to 6	9 to 15 7 to 14	X Y	%	A	
Young's Modulus under compression	1069 (155)	2144 (311)	Z	MPa (kpsi)	A	ASTM D695 (0.05/min strain rate)
ultimate stress	54 (7.9)	47 (6.9)	Z	MPa (kpsi)	A	
ultimate strain	33	25	Z	%		
Flexural Modulus	2634 (382) 1951 (283)	4364 (633) 3751 (544)	X Y	MPa (kpsi)	A	ASTM D790
ultimate stress	38 (5.5)	36 (5.2) 32 (4.4)	X Y	MPa (kpsi)		
Deformation under load	0.33 2.10	0.26 1.37	Z Z	% %	24 hr/50°C/7MPa 24 hr/150°/7MPa	ASTM D621
Moisture Absorption	0.05	0.05		%	24 hr/23°C 0.050" (1.27mm) thick	IPC-TM- 650 2.6.2.1
Density	2.7	3.1				ASTM D792
Thermal Conductivity	0.48 (3.3)	0.78		W/m/K (BTU/in/ft²/hr/°F)	23 to 100°C	ASTM D2214, Modified
Thermal Expansion	47 34, 117	24 24, 24	X Y,Z	ppm/°C	0 to 100°C	ASTM 3386 (5K/min)
Td	500	500		°C TGA		ASTM D3850
Specific Heat	0.97 (0.231)	1.00 (0.239)		J/g/K (BTU/lb/°F)		Calculated
Copper Peel	14.3 (2.5)	12.3 (2.1)		pli (N/mm)	after solder float	IPC-TM-650 2.4.8
Flammability Rating	94V-0	94V-0				UL
Lead-Free Process Compatible	Yes	Yes				

(1) SI unit given first with other frequently used units in parentheses.
(2) References: APR4232.33 DAS 4019.27-32, Internal TR 2610. Tests were at 23°C unless otherwise noted. Typical values should not be used for specification limits.
(3) Dielectric constant is based on .025 dielectric thickness, one ounce electrodeposited copper on two sides.
Typical values are a representation of an average value for the population of the property. For specification values contact Rogers Corporation.

STANDARD THICKNESS:	STANDARD PANEL SIZE:	STANDARD COPPER CLADDING:
0.010" (0.254mm) 0.025" (0.64mm) 0.050" (1.27mm) 0.075" (1.90mm) 0.100" (2.50mm)	10" X 10" (254 X 254mm) 10" X 20" (254 X 508mm) 20" X 20" (508 X 508mm)	¼ oz. (8 µm) electrodeposited copper foil. ½ oz. (17µm), 1 oz. (35µm), 2 oz. (70µm) electrodeposited and rolled copper foil. Heavy metal claddings are available. Contact Rogers Customer Service.

CONTACT INFORMATION:			
USA:	Rogers Advanced Circuit Materials	Tel: 480-961-1382	Fax: 480-961-4523
Belgium:	Rogers NV - Gent	Tel: 32-9-2353611	Fax: 32-9-2353658
Japan:	Rogers Japan Inc.	Tel: 81-3-5200-2700	Fax: 81-3-5200-0571
Taiwan:	Rogers Taiwan Inc.	Tel: 886-2-86609056	Fax: 886-2-86609057
Korea:	Rogers Korea Inc.	Tel: 82-31-716-6112	Fax: 82-31-716-6208
Singapore:	Rogers Technologies Singapore Inc.	Tel: 65-747-3521	Fax: 65-747-7425
China:	Rogers (Shanghai) International Trading Co., Ltd	Tel: 86-21-63916088	Fax: 86-21-63915060

Revised 03/2005 0697-0305-1.5ON Publication: #92-105

Appendix B

Conferences

B.1 International Conferences

This thesis work has participated as oral presentation in the IEEE International Conference Andescon 2008. The reference and the submitted paper are shown below:

Benjamín López-García, D.V.B. Murthy, Alonso Corona-Chávez, and Ignacio E. Zaldívar-Huerta, "Passive Millimeter-Wave Imaging Using Substrate Integrated Waveguide Technology," *IEEE International Conference Andescon 2008,* October 15-17, 2008, Cuzco, Perú, pp. 100.01-100.04.

Passive Millimeter-Wave Imaging Using Substrate Integrated Waveguide Technology

Benjamín López-García student IEEE, D.V.B. Murthy, Alonso Corona-Chávez member IEEE, and Ignacio E. Zaldívar-Huerta member IEEE
Electronics Department of the National Institute of Astrophysics, Optics and Electronics, Tonantzintla, Apdo. Postal 51 y 216, Puebla, C.P.72000, México

Abstract—**A Passive Millimeter-Wave Imaging System for concealed object detection at the frequency of 24 GHz with total power radiometer configuration has been designed and tested. We added to the system a microwave lens to focus the target under surveillance to the antenna. The novelty of this work is the incorporation of the Substrate Integrated Waveguide (SIW) Exponential Flare Horn Antenna.**

Index Terms—**microwave lens, nipkow disc, passive millimeter-wave imaging, radiometer, substrate integrated waveguide antenna.**

I. Introduction

THE NEED for a concealed weapons and explosive detection has increased in recent years. The Millimeter-Wave (MMW) Imaging is a possible solution to this problem since millimeter-waves can penetrate thin clothing layers. This is a method of forming images through the detection of millimeter-wave radiation from a scene. This power is a combination of what the scene object is directly emitting and what it is reflecting from its environment. The MMW radiation does not present a health hazard to people under surveillance and this kind of systems has also the ability to see under conditions of low visibility (fog, clouds, smoke, sandstorms, etc.) that would ordinarily blind visible or infrared (IR) sensors [1], [10].

Millimeter-wave Imaging can be either active or passive [2]. In active mode a source illuminates the scene, which could be non-coherent or coherent, monochromatic or broadband. The source produces much higher power than those emitted from blackbodies within the scene (typically tens of thousands of degrees). Due to the much higher effective temperature of the surroundings, the millimeter waves generated by objects between the scene are of less significance producing more contrast in the imaging results but also undesired speckle and/or glint. In Passive Millimeter-Wave (PMMW) Imaging, the spectral distribution of natural radiation which is emitted or reflected from a body at environmental temperatures is properly captured and displayed (radiometry). Here we have less contrast that in the active mode but better image quality.

Various active and passive mode millimeter-wave imaging systems for target identification have been documented by several authors [1]-[15]. However, there is no report of a PMMW Imaging System using substrate integrated waveguide technology in the receiver antenna.

The novelty of this work is the incorporation of the Substrate Integrated Waveguide (SIW) Technology in the receiver antenna of the PMMW Imaging System. The SIW Technology is synthesized by placing two rows of metallic via-holes in a substrate. The field distribution in an SIW is similar to that in a conventional rectangular waveguide. Hence, it takes the advantages of low cost, lower losses than coplanar and microstrip lines, and it is highly integrable with microwave and millimeter wave integrated circuits [16]-[19].

II. Total Power Radiometer

A radiometer is a sensitive receiver specially designed to measure the radiation that a body either emits directly or reflects from surrounding bodies [20], [21].

The aspect of radiometry that is of most interest to the microwave engineer is the design of the radiometer itself. The basic problem is to build a receiver that can distinguish between the desired radiometric noise and the inherent noise of the receiver, even though the radiometric power is usually less than the receiver noise power. The total power radiometer configuration represents an approach to this problem.

The block diagram of a typical total power radiometer is show in Fig. 1 [22], [23]. The front end of the receiver is a standard superheterodyne circuit consisting of an RF amplifier, a mixer/local oscillator, and a detector stage. This detector is generally a square-law device, so that its output voltage is proportional to the input power. The integrator is essentially a low-pass filter with a cutoff frequency of 1/T, and serves to smooth out short-term variations in the noise power [24].

If the antenna is pointed at a background scene with a brightness temperature T_B, the antenna power will be $P_A=kT_BB$; this is the desired signal. The receiver contributes noise which can be characterized as a power $P_R=kT_RB$ at the receiver input, where TR is the overall noise temperature of the receiver. Thus the output voltage of the radiometer is

$$Vo = G(T_B + T_R)kB \qquad (1)$$

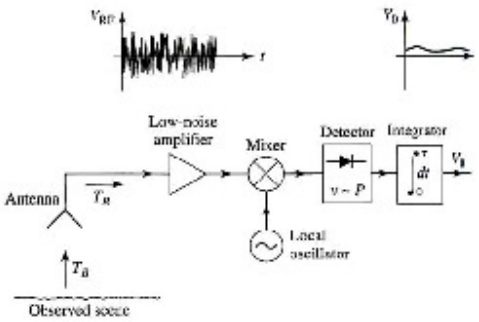

Fig. 1. Total Power Radiometer block diagram.

where G is the overall gain constant of the radiometer.

III. Passive Millimeter-Wave Imaging System

The experimental arrangement constructed for the passive millimeter wave imaging system is shown in Fig. 2. This system works at the frequency of 24 GHz. For the electronics we used the total power radiometer configuration described in section II.

To detect the small radiation emitted by the target we use a LNA which has a bandwidth from 15 to 26 GHz, 2.8 dB NF and 55 dB gain. To downconvert the frequency we use a triple balanced mixer with 9.5 dB NF. The local oscillator used achieves output power from 13 to 16 dBm with phase noise of ~135 dBc/Hz, and approximately 1 GHz of tuning range. The detector used is a square law detector with bandwidth from DC to 40 GHz. As mentioned in section II, an integrator with an integration time of 3 milliseconds was implemented to increase the sensitivity of the system.

We added to the system a microwave lens [25] to focus the target under surveillance to the antenna. The lens used has a diameter of 24 cm and it is made of Teflon material.

We designed a SIW horn antenna as proposed in reference [26]. We modified the design of the antenna by introducing exponential flares to have a wide bandwidth as shown in Fig. 3. The dimensions of the microstrip line are W_2 =3.8mm, and L_2 =2mm. The transition (from microstrip to SIW) dimensions are W_3 =5.32mm, and L_3 =10mm. The SIW dimensions are W_4 =6.312mm, L_4 =3.4mm, cylinder radius r =0.5mm, and cylinder separation p =1.2mm. The substrate thickness is h =2mm, and dielectric constant ε_r =10.2. The radius lens is H=8.6mm. The overall dimensions of the horn antenna are 41.775 x 19.4 x 2 mm^3.

IV. Results

To demonstrate the sensitivity of our system, several tests have been performed with concealed objects of different materials such as plastics, ceramics, cardboard and aluminum.

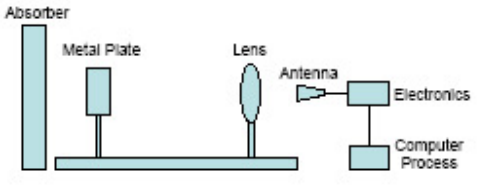

Fig. 2. Passive Millimeter-wave Imaging System block diagram.

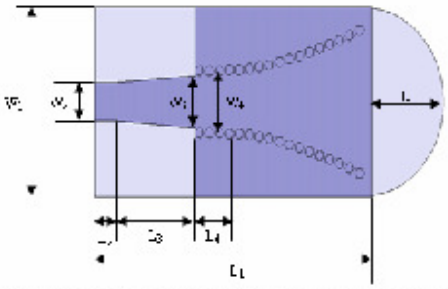

Fig. 3. Geometry of the SIW exponential flare horn antenna. The dimensions of the microstrip line are W_2 =3.8mm, and L_2 =2mm. The transition dimensions are L_3 =10mm, and W_3 =5.32mm. The SIW dimensions are W_4 =6.312mm, L_4 =3.4mm, cylinder radius r =0.5mm, and cylinder separation p =1.2mm. The substrate thickness is h =2mm, and dielectric constant of ε_r =10.2. The overall dimensions of the horn antenna are 41.775 x 19.4 x 2 mm^3.

Object	Voltage (mV)
Initial Voltage	81
Aluminum Metal Plate	110
Plastic Plate	79
Plastic Mousepath	78
Plastic Bucket	77
Plastic Mobile	79
Ceramic Plate	70
Cardboard Plate	81

Table 1. Voltage of different materials under surveillance

The obtained results, measured at room temperature, are shown in Table 1. The initial output voltage at the detector of our system having a microwave absorbing background foam 1m from the antenna was 81 mV. Then different objects have been sensed by placing them between the microwave foam wall and the receiver antenna. The metal plate shows the greatest voltage change with a difference of approximately 30 mV, while the cardboard plate did not provide any change. These findings are consistent with the theory, since the metal plate has an emissivity near to zero [11] and the cardboard is invisible to the millimeter waves [3].

The SIW antenna was simulated using a commercial finite element method package [26], and then fabricated. Its bandwidth is from 18 to 40 GHz, having a good response of the return loss S_{11} (under -10 dB approximately, see Fig. 4). The arc lens placed in the substrate improves the directivity of the SIW antenna. The radiation pattern obtained is illustrated in Fig. 5.

V. Conclusions

A passive millimeter-wave imaging system using SIW technology has been shown, different materials such as plastics, ceramics, cardboard and aluminum have been successfully detected. The incorporation of the SIW Technology in the radiometer of the PMMW Imaging System allows cost reduction and high integrability millimeter wave integrated circuits.

Acknowledgment

The authors thank to the INAOE and the Large Millimeter Telescope (GTM) to support this project. One of the authors, Benjamin López-García thanks to the National Council of Science and Technology (CONACyT) for the scholarship no. 204317.

References

[1] L. Yujiri, M. Shoucri, and P. Moffa, "Passive millimeter wave imaging," *IEEE Microwave Magazine*, vol. 4, no. 3, pp. 39-50, Sep. 2003.

[2] J. Detlefsen, A. Dallinger, and S. Schelkshorn, "Approaches to Millimeter-Wave Imaging of Humans," *Radar Conference, 2004. EURAD. First European*, 2004, pp. 279-282.

[3] K. Mizuno, H. Matono, Y. Wagatsuma, H. Warashina, H. Sato, S. Miyanaga, and Y. Yamanaka, "New Applications of Millimeter-Wave Incoherent Imaging," *Microwave Symposium Digest, 2005 IEEE MTT-S International*, 12-17 June 2005, pp. 629-632.

[4] L. L. Chao, Y. Jianyu, Z. Xin, F. Yong, and Z. R. Hong, "Design of a PMMW Imaging system," *Communications, Circuits and Systems, 2007. ICCCAS 2007. International Conference*, 11-13 July 2007, pp. 1313-1316.

[5] G.N. Sinclair, R.N. Anderton, and R. Appleby, "Outdoor passive millimetre wave security screening," *Security Technology, 2001 IEEE 35th International Carnahan Conference*, 16-19 Oct. 2001, pp. 172-179.

[6] D.O. Kornaev, L. Y. Bogdanov, and A.V. Nalivkin, "Passive Millimeter Wave Imaging System with White Noise Illumination for Concealed Weapons Detection," *Infrared and Millimeter Waves, 2004 and 12th International Conference on Terahertz Electronics, 2004. Conference Digest of the 2004 Joint 29th International Conference*, 27 Sept.-1 Oct. 2004, pp. 741-742.

[7] K. Watabe K. Shimizu, M. Yoneyama, and K. Mizuno, "Millimeter-Wave Active Imaging Using Neural Networks for Signal Processing," *Microwave Theory and Techniques, IEEE Transactions*, vol. 51, no. 5, pp. 1512-1516, May 2003.

[8] I.. Ocket, B. Nauwelaers, G. Koers,and J. Stiens, "Fast Modeling and Optimization of Active Millimeter Wave Imaging Systems," *Microwave Conference, 2006. 36th European*, Sept. 2006, pp. 1559-1562.

[9] T. Derham, H. Kamoda, T. Iwasaki, and T. Kuki, "Active MMW Imaging System using the Frequency-Encoding Technique," *Microwave Conference, 2007. KJMW 2007. Korea-Japan*, 15-16 Nov. 2007, pp. 181-184.

[10] M. Shoucri, R. Davidheiser, B. Hauss, P. Lee, M. Mussetto, S. Young, and L. Yujiri, "A Passive Millimeter Wave Camera for Aircraft Landing in Low Visibility Conditions," *Aerospace and Electronic Systems Magazine, IEEE*, vol. 10, no. 5, pp. 37-42, May 1995.

[11] L. Yujiri, "Passive Millimeter Wave Imaging," *Microwave Symposium Digest, 2006. IEEE MTT-S International*, pp. 98-101, June 2006.

[12] V.E. Lyubchenko, "Millimeter Wave Imaging Systems," *Microwaves Radar and Wireless Communications. 2000. MIKON-2000. 13th International Conference*, 22-24 May 2000, vol. 3, pp. 63-69.

[13] D.L. McMakin, D.M. Sheen, and T.E. Hall, "Three-Dimensional Millimeter-wave Imaging for Concealed Weapon Detection," *Microwave Theory and Techniques, IEEE Transactions*, vol. 49, no. 9, pp. 1581-1592, Sep. 2001.

[14] D.L. McMakin, D.M. Sheen, and H.D. Collins, "Remote Concealed Weapons and Explosive Detection on People Using Millimeter-wave Holography," *Security Technology, 1996. 30th Annual 1996 International Carnahan Conference*, 2-4 Oct. 1996, pp. 19-25.

[15] Z. Luo, J. Xiong, and J. Yang, "An Image Regulation Technique for Passive Millimeter Wave Focal Plane Array Imaging Radar System," *Radar, 2006. CIE '06. International Conference*, Oct. 2006, pp. 1-4.

[16] W. D'Orazio, and K. Wu, "Substrate-Integrated-Waveguide Circulators Suitable for Millimeter-Wave Integration," *Microwave Theory and Techniques, IEEE Transactions*, vol. 54, no. 10, pp. 3675-3680, Oct. 2006.

[17] W. D'Orazio, K. Wu, and J. Helszajn, "A Substrate Integrated Waveguide Degree-2 Circulator," *Microwave and Wireless Components Letters, IEEE*, vol. 14, no. 5, pp. 207 – 209, May 2004.

[18] K. Wu, D. Deslandes, and Y. Cassivi, "The Substrate Integrated Circuits - A New Concept for High-Frequency Electronics and Optoelectronics," *Telecommunications in Modern Satellite, Cable and Broadcasting Service, 2003. TELSIKS 2003. 6th International Conference*, vol. 1, 1-3 Oct. 2003, pp. III-X

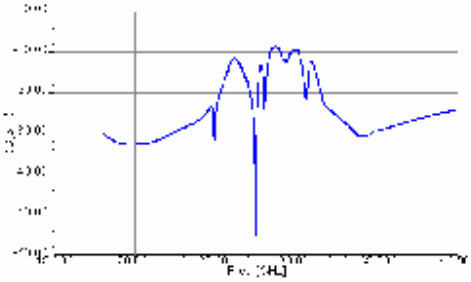

Fig.4. Return Loss S_{11} of the SIW exponential flare horn antenna.

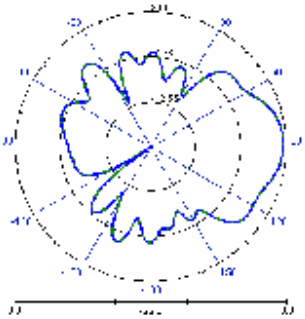

Fig. 5. Radiation patterns of the SIW exponential flare horn antenna.

[19] W. Che, B. Yao, and Y. L. Chow, "Substrate Integrated Waveguide Horn Antenna with Dielectric Lens," *Microwave and Optical Technology Letters*, vol 49, no. 1, pp. 168-170, Jan. 2007.
[20] D. M. Pozar, "Microwave Engineering," 3rd ed., Ed. Wiley, 2005, pp. 665-667.
[21] F.T. Ulaby, R. K. Moore, and A. K. Fung, "Microwave Remote Sensing: Active and Passive, Volume 1, Microwave Remote Sensing Fundamentals and Radiometry," Artech House, 1981, pp. 186-187.
[22] M. E. Tiuri "Radio Astronomy Receivers," *Antennas and Propagation, IEEE Transactions*, vol. 12, no. 7, pp. 930-938, Dec 1964.
[23] L. Quan, Z. Yong-hong, C. Qi-ke, F. Yong, Y. Jian-yu, and L. Liang-chao, "The W Band Radiometer for Imaging," *Communications, Circuits and Systems, 2007. ICCCAS 2007. International Conference*, 11-13 July 2007, pp. 1306-1308.
[24] H. Kim, S. Duffy, and J. Herd, "SiGe IC- based mm-wave imager," *Circuits and Systems, 2007. ISCAS 2007. IEEE International Symposium*, 27-30 May 2007, pp. 1975-1978.
[25] W. Chalodhorn, and D. R. DeBoer, "Use of Microwave Lenses in Phase Retrieval Microwave Holography of Reflector Antennas," Antennas and Propagation, IEEE Transactions, vol. 50, no. 9, pp. 1274-1284, Sep 2002.
[26] *"Ansoft HFSS*, version 9," Ansoft Corporation 2003.

Benjamin López-García was born in Puebla, Mexico, on December 05, 1981. He received the B.Sc. degree in electronic bachelor from Benemérita Universidad Autónoma de Puebla, Mexico in 2006. In the same year he joined the National Institute for Astrophysics, Optics and Electronics, Puebla, Mexico, where he currently studies the M. Eng. Degree in electronics with the speciality in microwaves. He is a student member IEEE.

Alonso Corona-Chavez (M'02) received the B.Sc. degree from the Instituto Tecnologico y de Estudios Superiores de Monterrey (ITESM), Monterrey, Mexico, in 1997, and the Ph.D. degree from the University of Birmingham, Edgbaston, U.K., in 2001. His doctoral research concerned microwave applications of superconductivity. From 2001 to 2004, he was a Microwave Engineer with Cryosystems Ltd., Luton, U.K., where he was involved with the development of microwave circuits using superconducting materials. During this time, he was also an Honorary Research Fellow with the School of Electrical Engineering, University of Birmingham. In 2004, he joined the National Institute for Astrophysics, Optics and Electronics, Puebla, Mexico, as an Associate Professor. His current interests include microwave applications of HTS, RF, and microwave devices for communications and radio astronomy.

Ignacio E. Zaldívar-Huerta received his B.Sc. degree in electronics engineering from Universidad Autónoma de Puebla, (México) in 1992, his M.Sc. Degree in microelectronics from the Instituto Nacional de Astrofísica, Optica y Electrónica (INAOE), México, in 1995, and his PhD degree in engineering sciences from Université de Franche-Comté, France, in 2001. Since February 2002, he has been an associate researcher at the Department of Electronics of the Instituto Nacional de Astrofísica, Optica y Electrónica in Tonantzintla, Puebla, México. His current research interests are primarily in fiber optics communication systems, and electro-optic devices on silicon, and microwave devices. He is a member of IEEE and SPIE.

D.V.B.Murthy was born in Andhra pradesh, India on August 2, 1980. He received the B.Sc. degree from Andhra university, India, in 2000, the M.Sc. degree in physics from Madras university, Tamilnadu, India in 2002, and Ph.D degree in microwave physics from Indian Institute of Technology, Madras, Tamilnadu, India in 2007. From 2007, he is working as Associate researcher C, Grand Millimeter telescope, National Institute of Astrophysics, Optics and Electronics, Puebla, Mexico. His current research interests include Microwave Hall effect, Passive millimeter wave imaging, Substrate integrated waveguide circuits, Microwave filters and Metamaterials.

B.2 Internal Conferences

This thesis work has also participated as poster presentation in the Noveno Encuentro de Investigación INAOE. The reference and the submitted paper are shown below:

Benjamín López-García, Alonso Corona-Chávez, and Ignacio E. Zaldívar-Huerta, “Passive Millimeter-Wave Imaging Using a Substrate Integrated Waveguide Antenna,” *Noveno Encuentro de Investigación INAOE,* November 6-7, 2008, Tonantzintla, Mexico, pp. 83-86.

Passive Millimeter-Wave Imaging using a Substrate Integrated Waveguide Antenna

Benjamin López-Garcia, Alonso Corona-Chávez & Ignacio E. Zaldivar Huerta
Electronics Department
benjamin_loga@inaoep.mx , alonsocorona@inaoep.mx, zaldivar@inaoep.mx

A passive millimeter-wave (PMMW) imaging system for concealed object detection at the frequency of 24 GHz with total power radiometer configuration has been designed and tested. We added to the system a microwave lens to focus the target to the antenna and a nipkow disc to scan the image under surveillance. We also incorporated the Substrate Integrated Waveguide (SIW) technology in the receiver antenna.

INTRODUCTION

Various passive mode millimeter-wave imaging systems for target identification have been reported by several authors [1], [2]. The novelty of this work is the incorporation of the Substrate Integrated Waveguide (SIW) technology in the receiver antenna, which is highly integrable with microwave and millimeter wave integrated circuits [3].

We also propose a technique that uses a nipkow disc to obtain the image under surveillance. The device consists of a mechanically spinning disk with a single turn spiral of equally distanced circular holes of equal diameter drilled in it, starting from an external radial point of the disk and proceeding to the center of the disk. When the disk rotates each hole in the spiral takes a horizontal "slice" through the image which is picked up as a pattern of light and dark by a sensor.

PASSIVE MILLIMETER-WAVE IMAGING SYSTEM

The block diagram of the PMMW imaging system is shown in Fig. 1. To enhance the sensitivity of the system we designed an integrator having integration time of 3 milliseconds.

We designed a SIW horn antenna as proposed in reference [4]. We modified the design of the antenna by introducing exponential flares to have a wide bandwidth as shown in Fig. 2.

We incorporate a microwave lens (to focus the target to the antenna) and a nipkow disc (to scan the image under surveillance) to the system. The lens used has a diameter of 24 cm and it is made of Teflon material. In order to validate the nipkow disc approach, we performed preliminary measurements at optical frequencies. The detailed explanation of the nipkow disc experimental arrangement at optical frequencies is given by Soto et. al., in [5]. The nipkow disc has a spiral of 6 holes which have a diameter of 1.5 mm.

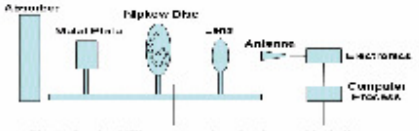

Fig. 1. Passive Millimeter-wave Imaging System block diagram.

RESULTS

The proposed antenna is shown in Fig. 2. It was simulated using a commercial EM simulator [6]. Its has a wide bandwidth from 18 to 40 GHz, having a good response of the return loss S_{11} (under -10 dB approximately), as shown in Fig. 3a. The arc lens placed in the substrate improves the directivity of the SIW antenna. The radiation pattern is illustrated in Fig. 3b.

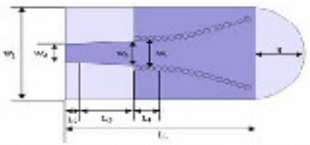

Fig. 2. Geometry of the SIW exponential flare horn antenna. The dimensions of the microstrip line are $W2$=3.8mm, and $L2$=2mm. The transition dimensions are $L3$=10mm, and $W3$=5.32mm. The SIW dimensions are W=6.312mm, L=3.4mm, cylinder radius r=0.5mm, and cylinder separation p=1.2mm. The substrate thickness is h=2mm, and dielectric constant of ε_r=10.2. The length of the arc is lh=8.6mm. The overall dimensions of the horn antenna are 41.775 x 19.4 x 2 mm^3.

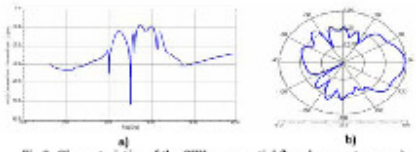

a) b)

Fig.3. Characteristics of the SIW exponential flare horn antenna. a) Return Loss S11. b) Radiation pattern.

A photograph of the experimental arrangement is shown in Fig. 4. Several tests have been performed with concealed objects of different materials such as plastics, ceramics, cardboard and aluminum. The results are shown in Table 1. The initial output voltage at the detector of our system having microwave absorbing background foam placed 1m away from the antenna was 81 mV. Then different objects have been sensed by placing them between the microwave foam and the receiver antenna. The metal plate showed a difference of approximately 30 mV with the initial value, while the cardboard plate did not provide any change. These findings are consistent with the theory, since the metal plate has an emissivity near to zero [1] and the cardboard is invisible to the millimeter waves [2].

Fig. 4. Photograph of the PMWW imaging system.

Object	Voltage (mV)
Initial Voltage	81
Aluminum Plate	110
Plastic Plate	79
Plastic Mosaicpull	78
Plastic Basket	77
Plastic Mozda	79
Ceramic Plate	79
Cardboard Plate	81

Table 1. Output voltage of different materials under surveillance.

The image obtained using the nipkow disc at optical frequencies is shown in Fig. 5b. The image projected on the scanning area was given the shape of a letter C, measuring 19.5mm high and 22.5mm wide. It has 30 data points obtained from the 6 holes in the nipkow disc taking 5 samples of each hole. No corrections were made for shape or intensity distortions in the reconstructed image.

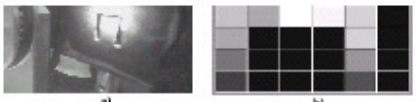

a) b)

Fig. 5. a) Object under surveillance. b) Computer image result

CONCLUSIONS

A passive millimeter-wave imaging system using a SIW technology has been shown, different materials such as plastics, ceramics, cardboard and aluminum have been successfully detected. The SIW exponential flare horn antenna was simulated obtaining good return loss in a wide bandwidth (18-40 GHz) and high directivity. The image (letter C) obtained using the nipkow disc at optical frequencies is presented. The demonstration of the nipkow disc principle is made in the optical region in order to validate the approach at microwave frequencies.

REFERENCES

[1] L. Yujiri, "Passive Millimeter Wave Imaging," *Microwave Symposium Digest, 2006. IEEE MTT-S International*, pp. 98-101, June 2006.

[2] K. Mizuno, H. Matsuo, Y. Wagatsuma, H. Sugahara, H. Sato, S. Hiyamizu, and Y. Yamamoto, "New Applications of Millimeter-Wave Incoherent Imaging," *Microwave Symposium Digest, 2005 IEEE MTT-S International*, 12-17 June 2005, pp. 629-632.

[3] K. Wu, D. Deslandes, and Y. Cassivi, "The Substrate Integrated Circuits - A New Concept for High-Frequency Electronics and Optoelectronics," *Telecommunications in Modern Satellite, Cable and Broadcasting Service, 2003. TELSIKS 2003. 6th International Conference*, vol. 1, 1-3 Oct. 2003, pp. III-X.

[4] W. Che, B. Yao, and Y. L. Chow, "Substrate Integrated Waveguide Horn Antenna with Dielectric Lens," *Microwave and Optical Technology Letters*, vol 49, no. 1, pp. 169-170, Jan. 2007.

[5] José Soto, and J. A. Dávila, "A Technique for the Fast Raster-Scanned Motion of a Small Window for Millimeter- Wave Image Acquisition," in *Microwave and Optical Technology Letters*, Vol 32, No. 6, pp. 440-442, March 2002.

[6] "Ansoft HFSS, version 9," Ansoft Corporation 2003.

Figure Index

Table Index